

EFFECT OF VARIOUS CERAMIC PRECURSORS ON THE MECHANICAL, THERMAL,  
AND ELECTROCHEMICAL PROPERTIES OF POLYMER/CERAMIC NANOFIBER  
SEPARATORS FOR LITHIUM ION BATTERIES

A Dissertation

Presented to the Faculty of the Graduate School

of Cornell University

In Partial Fulfillment of the Requirements for the Degree of

Doctor of Philosophy

by

Soshana Adele Smith

May 29, 2016

© 2016 Soshana Adele Smith

EFFECT OF VARIOUS CERAMIC PRECURSORS ON THE MECHANICAL, THERMAL,  
AND ELECTROCHEMICAL PROPERTIES OF POLYMER/CERAMIC NANOFIBER  
SEPARATORS FOR LITHIUM ION BATTERIES

Soshana Adele Smith, Ph. D.

Cornell University 2016

Researchers have been incorporating ceramics into porous membrane separators as a way to improve their mechanical, thermal and battery performances. However, the inclusion of pre-formed ceramics within the polymer membrane can require multiple additional steps. Current methods of ceramic particle inclusion in the polymer network can lead to issues of particle aggregation which can lead to non-uniform membrane performance. Ceramics present on the surface can delaminate from the surface, which would negatively affect the membrane performance. For this study, we aimed to incorporate room temperature curable liquid ceramic precursors into polymer networks to fabricate polymer/ceramic hybrids in a single electrospinning step.

First, we combined polyacrylonitrile (PAN) and organopolysilazane (OPSZ) to successfully create polymer-ceramic membranes without the need for further post-treatment. We varied the amount of ceramic precursor added to investigate the effect of ceramic loading on membrane properties and its electrochemical performance. Results show that with increasing the amount of ceramic, there is an improvement in the mechanical strength and thermal stability of the membranes. There is also an increase in ionic conductivity with increased ceramic inclusion as the presence of the ceramic disrupts the polymers ability to crystallize. The increased ionic conductivity correlated to an increase in battery performance and capacity retention especially at high charge/discharge rates. We note that all nanofiber based separators in the current study have the similar porosity around 80%, and they exhibit a wide range of the rate

capability performances due to their different internal and surface morphologies of nanofibers which in turn affect the ionic conductivity.

We then used various organopolysilazanes with different ratios of tetraethyl orthosilicate (TEOS) pendant chain to polysilazane backbone to investigate the effect of ceramic structures on the membrane performance. Our results demonstrate that changing the TEOS to polysilazane ratio can affect that the ceramics ability to form a continuous network within the polymer at the same concentration. The ability to form continuous network increases the amorphous regions within the polymer network, leading to an increase in the ionic conductivity which in turn leads to better battery performance.

We note that using OPSZ shows an approximately 5 nm ceramic sheath layer forms on the fibers. In order to investigate the effect of this ceramic sheath layer, we incorporated various silica precursors which resulted in various polymer-ceramic morphologies, ranging from no sheath layer, partial sheath layers, and to full shear layer on the polymer/ceramic fibers. Our results reveal that the presence of ceramic sheath layer leads to better membrane-electrolyte interaction which caused the increase in electrolyte uptake and ionic uptake. Additionally, the ceramic on the sheath layer can aid in preventing the buildup of fluorine based particles on the surface on the fiber, leading to improved capacity retention.

## BIOGRAPHICAL SKETCH

Soshana Adele Smith was born in Kingston, Jamaica on August 17<sup>th</sup>, 1987. She lived there until age ten, at which time she immigrated to Lauderhill, FL with her family. In May 2005, she graduated from Boyd H. Anderson High school in the top 1% of her graduating class after completing the International Baccalaureate program. She began her college career in August 2005 at Cornell University studying Chemical and Biomolecular Engineering. She graduated with a Bachelor of Science in May 2009. Soshana decided to continue post-secondary education in the spring of 2010, enrolling in Fiber Science & Apparel Design M.S. program at Cornell University. For her master's project, she worked with Professor Juan Hinestroza, completing her master's thesis "Characterization of Island-In-The-Sea Bi-Component Nylon/ Polyethylene Terephthalate Fibers Using Atomic Force Acoustic Microscopy" in August 2012. In March 2013, Soshana started her PhD work in Professor Yong Lak Joo's research group studying the effect of various ceramic precursors on the membrane performance of electrospun polymer/ceramic hybrid membranes.

To my beloved family for all their love and support

## ACKNOWLEDGMENTS

First, I would like to thank my advisor Dr. Yong Lak Joo for giving me the opportunity to join his research group and all his advice over the last three years during my work on this project. I would also like to thank Dr. Lynden Archer, who served both as my undergraduate advisor and special committee member for my PhD project. Dr. Archer gave me my first research opportunity in the summer of 2007, which lead me on the path to graduate work. During my graduate work he has also given me invaluable insight for which I will also be grateful. Dr. Margaret Frey has also been a great mentor to me over the last six years, offering great academic and professional advice. Finally I would like to thank Professor Tobias Hanrath for agreeing to serve as a proxy member on committee with such short notice.

I would also like to thank the all members of the Joo group for all their expert advice. In particular I would like to thank Dr. Jay Hoon Park for his help in the beginning of this project and his expert electrospinning advice. I am also grateful to Brian Williams for his help with TEM and microtoming. Dr. Ling Fey and Ghazal Shoorideh were a constant source of knowledge and advice.

Finally, I would like to thank my friends and family for their support and guidance over the last six years.

## TABLE OF CONTENTS

<b>Chapter 1 Introduction .....</b>	<b>1</b>
<b>1.1 Overview of Batteries .....</b>	<b>1</b>
1.1.1 Battery Basics .....	1
1.1.3 Battery Configuration .....	3
1.1.4 Overview of Lithium Ion Battery .....	4
<b>1.2 Overview of Separators .....</b>	<b>7</b>
1.2.1 Introduction on the separator .....	7
1.2.2 Requirements for lithium-ion battery separators .....	8
1.2.2.1 Thickness .....	8
1.2.2.2 Electrochemical Stability .....	8
1.2.2.3 Porosity and Pore Size .....	8
1.2.2.4 Mechanical Stability .....	9
1.2.2.4 Thermal Stability .....	10
1.2.2.5 Wettability and Electrolyte Uptake .....	10
1.2.2.6 Permeability .....	10
1.2.2.7 Dimensional Stability .....	11
1.2.3. Types of separators .....	11
1.2.3.1 Microporous membranes .....	11
1.2.3.2 Nonwoven Separators .....	17
1.2.3.3 Composite Separators .....	24
<b>1.3 Electrospinning .....</b>	<b>33</b>
<b>1.4 Ceramic Precursors .....</b>	<b>37</b>
<b>References .....</b>	<b>40</b>
<b>CHAPTER 2 Objectives and Motivation .....</b>	<b>50</b>
<b>Chapter 3 Experimental Procedure .....</b>	<b>53</b>
<b>3.1 Materials .....</b>	<b>53</b>
<b>3.2 Material Preparation .....</b>	<b>53</b>
<b>3.3 Membrane Characterization .....</b>	<b>54</b>
<b>3.4 Electrochemical Characterization .....</b>	<b>56</b>
<b>Chapter 4 Polyacrylonitrile/Polymer Derived Ceramic Co-continuous Nanofiber Membranes via Room-Curable Organopolysiloxazane for Improved Lithium Ion Battery Performance .....</b>	<b>58</b>
<b>4.1 Introduction .....</b>	<b>58</b>
<b>4.2 Experimental Section .....</b>	<b>61</b>
4.2.1 Material Characterization .....	61
4.2.2 Electrochemical Characterization .....	63
<b>4.3 Results and Discussion .....</b>	<b>63</b>
4.3.1 Physical Properties .....	63
4.3.2 Electrochemical Performance .....	76
<b>4.4 Conclusion .....</b>	<b>80</b>
<b>References .....</b>	<b>81</b>

<b>Chapter 5 Impact of The Structure of Room-Curable Organopolysilazane on the Performance of Electrospun PAN/Polymer Derived Ceramic Composite Nanofiber Membranes for Lithium Ion Battery Separators .....</b>	<b>83</b>
<b>5.1 Introduction .....</b>	<b>83</b>
<b>5.2 Experimental .....</b>	<b>86</b>
5.2.1 Material Preparation.....	86
5.2.2 Characterization .....	86
<b>5.3 Results and Discussion .....</b>	<b>88</b>
<b>5.4 Conclusions .....</b>	<b>101</b>
<b>References .....</b>	<b>102</b>
<b>Chapter 6 Effect of Ceramic Morphology on the Properties of Bi-Component Polyacrylonitrile/Polymer-Derived Ceramic Nanofibers for the use as Separator Membranes in Lithium-ion Batteries.....</b>	<b>104</b>
<b>6.1 Introduction .....</b>	<b>105</b>
<b>6.2 Experimental .....</b>	<b>107</b>
6.2.1 Membrane Preparation .....	107
6.2.2 Membrane Characterization.....	108
<b>6.3 Results and Discussion .....</b>	<b>109</b>
<b>6.4 Conclusion .....</b>	<b>120</b>
<b>References .....</b>	<b>121</b>
<b>Chapter 7 Conclusion.....</b>	<b>125</b>
<b>Chapter 8 Recommendation for Future Works .....</b>	<b>128</b>

## LIST OF FIGURES

Figure 1-1 Comparison of volumetric and gravimetric energy density of the secondary battery systems <sup>5</sup> .....	2
Figure 1-2 Battery Configurations: a) Flat stacked cell <sup>17</sup> b) coin cell <sup>18</sup> c) cylindrical cell <sup>18</sup> .....	4
Figure 1-3 Crystal structure of the three lithium-insertion compounds in which the Li+ ions are mobile through the 2-D (layered), 3-D (spinel) and 1-D (olivine) frameworks. <sup>25</sup> .....	5
Figure 1-4 Schematic of a Lithium ion battery. Consisting of a positive electrode (cathode), negative electrode (anode), electrolyte and other materials <sup>28</sup> .....	7
Figure 1-5 Structure of dry process made polyolefin separators before (a) and after (b) stretching <sup>41</sup> .....	12
Figure 1-6 Microstructure of various membranes created via the wet process procedure: (a) Celgard <sup>45</sup> , (b) Tonen <sup>3</sup> .....	13
Figure 1-7 Cross-section SEM micrographs of blend membranes with different weight ratios of PMMA/PVDF. <sup>53</sup> .....	17
Figure 1-8 Images of non-wovens created by a) melt-blown method <sup>56</sup> b) wet laid method <sup>57</sup> c) electrospinning <sup>58</sup> .....	18
Figure 1-9 The cycle performances of Li/LiFePO <sub>4</sub> cell using electrospun PET fibrous membrane and Celgard membrane. <sup>59</sup> .....	19
Figure 1-10 Cycle performance of the cells with Celgard™ 2400 and PVDF (EPM884) at room temperature .....	22
Figure 1-11 Electrolyte uptake (%) of PIM and ESM (liquid electrolyte: 1 M LiPF <sub>6</sub> in EC/DMC). .....	23
Figure 1-12 Effect of temperature on the ionic conductivity of P(VdF-co-HFP) membranes (liquid electrolyte: 1 M LiPF <sub>6</sub> in EC/DMC). <sup>72</sup> .....	23
Figure 1-13 SEM images of separator surface with and without SiO <sub>2</sub> particles coating. (a) Without coating, (b) 8%, (c) 20%, (d) 27%, (e) 45%, (f) 55%. <sup>75</sup> .....	26
Figure 1-14 a) The variation in contact angle between polyolefin microporous membranes and polyolefin nonwoven membranes with and without ceramic inclusion b) LiCoO <sub>2</sub> /graphite full cell performance of batteries with various membranes .....	29
Figure 1-15 Schematic depiction of the PAN/Celgard/silica membranes <sup>83</sup> .....	30
Figure 1-16 Photographs showing liquid electrolyte (1 M LiPF <sub>6</sub> in EC/DMC = 1/1 v/v) wetting behavior of Celgard 2500 separator and SPN separator <sup>85</sup> .....	31
Figure 1-17 Schematic of electrospinning set up (a) Formation of Taylor cone in an applied electric field. (b) Taylor cone ejects fluid jet. (c) Surface tension causes cone shape to relax. <sup>95</sup> .....	35
Figure 1-18 Different fiber morphologies achieved by various researchers using the electrospinning technique: a) beaded <sup>112</sup> b) aligned <sup>113</sup> c) hollow <sup>114</sup> d) core-sheath <sup>115</sup> e) flat ribbon <sup>107</sup> f) porous <sup>116</sup> .....	36
Figure 1-19 Chemical structure of PHPS and its conversion to silica at ambient temperature .....	38

Figure 1-20 The chemical formula of organopolysilazane where $R_1$ and $R_2$ can be organic pendant groups or hydrogen .....	39
Figure 3-1 Configuration of a typical full cell.....	57
Figure 4-1 a) FTIR spectra of liquid OPSZ and cured PDC b) FTIR spectra of PAN and PAN/OPZ electrospun membranes.....	65
Figure 4-2 SEM images of electrospun membranes. a) PAN B) PAN/PDC 90:10 wt% c) PAN/PDC 80:20 wt% d) PAN/PDC 70:30 wt% .....	67
Figure 4-3 TEM images of PAN/OPZ composite fibers. a-b) cross section and longitudinal view of 10 wt% fibers. c-d) cross section and longitudinal view of 20 wt% fibers. e-f) cross section and longitudinal view of 30 wt% fibers.....	68
Figure 4-4 SEM images of fiber mats after PAN has been removed with DMF. a) 10 wt% b) 20 wt% c) 30 wt%.....	69
Figure 4-5 a) TGA isotherms of PAN and PAN/PDC mats. B) DSC measurement showing the cyclization temperature, an exothermic process, of the PAN polymer .....	70
Figure 4-6 DMA showing the mechanical stability of PAN and PAN/PDC membranes .....	72
Figure 4-7 XRD patterns of electrospun PAN/PDC composite membranes with various ceramic contents .....	73
Figure 4-8 a) Dynamic contact angle measurements as a function of time using various membranes b) Variations of electrolyte uptake in electrospun PAN/PDC composite membranes with PDC content.....	75
Figure 4-9 Nyquist plots for the cells with Celgard, PAN membrane, 90:10wt%, 80:20wt%, 70:30wt% PAN/PDC membranes respectively.....	77
Figure 4-10 Cycle performance of LiCoO <sub>2</sub> /graphite full cells with various separator membranes at 0.2C .....	79
Figure 4-11 Results of rate capability tests for the LiCoO <sub>2</sub> /graphite full cells with various separator membranes .....	80
Figure 5-1 SEM images and TEM images cross sectional and longitudinal cross section of various separator membranes. (a-c) 40wt% (d-f) 20wt% (g-i) 0wt%...	91
Figure 5-2 SEM images of various membranes after removal of PAN using DMF rinse (a,d) 0wt%, (b,e) 20 wt%, (c,f) 40wt% .....	92
Figure 5-3 DSC thermograms of various separator membranes .....	93
Figure 5-4 Typical stress-strain curves of various separator membranes .....	94
Figure 5-5 XRD patterns of electrospun PAN/PDC composite membranes with various ceramic contents .....	95
Figure 5-6 Ionic conductivity of various membranes in relation to polymer crystal size and crystallinity .....	97
Figure 5-7 The cycle performances of LiCoO <sub>2</sub> /graphite full cells with various separator membranes at a) 0.2C b) 0.5C .....	99
Figure 5-8 Results of rate capability tests for the LiCoO <sub>2</sub> /graphite full cells with various separator membranes .....	101
Figure 6-1 FTIR of various PAN/ceramic membranes .....	110
Figure 6-2 SEM images of various PAN/Ceramic membranes. a) OPSZ b) MSQ c) MSX d) PSSQ.....	111

Figure 6-3 TEM images revealing the internal morphology of the PAN/ceramic fibers. a-b) PAN/OPSZ c-d) PAN/MSQ e-f) PAN/MSX g-h) PAN/PSSQ.....	113
Figure 6-4 Stress-Strain curves of the four membranes .....	114
Figure 6-5 a) Electrolyte uptake of various separator membranes b) Contact angle between separator membranes and electrolyte .....	115
Figure 6-6 a) Ionic Conductivity of PAN/ceramic based separator membranes a) Nyquist plots for the cells with containing four PAN/ceramic based membranes .....	117
Figure 6-7 Cycling performance of LiCoO <sub>2</sub> /graphite full cells at a) 0.2C and b) 0.5C .....	119
Figure 6-8 SEM images of membranes after cycling. a) OPSZ b) MSQ c) MSX d) PSSQ.....	120
Figure 8-1 Cycling Performance of various PAN/OPSZ 90:10wt% .....	130
Figure 8-2 SEM Images of membranes after being cycled at 0.5C for 100 cycles. a) Annealed b) Annealed 2 c) As-Spun 3 months after Spinning d) As-Spun 1 Day after Spinning 3) As-Spun 2 days after Spinning .....	131

## LIST OF TABLES

Table 1-1 Properties of various cathode materials. <sup>25</sup> .....	6
Table 3-1 Spinning conditions of various polymer/ceramic hybrid membranes. Note: MSQ and MSX a solutions are only 12 percent ceramic precursor. While the others are 100 percent precursor.....	54
Table 4-1 Characteristics of PAN/PDC composite separators of various PDC inclusions .....	67
Table 4-2 Electrochemical impedance spectra (EIS) of various separators .....	77
Table 5-1 Weight change in polymer/ceramic hybrid fibers after annealing .....	88
Table 5-2 Elemental composition of OPSZ precursors and resultant ceramic inside the fiber after electrospinning.....	89
Table 5-3 Fiber diameter, porosity, pore size distribution and electrolyte uptake of various separator membranes .....	91
Table 6-1 Electrospinning conditions for various separator membranes .....	108
Table 6-2 Characteristics of PAN/PDC composite separators of various PDC inclusions .....	111

## LIST OF ABBREVIATIONS

OPSZ - Organopolysilizane

PAN – Polyacrylonitrile

DMF- N,N-Dimethylformamide

MSQ - Methylsilsesquioxane

MSX - Methylsiloxane

PSSQ - Polysilsesquioxane

SEM - Scanning Electron Microscopy

TEM - Transmission Electron Microscopy

XRD - Wide angle X-ray diffraction

TGA - Thermogravimetric Analysis

DSC - Differential Scanning Calorimetry

LiCoO<sub>2</sub> – Lithium Cobalt Oxide

FTIR - Fourier Transform Infrared Spectroscopy

PDC – Polymer Derived Ceramic

## LIST OF SYMBOLS

$M_a$  - Soaked membrane mass

$M_i$  - Dry Membrane mass

$P$  - Membrane porosity

$W$  - Membrane weight

$\rho$  - Membrane Density

$V$  - Membrane apparent volume

$D_e$  - effective diffusivity defined as the diffusion through a pore space of a porous media

$D$  - diffusion coefficient

$\varepsilon$  - porosity

$\tau$  - tortuosity

## Chapter 1 Introduction

### 1.1 Overview of Batteries

#### 1.1.1 Battery Basics

A battery consists of one or more electrochemical cells that convert stored chemical energy into electrical energy. Ever since its invention in the 1800 by Alessandro Volta<sup>1</sup>, batteries have been a vital component of our daily lives. They are used to power a number of devices to make modern live more convenient and efficient. A typical battery consist of four components:

- a) The cathode is a positive electrode. It accepts electrons from the external circuit with reduction during the electrochemical reaction. The half-cell with the cathode has the higher electrode potential.
- b) The anode is a negative electrode. It supplies electrons to external circuit with oxidation during electrochemical reaction. The half-cell with the anode has the lower electrode potential.
- c) The electrolyte provides the medium for the transfer of charges in the cell between the anode and cathode. The electrolyte is typically a solvent containing dissolved ions, which gives ionic conductivity. It should be a non-conductor of electrons to avoid self-discharge of the cell.
- d) The separator should physically and electrically isolate the anode and cathode.

When a battery is fully charged, the anode is fully charged with electrons giving it a negative charge, while the cathode is lacking in electrons giving it a positive charge, this creates a potential difference within the cell. As the battery is discharged the excessive electrons present on the negatively charged anode side flow to the positively charged cathode creating a circuit. Similarly ions can also flow from the cathode to anode, creating a redox reaction.

### 1.1.2 Types of batteries

Batteries are classified as either primary or secondary batteries depending on their ability to recharge. Primary batteries participate in an irreversible electrochemical reaction therefore it can be only be used once and then discarded. Primary batteries are more suitable for long periods of storage with low self-discharge such a smoke detector or alarm. Secondary batteries can be charged and discharged over and over because the electrochemical reaction is reversible. There are several different types of secondary batteries including lead-acid, nickel cadmium (NiCd), nickel metal hydride (NiMH), lithium-ion (Li-ion), lithium-ion polymer (Li-ion polymer), etc.<sup>2-4</sup> Comparison of characteristics and energy density of the different types of secondary batteries can be seen in Figure 2.

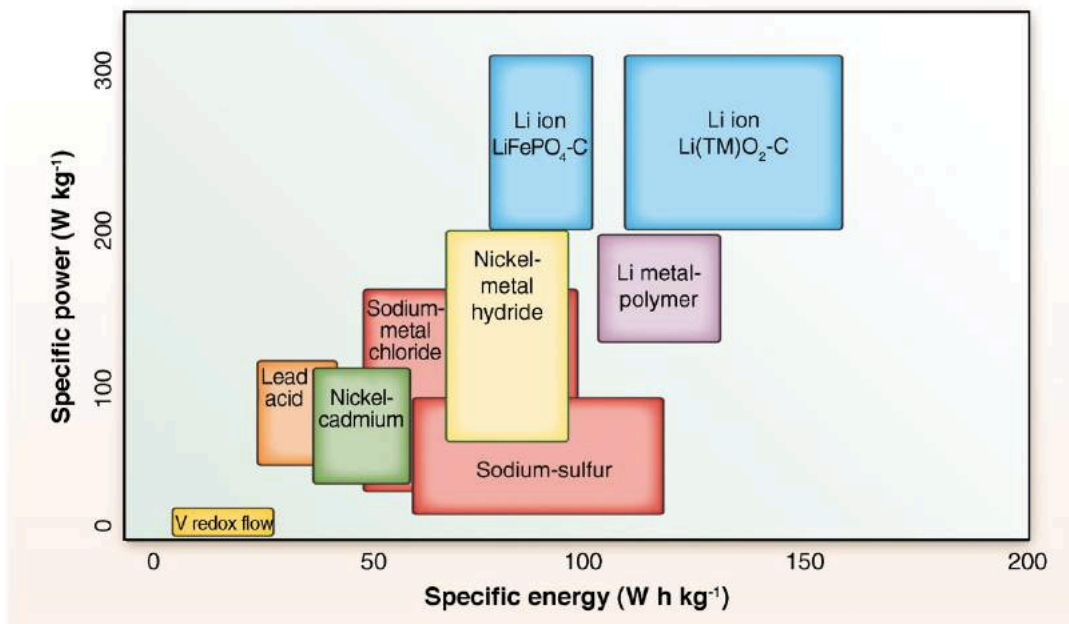


**Figure 1-1** Comparison of volumetric and gravimetric energy density of the secondary battery systems<sup>5</sup>

Lead acid batteries were the first commercially available secondary batteries; invented in by the French physician Gaston Plante in 1859.<sup>6,7</sup> Because of its ability for high surge currents, these types of batteries have a large power to weight ratio, making it attractive for the use in motor vehicles, hospital equipment and other equipment. Lead cell are arranged in a flat-stacked cells configuration consisting of alternating sheets of anode and cathode materials separated by separator material. Nickel-cadmium (Ni-Cd) batteries are secondary battery using nickel oxide hydroxide and metallic cadmium as electrodes.<sup>8</sup> Ni-Cd batteries are usually present in AA, AAA, C, D batteries commonly used in flashlights, children toys and power tools. They are attractive because of long life, high discharge rate, and economical price.<sup>9,10</sup> However, since the 1990's the sales of these batteries have fallen dramatically in favor of NiMH and li-ion battery due to the toxicity of materials used in Ni-Cd batteries. NiMH is similar to Ni-Cd but has three times the power density for the same size battery.<sup>11</sup> With the rapid growth in the personal devices such as cell phones and laptop computers, there also been a large growth in the demand for lithium ion batteries. Lithium ion batteries have a high energy density to weight ratio and excellent cycle life.

### **1.1.3 Battery Configuration**

Batteries can be arranged in a variety of configuration and shapes depending on the needed application. Coin cells were designed to minimize battery size and are used widely in watches, calculators, and memory backup where small size, high capacity and low power are required.<sup>12,13</sup> These cells involve circular cathode and anode electrodes separated by separator. The cell is filled with electrolyte, spacer and springs and sealed. Despite all the advantages of

this configuration, it is also plagued by disadvantages including the lack of safety vents, which can lead to swelling if the cell is charged too fast.<sup>11,14</sup>

With demand for smaller and higher power batteries, it was important to increase the amount of active material present in battery cell. In order to facilitate the increase in material and maintain a compact size, batteries are assembled in a cylindrical configuration. In this configuration, the cathode, anode and separator are assembled in flat sheets and then tightly rolled into a spiral shape. This configuration leads to low internal resistance but limits space for the electrolyte and so the potential energy storage capacity of the cell is greatly reduced.<sup>11,15,16</sup> The cylindrical configuration is widely used in Ni-Cd and NiMH cells, such as the AA batteries most consumers are familiar with using. Examples of each configuration can be seen below.

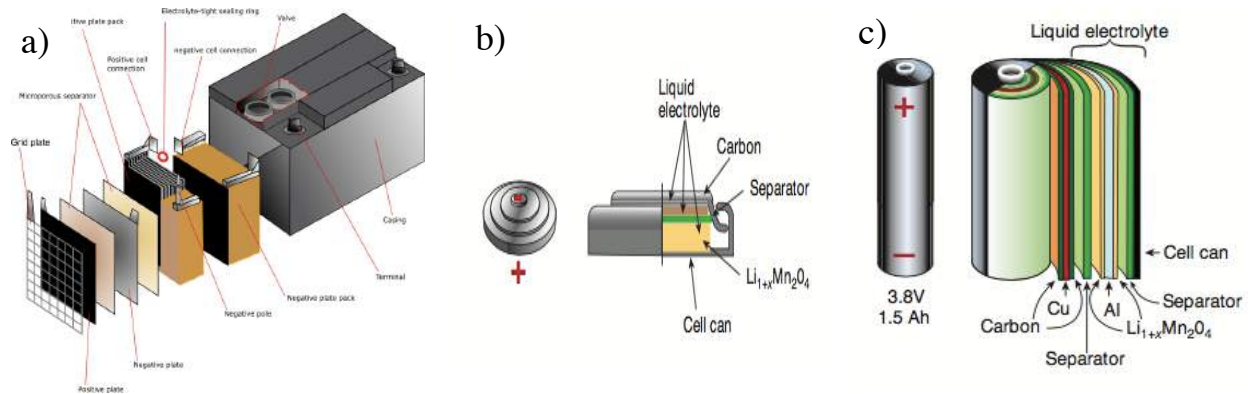


**Figure 1-2** Battery Configurations: a) Flat stacked cell<sup>17</sup> b) coin cell<sup>18</sup> c) cylindrical cell<sup>18</sup>

### 1.1.4 Overview of Lithium Ion Battery

A lithium-ion battery is the most popular secondary battery for portable electronics because of high energy density, no memory effect, long cycle life, and low self-discharging.<sup>12,19-</sup>

<sup>21</sup> Sony first made lithium ion batteries commercially available in 1991.<sup>22</sup> Since then its share of secondary battery market has skyrocketed because of its high energy to weight ratio compared to

other secondary batteries and low maintenance required for long battery life. Lithium ion batteries are also relatively safe compared to other secondary batteries because of the lack of free lithium. Instead of free lithium, lithium is usually combined with other materials to form the metal oxide used for the cathode. The most popular commercially used metal oxides are lithium cobalt oxide ( $\text{LiCoO}_2$ ), lithium iron phosphate ( $\text{LiFePO}_4$ ), and lithium manganese oxide ( $\text{LiMn}_2\text{O}_4$ ).<sup>23,24</sup> The structures for these metal oxides are illustrated in Figure 1-3 and their properties listed in Table 1-1.

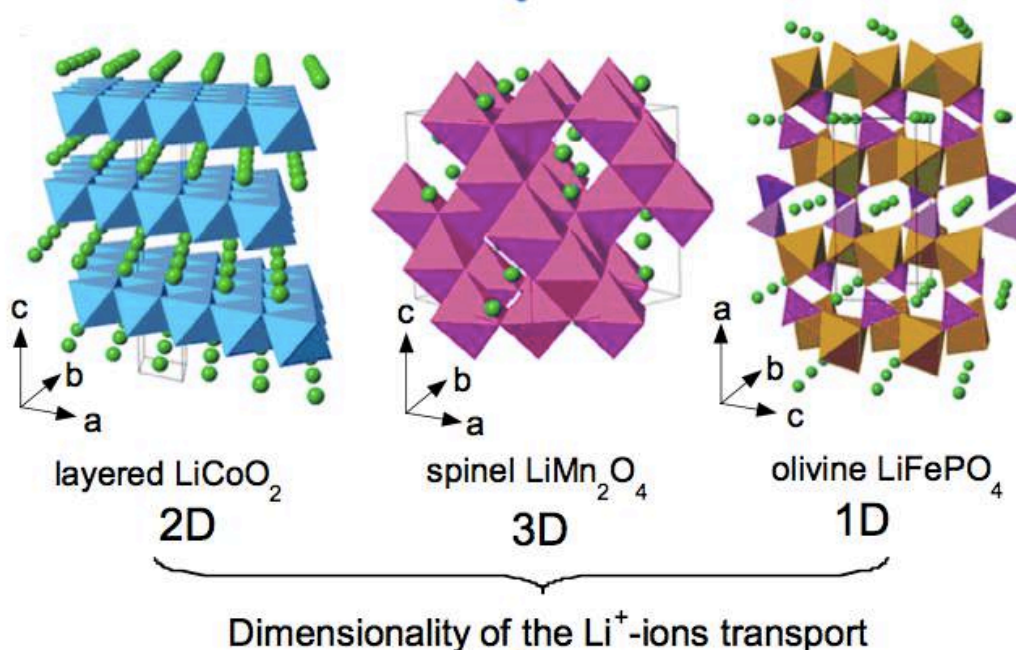


**Figure 1-3** Crystal structure of the three lithium-insertion compounds in which the  $\text{Li}^+$  ions are mobile through the 2-D (layered), 3-D (spinel) and 1-D (olivine) frameworks.<sup>25</sup>

The anode is usually made up of carbon graphite. The electrolyte consists of one or more organic complexes such as ethylene carbonate (EC), diethyl carbonate (DMC), propylene carbonate (PC), dimethyl carbonate (DMC), and ethyl methyl carbonate (EMC).<sup>26,27</sup> Dispersed in the organic electrolyte is a lithium salt such as lithium hexafluorophosphate ( $\text{LiPF}_6$ ), lithium hexafluoroarsenate monohydrate ( $\text{LiAsF}_6$ ), lithium perchlorate ( $\text{LiClO}_4$ ), lithium

tetrafluoroborate ( $\text{LiBF}_4$ ), and lithium triflate ( $\text{LiCF}_3\text{SO}_3$ ).<sup>27</sup> A schematic of the components and typical reactions in a lithium battery is shown in Figure 1-4.

Cathode Material	$\text{LiCoO}_2$	$\text{LiFePO}_4$	$\text{LiMn}_2\text{O}_4$
Crystalline Structure	Layered	Olivine	Spinel
Average potential (V vs. $\text{Li}^0/\text{Li}^+$ )	4.2	3.45	4.1
Specific Capacity Theoretical (Practical)	272 (140)	170 (160)	148 (120)
Specific Energy	0.518	0.495	0.400

**Table 1-1** Properties of various cathode materials.<sup>25</sup>

A lithium ion battery works according to an intercalation mechanism. When a battery is discharged, the lithium ions intercalated in the graphite anode flow to the cathode through the electrolyte. For the battery to be charged, an external power source is required, forcing the electrons to reverse the reaction flowing from the positive electrode to the negative electrode. These are reversible and can be done over a thousand times over the lifetime of the battery.

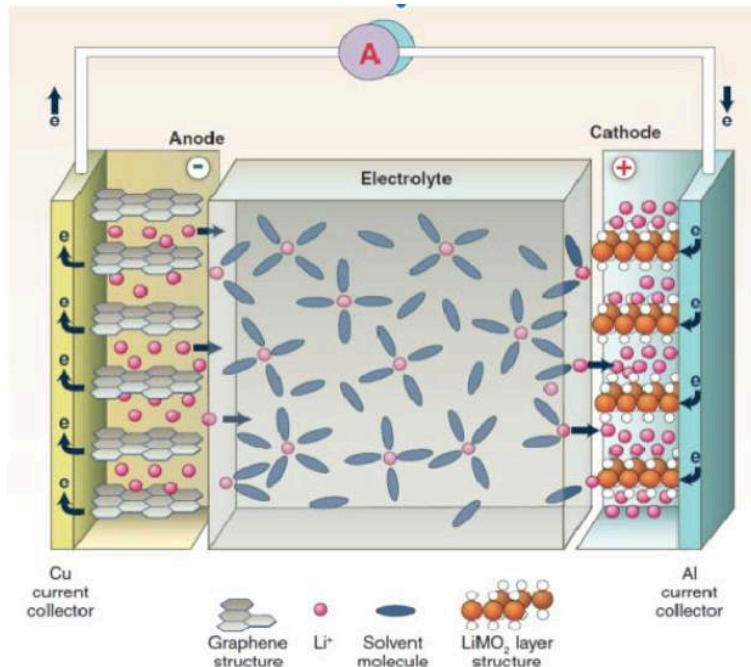


**Figure 1-4** Schematic of a Lithium ion battery. Consisting of a positive electrode (cathode), negative electrode (anode), electrolyte and other materials<sup>28</sup>

## 1.2 Overview of Separators

### 1.2.1 Introduction on the separator

The separator is a physical barrier within the battery that is placed between the positive and negative electrodes. It prevents contact between the anode and cathode, thus preventing short-circuiting. It also acts as an electrolyte reservoir in systems that require a liquid electrolyte, aiding in the ionic transport of ions between the two electrodes. Though the separator is not involved in the electrochemical reaction within the battery, its structure and properties can affect battery properties such as capacity retention, safety, energy and power density. An ideal separator should be electrochemically stable over the operation cycle of the battery, excellent mechanical and thermal properties, good ionic conductivity, easily wetted by electrolyte and able to retain the electrolyte. Safety and cost also need to be taken into account when developing separators.

## **1.2.2 Requirements for lithium-ion battery separators**

### **1.2.2.1 Thickness**

An ideal separator should be infinitesimally thin as to offer no resistance to ionic transport within the cell.<sup>29</sup> A thin separator will show high ionic conductivity and power density. On the other hand, a separator that is too thin will lack the mechanical strength required to have a safe separator and continuous cell assembly. A compromise must be reached to ensure a sturdy separator without too much resistance within the cell. Most commercial separators have a thickness  $\leq 25 \mu\text{m}$  for general use batteries and  $\leq 40 \mu\text{m}$  for EV application.<sup>30</sup>

### **1.2.2.2. Electrochemical Stability**

Conditions within a rechargeable cell can be harsh; a good separator should be able to withstand harsh chemical conditions within the battery. As a battery goes through charging and discharging, there are strong reduction and oxidizing conditions through which the separator should maintain its dimensional and mechanical stability. The separator must be able to withstand the strong oxidizing positive electrode and the corrosive nature of the electrolyte at temperatures as high as  $75^{\circ}\text{C}$ .<sup>29</sup>

### **1.2.2.3. Porosity and Pore Size**

The pore size of a separator is a key component. The pore sizes within the separator should be small enough as to block the penetration of particles, including active material that has gotten loose from the current collector. Uniform pore size can also aid in the prevention of dendrite formation on the separator as well as maintaining stable battery performance.<sup>28,31</sup>

The porosity within a separator can have an influence on the on the electrolyte uptake of the separator as well as the ionic conductivity. A separator with low porosity leads to high resistance within the cell impacting the amount of liquid electrolyte present between the anode and cathode. Similarly, membranes with low porosity will have a low effective diffusivity. The effective diffusivity for porous membranes is defined as

$$D_e = \frac{D\varepsilon}{\tau} \quad (1)$$

where  $D_e$  is the effective diffusivity defined as the diffusion through a pore space of a porous media,  $D$  is the diffusion coefficient,  $\varepsilon$  is the porosity, and  $\tau$  is the tortuosity. As the porosity of the separator increases, the ability of the ions to freely across the membrane increases thus improving the ionic conductivity. The actual porosity of a membrane is determined by the weight before and after the absorption of a liquid as in the following equation:

$$P = 1 - \left(\frac{W}{\rho \cdot V}\right) \quad (2)$$

where  $W$  is the dried membrane weight,  $\rho$  the membrane density, and  $V$  the apparent volume of the membrane.

#### 1.2.2.4. Mechanical Stability

Most batteries are subjected to some kind of mechanical stress during the drawing of the membrane or being wound in a battery. It is important that the membrane maintain its mechanical stability during these processes. While the separator is being wound under tension it is important that it does not elongate significantly as not to shrink in the transverse direction. Separators used in wound cells are susceptible to particle penetration. If electrolyte material penetrates across the separator this could lead to short-circuiting of the battery. Therefore it's

important that a separator have high puncture strength. The puncture strength is defined as the maximum load required for a needle to penetrate a given separator.

#### **1.2.2.4. Thermal Stability**

As batteries are being used in more EV/HEV, it is important that separators do not melt or shrink at high temperatures. Water can be poisonous inside a lithium battery, so it is important to dry all components at 80°C for at least an hour. Therefore separators should be able to withstand those conditions without any change in mechanical strength or dimensional change.

#### **1.2.2.5. Wettability and Electrolyte Uptake**

Electrolyte absorption into the porous membrane is required for the transport of ions between the two electrodes therefore the wettability of the membrane is an important factor. The fast absorption of liquid electrolyte facilitates the process of electrolyte wetting in the battery assembly. The ability of the separator to uptake and retain a significant amount of electrolyte will affect its ability to lower the resistance within the cell and achieve high ionic conductivity. The wetting speed depends on the type of the hydrophobicity of the material, porosity, and pore size of the separator.

#### **1.2.2.6. Permeability**

The separator must not affect the electrical performance of the battery. Though the separator is a necessary component within the battery, it has negative impacts on the resistance of the electrolyte. The permeability of a separator is defined by the MacMullin number, ratio on the resistivity of the separator wet with electrolyte vs. the resistivity of the separator alone. The presence of the separator increases the MacMullin number by a factor of 6-7, which a MacMullin number of 10-12 being suitable for batteries used in commercial devices. In order for a battery to have a long life cycle, it is preferable for it to have a low MacMullin number. The MacMullin number is proportional to air permeability and thus it can be expressed by the Gurley value. The

Gurley value is defined by the time required for air to pass through a unit area under a fixed pressure.

#### **1.2.2.7. Dimensional Stability**

A good separator should lay flat and not curl at the edges when unwound or immersed in electrolyte. The separator should also maintain its shape after mechanical tension and at elevated temperatures. Any bow or skew in the membrane can cause misalignment during construction of the battery leading to poor cell performance.

#### **1.2.3. Types of separators**

Separators for lithium-ion batteries can be divided into three main categories: i) microporous polymer membranes, ii) non-woven mats, and iii) composite membranes. The most widely used commercial membranes are polyolefin membranes manufactured by either a dry or wet process because of their proven performance in application. Despite their advantages, there are many limitations to polyolefin membranes, which researchers have tried to address with non-woven and composite membranes.

##### **1.2.3.1 Microporous membranes**

As previously mentioned, microporous membranes are usually made with polyolefin polymers such as polypropylene (PP), polyethylene (PE) or a combination of the two polymers. These membranes begin with the manufacturing of a polymer film that eventually stretched to create micro-pores and slits. The membranes made from the dry process form pores that are slit like in shape and are suitable for high power density batteries because of the straight and open pore structures. Membranes created with the wet process have a more elliptical and interconnected pore structure suitable for long life cycle batteries.

The dry process<sup>32-36</sup> usually begins with the extrusion of a uniaxial lamellar structured polyolefin film (Figure 1-5a). The extruded film shows a stacked lamellar structure along the transverse direction. This precursor film is annealed at a temperature slightly lower than the polymer's melting point to increase the crystallinity and crystal size of the polymer membrane. The stretching step is composed of a cold stretch, hot stretch, and relaxation to reduce internal stresses in the membrane. The annealed film is first cold-stretched; pulling the lamellar stacks apart creating the needed pores (Figure 1-5b). The porosity of the membrane will depend on the percent crystallinity of the annealed film, as pores will only form in the amorphous regions. The hot stretch increases pore sizes using a higher temperature and a slower strain rate. Polyolefin membranes can be stretched either uniaxially<sup>32,33</sup> or biaxially<sup>37,38</sup>, though to date, most membranes are stretched uniaxially. The advantage of the dry process technique is the lack of solvents used. However since it is only stretched uniaxially, it is relatively weak in the lateral direction. Commercially available membranes made by the dry-stretch technique include Celgard<sup>39</sup> and Ube<sup>40</sup>.

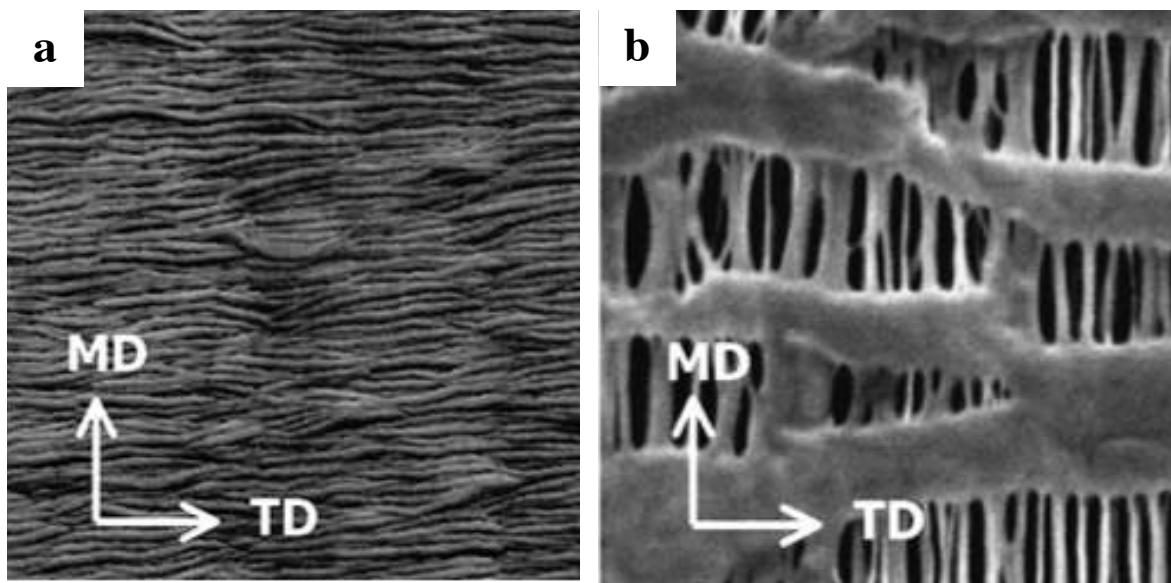


**Figure 1-5** Structure of dry process made polyolefin separators before (a) and after (b) stretching<sup>41</sup>

The wet process<sup>42-44</sup>, also known as the phase inversion process, consists of three steps: mixing, extrusion and stretching steps. Polymer resin such as ultrahigh molecular weight polyethylene (UHMWPE), hydrocarbons like paraffin oil, and other additives are mixed and heated to form a solution. The solution is then extruded into a sheet, and then volatile solvents are used to remove the liquids and hydrocarbons and create the micropores. A stretching step can be added before or after the extraction step. The membranes made by stretching after extraction showed larger pore size and the wider distribution of pore size than those prepared by stretching before extraction step. The structure and properties of membranes depend on the composition of the solution and the extraction of solvents. Examples of membranes manufactured using the wet process can be seen in Figure 1-6. Commercial membranes made using this technique include Setela<sup>30</sup> and Teklon<sup>30</sup>.

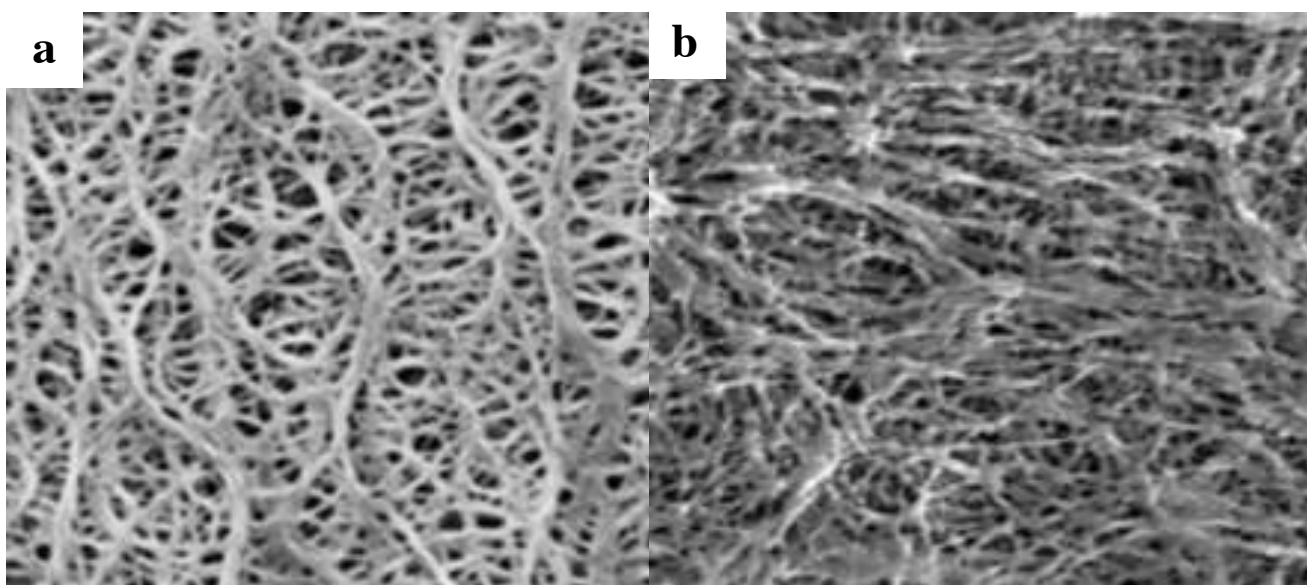


**Figure 1-6** Microstructure of various membranes created via the wet process procedure: (a) Celgard<sup>45</sup>, (b) Tonen<sup>3</sup>

A major limitation of polyolefin membranes is its poor miscibility with polar electrolytes because of the low polarity of the polymer backbone. In order to address this limitation, researchers have manufactured microporous membranes from a variety of polymers including

PAN, PMMA, and PVDF. PAN is utilized because of its high thermal and electrochemical stability and good compatibility with electrodes. PMMA is utilized for its good mechanical strength and its high affinity for polar electrolyte. PVDF membranes demonstrate good wettability, dimensional stability, and excellent mechanical strength because of high crystallinity, approximately 40% to 60%.

Phase inversion is commonly used to create microporous separators using the previously mentioned polymers. The phase inversion process involves casting a thin film of the polymer and soaking it in a non-solvent coagulation bath. The pores are formed by precipitation of the polymer by solvent exchange, similar to the wet-process described previously. The phase separations and solidification of the polymer results in an asymmetric pore structure than can be affected by depending on the type and concentration of polymers, temperature, thickness, and solvent type.

Han *et al.*<sup>46</sup> produced a variety of PVDF microporous membranes to study the effect of amount of additives, polymer type, concentration of solution and ratio of water/ethanol on the morphology of the final membrane. Results indicate increasing the ratio of ethanol in the solution increases the porosity of the system and the upper structure was transformed into a sponge-like structure. Mechanical testing showed there was a positive impact on the mechanical strength of the membrane when up to 25 percent of ethanol as added, however it decreased after that point most likely due to the high porosity of the system. Small amounts of hydrophilic additives showed an improvement in the morphology and mechanical strength of the membrane.

However, there are a few drawbacks not seen with the other membranes. The F-C along the PVDF backbone can react with lithium and lithiated graphite to form more stable LiF and

>C=CF– unsaturated bonds, which can negatively affect battery performance. In addition, PVDF can be soluble in certain liquid electrolytes which can affect its mechanical strength.<sup>47</sup>

In addition, the semi-crystalline nature of PVDF leads to a high crystallinity of the membrane, which can lower its ionic conductivity. The crystalline region of a polymer membrane can hinder the migration of lithium ions resulting in low capacity and poor C-rate values.<sup>28,29,48,49</sup> In order to address this issue, copolymers were added into the PVDF membranes. These copolymers include poly(vinylidene fluoride-co-hexafluoropropylene) (PVDF-co-HFP), PVDF/PMMA, and PVDF/P(MMA-co-PEGMA) among others.

Shi *et al.* prepared PVDF-co-HFP membranes that showed processing conditions such as temperature and composition of the coagulation bath have an effect on the porosity of the system.<sup>50</sup> Their findings show that a good separator should have pore sizes less than one micron and porosity higher than 80 percent. A small pore size distribution was also ideal for maintaining good electrolyte and ionic conductivity. Li *et al.*<sup>47</sup> demonstrated that fabrication of PVDF/P(MMA-co-PEGMA) membranes decreases the crystallinity of the membranes from 46 to 38 percent resulting in an increase in electrolyte uptake and ionic conductivity. Similar results are seen when PVDF-co-HFP is mixed with PEG to create PVDF-co-HFP/PEG. Hwang *et al.*<sup>51</sup> found there was an increase in membrane porosity with an increase in PEG percentage. This increase in porosity led to an increase in ionic conductivity of the membrane and improved capacity in Li/LiCoO<sub>2</sub> half cells. However, as the PEG content is increased above 50 percent there is leakage of electrolyte solution from the membrane resulting in poor cycling performance. Subramania *et al.*<sup>52</sup> created PVDF-co-HFP/PAN membranes which showed an increase in ionic conductivity with increasing PAN content. The polymer blend resulted in higher specific capacity than using PAN or PVDF alone as a membrane. Using thermally induced phase

separation, Ma *et al.*<sup>53</sup> created PVDF/PMMA blend microporous membrane. SEM images (Figure 1-7) show the pores created are uniform and well-connected. An increase in PMMA inclusion lead to decreased crystallinity, increased porosity of then membrane, increase in electrolyte uptake and enhanced ionic conductivity.

Jung *et al.*<sup>54</sup> made microporous PAN/poly(vinylpyrrolidone) (PVP) membranes and showed the asymmetric structure of the membranes on the top and bottom increased with PVP content. There was also an increase in membrane permeability as PVP content decreases. PAN/PMMA fabricated using phase inversion induced ultrasonic humidifier by Pu *et al.*<sup>55</sup> leading to more uniform pore sizes across the cross section of the membrane compared to porous membrane prepared by conventional water bath coagulation technique. These membranes had a ionic conductivity of  $2.52 \times 10^{-3}$  S/cm at room temperature when gelled with 1 M LiPF<sub>6</sub>/EC-DMC (1:1, vol.%) electrolyte solution. Cycling tests of a Li metal/graphite half-cell showed 88% capacity retention after 50 cycles.

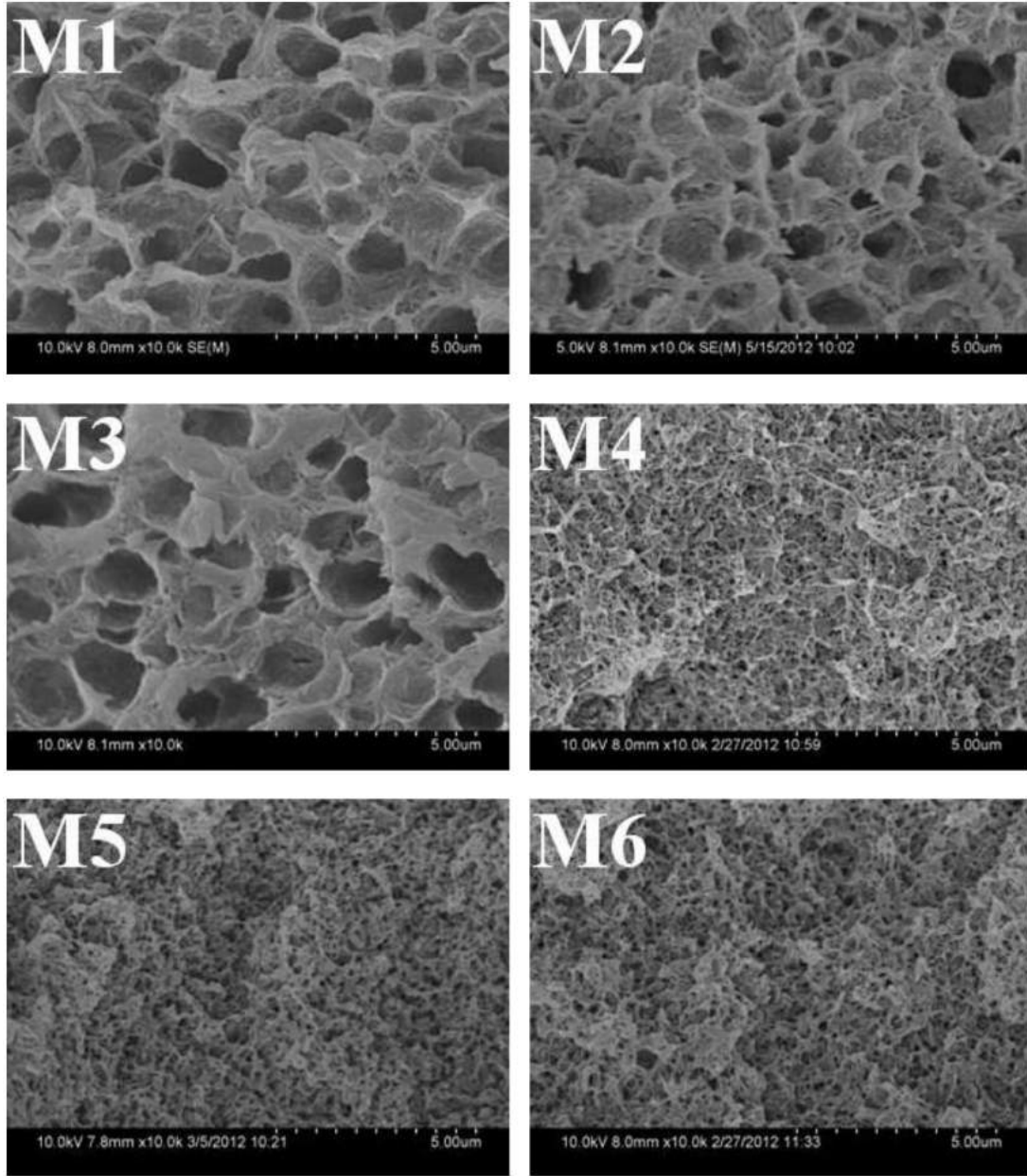


**Figure 1-7** Cross-section SEM micrographs of blend membranes with different weight ratios of PMMA/PVDF.<sup>53</sup>

### 1.2.3.2 Nonwoven Separators

To overcome the limitation of microporous membranes researchers have begun investigating the use of non-woven membranes as separators in lithium ion batteries. Non-wovens are defined as a manufactured sheet, web, or mat of aligned or randomly oriented fibers

bonded chemically or mechanically bonded together. Non-wovens can be made from natural sources such as cellulose and its derivatives, as well as synthetic sources. Non-wovens can be made using a variety of methods including meltblown method, wet laid method and papermaking process. However, for the non-wovens used in lithium-ion batteries, the most widely used method is electrospinning. Electrospinning creates ultra-thin fibers forming an interconnected highly porous membrane. Electrospun nanofiber membranes have high porosity, small pore size, high permeability and large surface area. The highly porous nature of electrospun networks helps prevent the growth of dendritic lithium in rechargeable batteries. The high porosity of electrospun membranes (60-80%) leads to higher effective diffusivity of the membrane leading to high ionic conductivity. Electrospun membranes can be made from a variety of synthetic polymers including polyamide (PA), polytetrafluoroethylene (PTFE), polyethylene terephthalate (PET), polyacrylonitrile (PAN), polyvinylidene fluoride (PVDF) and so forth.

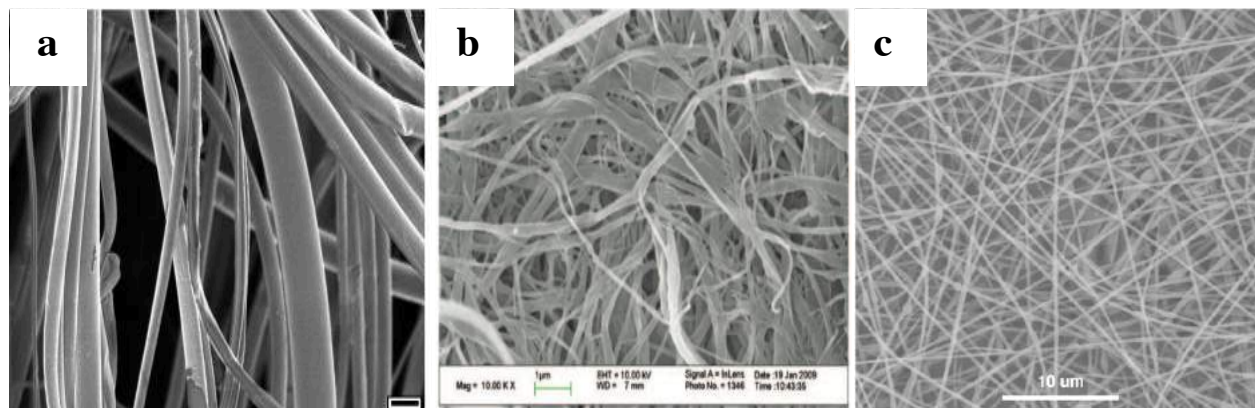


**Figure 1-8** Images of non-wovens created by a) melt-blown method<sup>56</sup> b) wet laid method<sup>57</sup> c) electrospinning<sup>58</sup>

Hao *et al.*<sup>59</sup> investigated the use of PET electrospun non-woven membranes in 2007. The membrane displayed excellent thermal, mechanical and electrochemical properties. Due to the

high porosity of the membranes, 89% compared to 40% porosity of Celgard, the PET membranes exhibited almost 3 times the electrolyte uptake of the polyolefin Celgard membrane. The increase in porosity and electrolyte uptake lead to in 10 fold increase in the ionic conductivity, 2.3 mS/cm compared to 0.3 mS/cm of Celgard. When the membranes are placed in Li/ LiFePO<sub>4</sub> half cells, the excellent electrochemical performance of the PET membrane is exhibited. PET membrane shows higher initial discharge and superior capacity retention after 50 cycles.

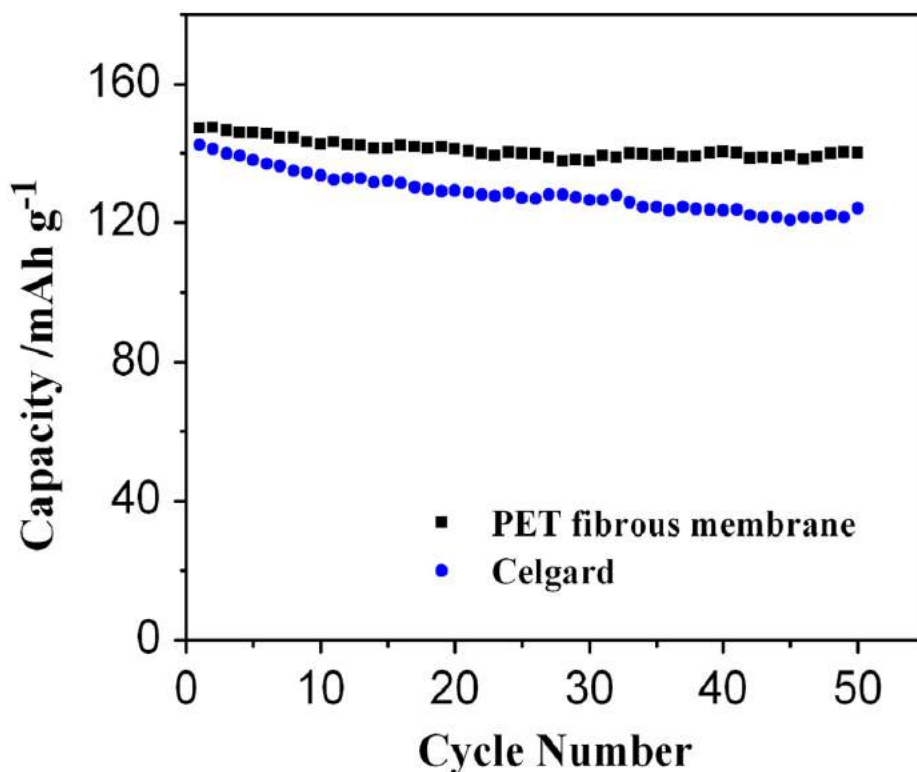


**Figure 1-9** The cycle performances of Li/LiFePO<sub>4</sub> cell using electrospun PET fibrous membrane and Celgard membrane.<sup>59</sup>

PAN based electrospun membranes have been investigated by researchers because of the superior characteristics in mechanical stability and lithium ion transport demonstrated by PAN membranes. Studies show the nitrile group (C-N ) of the polymer chain hinder the arrangement of the polymer chain during electrospinning process.<sup>60</sup> This leads to fibers with more amorphous

regions, allowing for the easier flow of the ions across the membrane. Due to both the increased porosity and more hydrophilic nature of PAN compared to polyolefins there is a dramatic increase in the electrolyte uptake and ionic conductivity. In addition, the highly polar nitrile group of the PAN polymer interacts favorably with the lithium salt, further increasing the ionic conductivity..<sup>61-63</sup> Increase in ionic conductivity leads to superior electrochemical performance within the battery compared to polyolefin microporous membranes. Cho *et al.*<sup>62,64</sup> reported PAN electrospun membranes were much more thermally stable under a hot oven test. In addition, they also delivered higher capacity at high C-rates compared to PE and PP membranes. Combining PAN with PVDF, Gopalan *et al.*<sup>65</sup> created PAN/PVDF membranes with various loadings of PAN. The membranes with 25% PAN had the highest ionic conductivity and cycling performance.

Polyimides have also been investigated because of their superior thermal stability, low dielectric constants and inertness to solvent and radiation resistance.<sup>66</sup> Maio *et al.* manufactured electrospun polyimide separators with very promising results. In comparison to Celgard, the PI membranes showed better thermal stability, lower internal resistance and more favorable electrolyte interactions. When the membranes are placed in  $\text{Li}_4\text{Ti}_5\text{O}_{12}$  half-cell, there is a 100% capacity retention over 100 cycles at a C/5 charging rate. When the rate capability is tested, cells showed a 62% retention at 10C charging rate compared to 45% seen for Celgard. Most testing is done at room temperature, however Jiang *et al.*<sup>67</sup>, performed their cell testing between 80-120°C using both PI and Celgard membranes. The impact of using PI as the separator membrane is immediately apparent. Oven tests show the PI membrane maintains its shape at 150°C for an hour, while the Celgard membrane curls and shrinks, losing its dimensional stability. Ionic conductivity increases from 0.89 mS/cm at 25 °C and 1.73 mS/cm at 120 °C. At 80°C, after 50

cycles, the PI membrane has a capacity retention of 91% compared to 80% of Celgard. As the temperature is raised to 120°C the Celgard membrane is not able to be stably charged, while the PI membrane achieved an initial capacity of 142 mAh/g and maintained an 86% retention after 50 cycles.

Non-woven PVDF membranes are another commonly used separator because of its affinity for the electrolyte and stable electrochemical performance. The strong electron withdrawing functional groups (-C-F) allows the membranes to have a high dielectric constant. This enables PVDF membrane to provide better dissolution of lithium salts to support higher concentration of charge carriers. The effect of fiber orientation on the mechanical properties were investigated by Costa *et al.*<sup>68</sup> As the fibers become more oriented there is an increase in the tensile strength of membrane especially for the electrolyte soaked membrane. However, the oriented fibers showed lower ionic conductivity membrane due to higher tortuosity. Choi *et al.*<sup>69</sup> fabricated PVDF electrospun separator membrane to investigate their thermal and electrochemical properties. After being immersed in electrolyte, the membranes were still able to maintain good mechanical strength and had good electrolyte uptake because of the three-dimensional network structure with fully interconnected network. In addition, the gel phase formed by swelling of the fibers lead to improvement in the electrochemical stability of the membranes. Gao *et al.*<sup>70</sup> prepared PVDF separator membranes for the use in lithium metal batteries. Compared to commercial polyolefin membranes, the PVDF membranes showed better affinity for the lithium metal and increased electrolyte uptake. Due to this, the membranes showed 95 percent capacity retention compared to 85 percent retention of Celgard at C/2 charge rate after 100 cycles.

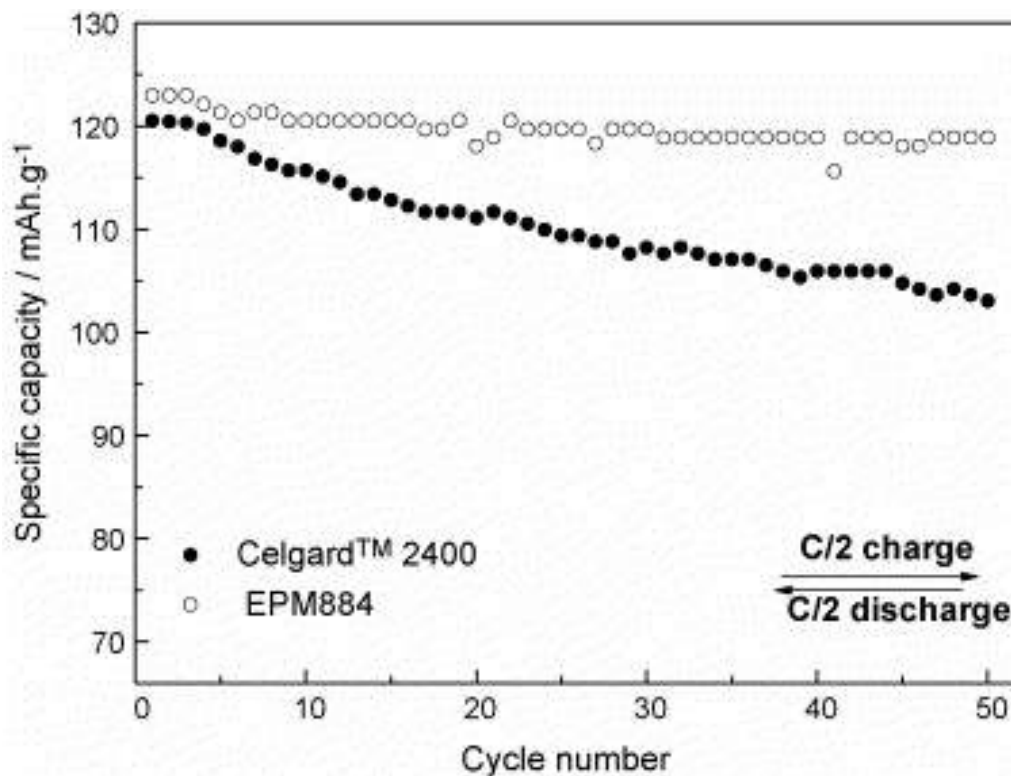


**Figure 1-10** Cycle performance of the cells with Celgard™ 2400 and PVDF (EPM884) at room temperature.

Researchers have also electrospun PVDF copolymers in an effort to reduce the crystallinity of the PVDF membrane. Raghavan *et al.*<sup>71</sup> compared the electrochemical performance of PVDF-HFP membranes made by phase inversion and electrospinning. The electrospun membranes demonstrated superior electrolyte uptake compared to the phase inversion membrane due to higher porosity (Figure 1-11). The ionic conductivity is 4.32 mS/cm which is about five times greater than that of phase inversion membrane (Figure 1-12). Ionic conductivity resulted in higher initial discharge capacity and better cycleability. Kader *et al.*<sup>72</sup> prepared poly(vinylidene fluoride)-graft-poly(tert-butyl acrylate) (PVDF-g-tBA) membranes using the electrospinning technique. The graft copolymer reduced the crystallinity of the membrane resulting in improved ionic conductivity and cycling performance.

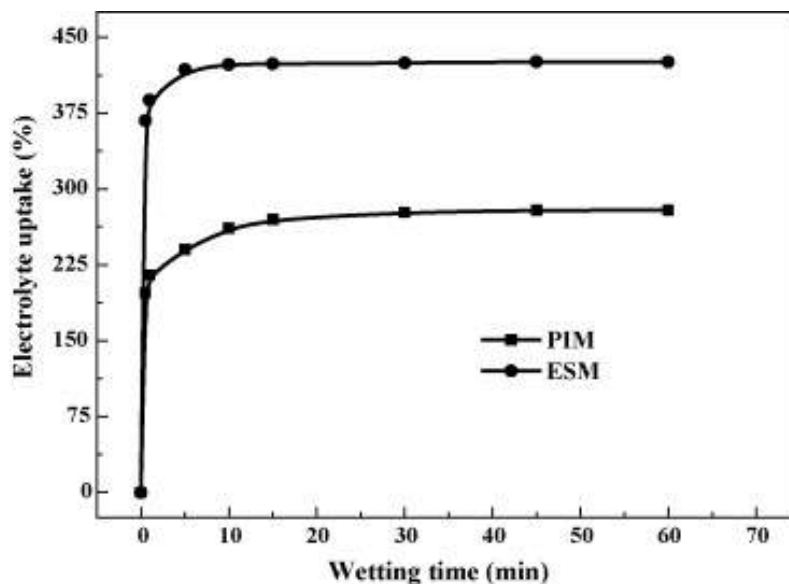


**Figure 1-11** Electrolyte uptake (%) of PIM and ESM (liquid electrolyte: 1 M LiPF<sub>6</sub> in EC/DMC).

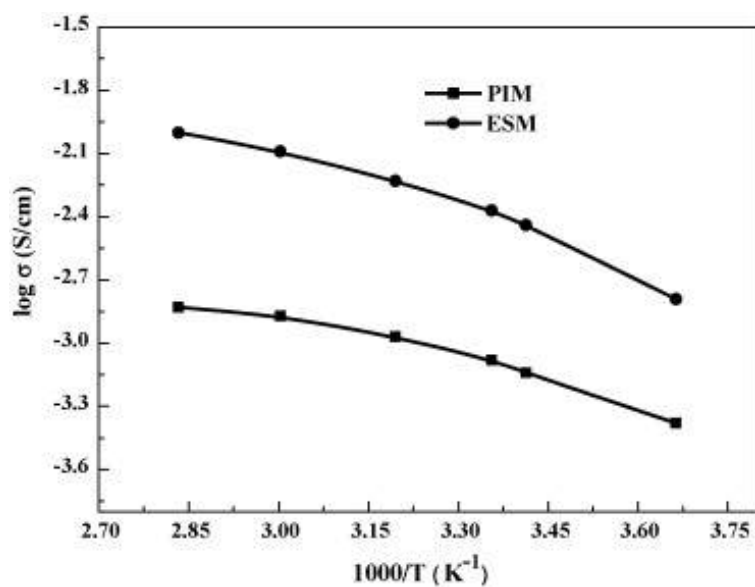


**Figure 1-12** Effect of temperature on the ionic conductivity of P(VdF-co-HFP) membranes (liquid electrolyte: 1 M LiPF<sub>6</sub> in EC/DMC).<sup>72</sup>

Researchers have also created trilayer separators in order to improve the electrochemical performance of electrospun membranes<sup>60,73</sup> PVdF-HFP/PVC/PVdF-HFP based- trilayer separators have increased electrolyte uptake, increased mechanical and thermal stability due to the combination of the two polymers. Trilayer membranes created with PAN nanofibers and

PVdF-HFP nanofibers also exhibited high electrolyte uptake and good ionic conductivity because of the high porosity of the membranes. Assembled cells shows high electrochemical stability and stable cycling performance.

### 1.2.3.3 Composite Separators

To further increase the thermal stability and ionic conductivity of membranes, researchers have also included inorganic ceramic fillers into the electrospun membranes. Fillers usually used include barium titanate ( $\text{BaTiO}_3$ ), aluminum oxide ( $\text{Al}_2\text{O}_3$ ), and silicon dioxide ( $\text{SiO}_2$ ). The incorporation of ceramic fillers lead to an increase in thermal stability by increasing the melting point of the polymer, an increase in mechanical stability, increase in liquid electrolyte uptake and high electrolyte retention. The incorporation of ceramics can be done through a variety of methods including dip-coating, rolling, or incorporating the ceramic directly into the polymer network.

#### 1.2.3.3.1 Inorganic particle-coated or filled microporous membrane separators

Thin layers of inorganic particles applied onto microporous membranes can improve the thermal stability and wettability of the membranes. Jeong *et al.*<sup>74</sup> coated both sides of PE membranes with a  $\text{SiO}_2$ /PVDF-HFP to improve the thermal stability of the membrane, reducing thermal shrinkage from 94 to 77 percent compared to the pristine PE membrane. Fu *et al.*<sup>75</sup> coated PE membranes with varying amounts of  $\text{SiO}_2$  particles.  $\text{SiO}_2$  loading up to 40% showed a gradual increase in electrolyte uptake. There was also an improvement in thermal shrinkage similar to results discussed by Jeong *et al.*

Takemura *et al.*<sup>76</sup> investigated the effect of particle size on the performance of  $\text{Al}_2\text{O}_3$  coated microporous membranes. The addition of both the 0.01  $\mu\text{m}$  and 0.3  $\mu\text{m}$  size particles decreased the pore size distribution of the membrane compared to a bare PE membrane. Results

showed the 0.01  $\mu\text{m}$  showed excellent cycling properties compared to the uncoated membrane and the 0.3  $\mu\text{m}$  particle size coated membrane. This improvement is attributed to small pore sizes provided by the 0.01  $\mu\text{m}$  membrane allowing it to trap more electrolyte.

Using nanosized  $\text{Al}_2\text{O}_3$  powder and hydrophilic poly(lithium 4-styrenesulfonate) binder to coat a microporous membrane, Choi *et al.*<sup>77</sup> were able to improve the thermal stability of the microporous membrane. In addition, due to high hydrophilicity of the polymer binder and large surface area of the small ceramic particles, the separators show good wettability with the electrolyte. Improved wettability led to increases electrolyte uptake, higher ionic conductivity and more stable cycling performance.

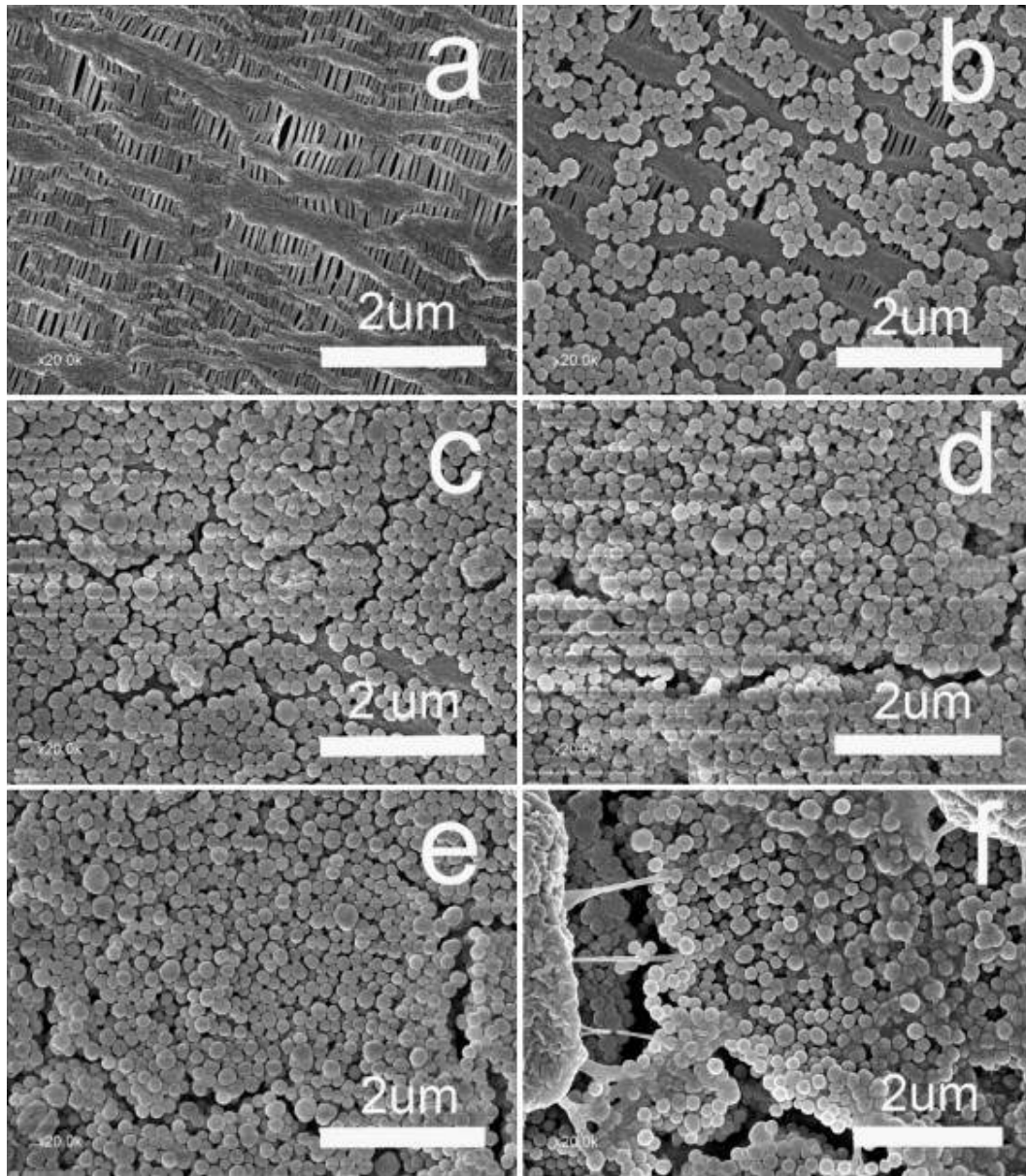


**Figure 1-13** SEM images of separator surface with and without SiO<sub>2</sub> particles coating. (a) Without coating, (b) 8%, (c) 20%, (d) 27%, (e) 45%, (f) 55%.<sup>75</sup>

Polymer binder can have a negative side effect on the ion transport of batteries containing separators with polymer binders. Kang *et al.*<sup>78</sup> used an integrative mussel- and diatom-inspired approach to trigger the growth of ceramic onto the surface of PE separators. There is an increase in electrolyte uptake from 96% to 121% and an increase in ionic conductivity from 0.23 mS/cm to 0.35 mS/cm due to the increased electrolyte uptake. C-rate tests of full cell LiMn<sub>2</sub>O<sub>4</sub>/separator/graphite cells show the membranes containing SiO<sub>2</sub> had the best capacity retention at high charge rates, up to 15C.

Zhu *et al.*<sup>79</sup> grafted SiO<sub>2</sub> onto a PE membrane using electron beam irradiation. This technique did not alter the thickness or the porosity of the membrane. The addition of ceramic on to surface increased the thermal stability of the membrane increasing the melting temperature from 139°C to 143°C. The ionic conductivity of the membrane increased from 0.32 mS/cm for the bare PE membrane to 0.45 mS/cm for the ceramic grafted membrane. The Li/ceramic-grafted-separator/LiFePO<sub>4</sub> cell also showed lower electrochemical resistance compared to the pristine cell. With the increase in current rate, the grafted membrane exhibited improved capacity retention.

In the presence of water, LiPF<sub>6</sub> can hydrolyze to create hydrogen fluoride (HF) which is one of the main sources of capacity fading in the cathode materials. Zhang *et al.*<sup>80,81</sup> used alkaline calcium carbonate (CaCO<sub>3</sub>) as their inorganic component in order to neutralize HF. CaCO<sub>3</sub> was combined with a Teflon emulsion in a 92 to 8 ratio to create ceramic films. CaCO<sub>3</sub> and Teflon emulsion were thoroughly mixed with small amounts of ethanol and hot-rolled to create a self-standing membrane. Resultant membranes had ionic conductivities ranging from 2.5-4 mS/cm. Li/LiMn<sub>2</sub>O<sub>4</sub> cells containing the composite membranes show improved cycling

performance over Celgard membrane. This improvement is attributed to the membranes ability to neutralize the acidic products in the cell.

#### 1.2.3.3.2 Inorganic particle-coated or filled non-woven membrane separators

Cho *et al.*<sup>32</sup> produced electrospun polyethylene-polypropylene sheath-core composite fibers coated with varying amount of silica powder using the air laid method. Results were then compared to microporous polyethylene-polypropylene Celgard membranes. Using the same material (PE/PP) but changing from microporous membrane to an electrospun membrane caused an immediate change in solvent-membrane interaction reducing the contact angle from 70° to 40°. After the silica powder was incorporated, the contact angle is reduced further to 20°. There is also an increase in ionic conductivity from 0.8 mS/cm to 1.0 mS/cm. These favorable changes led to an increase in capacity retention compared to Celgard and non-ceramic coated membranes.

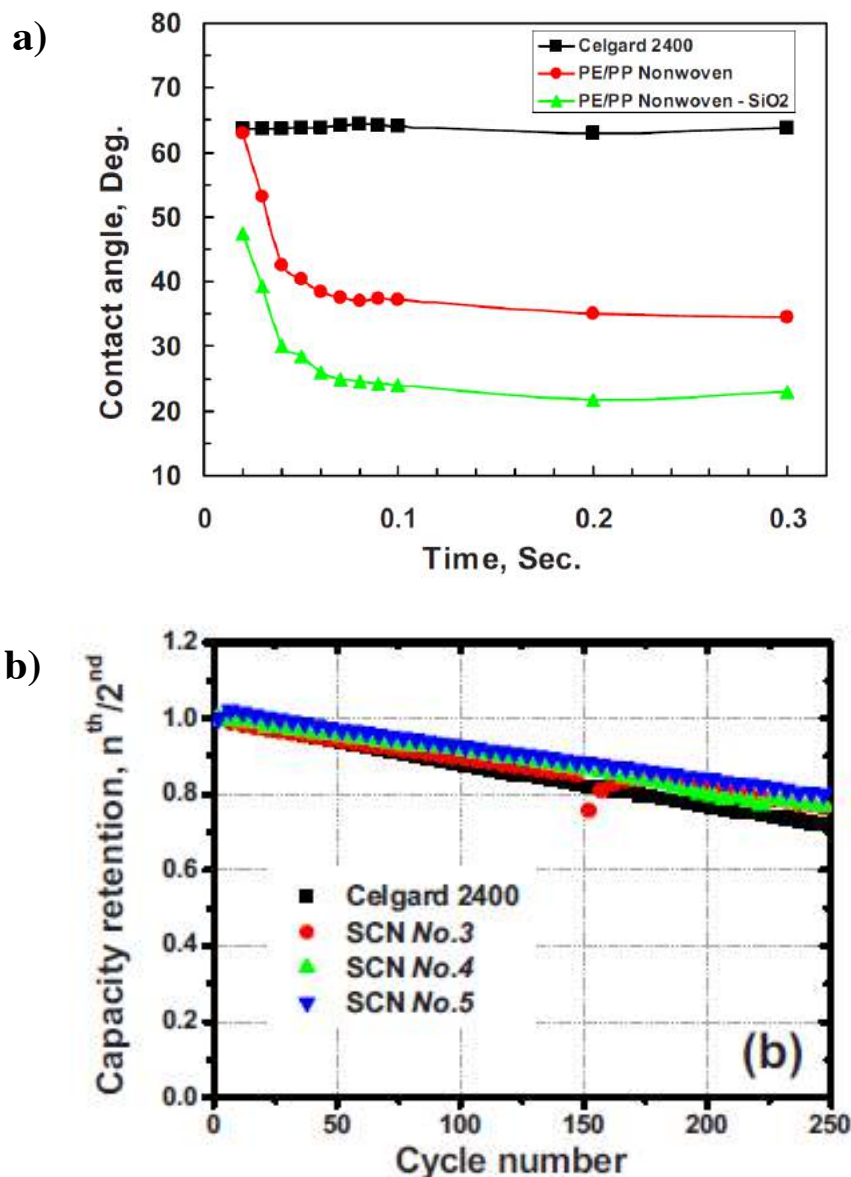


**Figure 1-14** a) The variation in contact angle between polyolefin microporous membranes and polyolefin nonwoven membranes with and without ceramic inclusion b) LiCoO<sub>2</sub>/graphite full cell performance of batteries with various membranes

Cho *et al.*<sup>83</sup> combined a PAN nonwoven with a ceramic-coated polyolefin separator using a hot press to overcome the shortcomings of the polyolefin separator. The new composite separator showed improved porosity and air permeability compared to the commercial separator. The PAN non-woven also improved the thermal stability compared Celgard as the membrane did

not shrink after being in a 150°C for an hour. When the composite separators were placed in LiCoO<sub>2</sub>/graphite full cells, the composites showed a 10 percent increase in capacity retention. Rate capability tests show superior performance of composite separators at all charge rates.

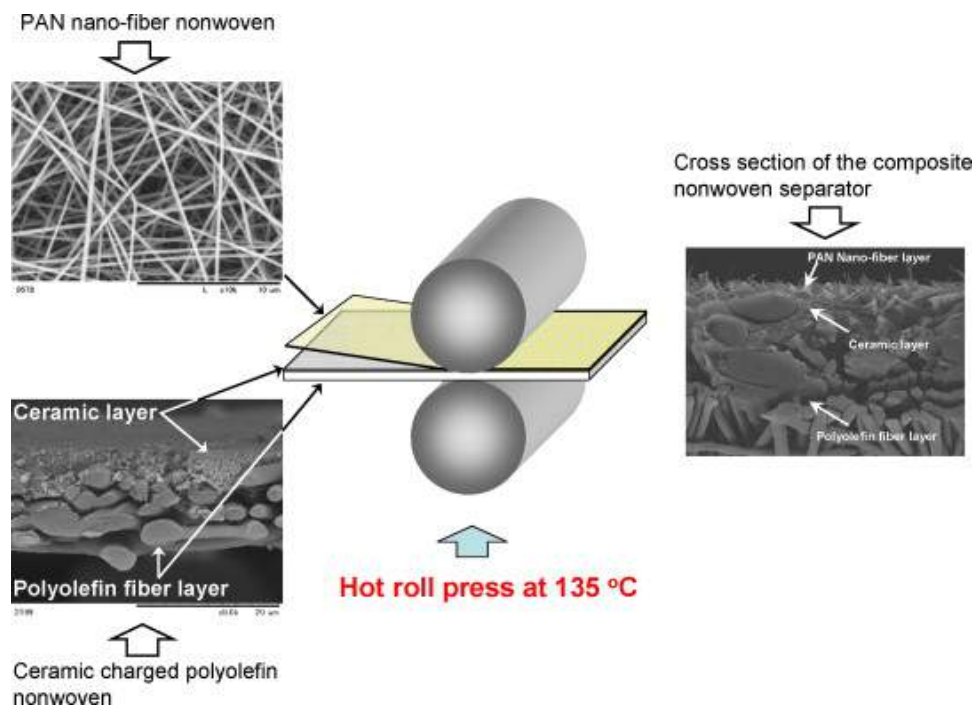


**Figure 1-15** Schematic depiction of the PAN/Celgard/silica membranes<sup>83</sup>

Sethupathy *et al.*<sup>84</sup> created superhydrophobic PVDF/fumed SiO<sub>2</sub> composite electrospun membranes. Ceramic loadings were low, ranging from 0 to 0.7 weight percent. The presence of ceramic of increased the surface roughness of the membranes, however there was no change in the diameter of the fibers. There is an increase in electrolyte uptake from 300% percent to 450% due to the presence of ceramic in the fiber. Ionic conductivity increased from  $0.242 \times 10^{-4}$  S/cm to  $7.731 \times 10^{-4}$  S/cm.

Using the dip-coating method, Zhang *et al.*<sup>85</sup> prepared silica coated polysulfonamide (SPN) nonwoven separator membranes. These membranes showed excellent wettability of the

SPN membrane as shown in Figure 1-16. The liquid electrolyte quickly wetted the SPN membrane in 10s and spread evenly over the membrane. The electrolyte uptake increased from 120% to 300% due to the SPN membrane being more lyophilic to the electrolyte. Cycling  $\text{LiCoO}_2$ /graphite cells shows superior cycling performance at 0.5C charge and discharge rates after 100 cycles. In addition, cells run at elevated temperatures,  $120^\circ\text{C}$ , demonstrated the importance of thermal stability for separator membrane. Cells made with Celgard could not charge and discharge while the SPN membranes maintained a 113 mAh/g in  $\text{LiFePO}_4/\text{Li}$  cells.

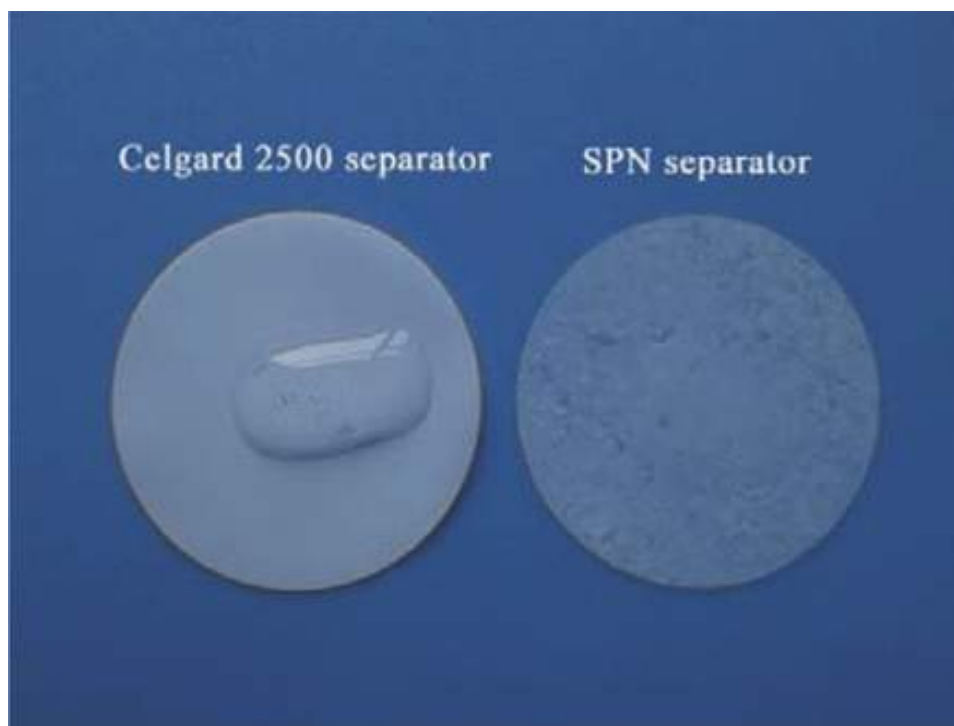


**Figure 1-16** Photographs showing liquid electrolyte (1 M  $\text{LiPF}_6$  in  $\text{EC}/\text{DMC} = 1/1$  v/v) wetting behavior of Celgard 2500 separator and SPN separator<sup>85</sup>

Yanilmaz *et al.*<sup>86</sup> made composite membranes by combining electrospinning and electrospaying techniques to produce silica/PVDF membranes. Silica inclusion varied from 0 wt% to 24 wt%. Increases in silica inclusion resulted in increased electrolyte uptake and ionic

conductivity. The increase in these properties is thought to be caused by silica particles helping to sustain tunneling structures and hold more electrolyte due to an increase in surface area. The increased ionic conductivity resulted in improved battery performance when membranes were placed in Li/LiFePO<sub>4</sub> half cells.

Instead of having the ceramic only on the outside of the fibers, Jung *et al.*<sup>87</sup> instead incorporated fumed silica within the PAN network with varying amounts of silica. Comparing the PAN/fumed silica composites to the neat PAN electrospun fiber saw a decrease in fiber diameter with increasing silica inclusion, along with an increase in porosity. There was also an increase in electrolyte uptake and ionic conductivity. Jung *et al.* showed, however, that there was a limit to the amount of fumed silica than can be used. All the previously mentioned trends occurred from 0 to 12wt% fumed silica; when the amount was increased further to 15wt% there was a reversal in all the previously discussed trends.

Similarly Kim *et al.*<sup>88</sup> incorporated 0, 6, 10 wt% of SiO<sub>2</sub> into PVDF-HFP electrospun membranes. As the amount of silica increases, the average fiber diameter also increases. There is an increase in ionic conductivity from 2.3 mS/cm to 4.3 mS/cm when inorganic content is increased from 0 to 6 percent. However further increase in inorganic content leads to ionic conductivity falling to 3.4 mS/cm, most likely due to the agglomeration of silica particles at that high loading. The membranes with 6% SiO<sub>2</sub> also showed the most stable cycling performance, delivering the specific capacity of 170 mAh/g in Li/LiFePO<sub>4</sub> cells. The bare PVDF-HFP electrospun membrane had a specific capacity of 140 mAh/g.

Silica was also integrated into nylon 6,6 by Yanilmaz *et al.*<sup>89</sup> to create thermally-stable separator membranes. Similar to previously mentioned cases, the inclusion of ceramic increased the electrolyte uptake and ionic conductivity of the polymer composite membrane. In addition,

there is an increase in the tensile strength of the membrane, increasing the strength from 18 MPa to 22 MPa. Cycling performance of Li/LiFePO<sub>4</sub> half cell batteries show excellent cycling performance and capacity retention.

Liang *et al.*<sup>90</sup> introduced lithium lanthanum titanate oxide (LLTO) into PAN polymer matrix in 5 percent increments from 0 to 15 percent. As the LLTO content increases surface roughness increases and fiber diameter decreases due to altered surface tension, electrostatic repulsion and viscoelastic force caused by the presence of lithium-ion conducting LLTO particles. In addition, starting to 10 wt%, LLTO particle begin to agglomerate and form clusters. The pure PAN membrane has an ionic conductivity of 0.87 mS/cm, while the membrane with 15 wt% LLTO has an ionic conductivity of 1.95 mS/cm. This is attributed to increase in surface area which can trap more liquid electrolyte.

### **1.3 Electrospinning**

Electrospinning is a unique process that uses electrostatic forces to create micron and submicron fibers from a variety of polymer solutions. Though the principles of electrospinning have been known for centuries, its not until the 1990's that it became widely used among researchers. Since then, researchers have used utilized their unique properties for their used in filtration, biomedical devices, energy devices, etc.

Electrospinning consists of three main parts: a syringe filled with polymer solution, a grounded collector, and a voltage source providing electricity to the needle attached to the syringe. Using an external force, such as a syringe pump, solution of gradually forced out of the syringe into the needle. A voltage source is attached to the needle, creating a positive charge on the polymer solution. The application of the electric field creates an electrical field gradient

between the polymer solution and the grounded collector. The interaction between the applied electric field and the polymer solution creates a pendant-like droplet called a Taylor cone. The Taylor cone concept was first discussed by Geoffrey Ingram Taylor in 1969 following his work studying electrostatic interaction on a polymer droplet from conducting tubes.<sup>91</sup> He found the droplet forms into a conical shape and jets are ejected from the cone once the critical electrical potential is reached to overcome the surface tension forces on the polymer surface. He determined a semi-vertical angle of 49.3 degrees is required in order for the polymer solution to produce jets.<sup>92</sup> Once the Taylor cone forms and then jet is ejected, the polymer jet begins to elongate as the electrical force increases. The jet is distorted and undergoes stretching and whipping because it is subjected to a variety of forces during traveling, including electrostatic repulsion between charged ions and Coulombic force by the external electric field. As the polymer jet travels, the solvent rapidly evaporates ( $\sim 200$  nl/s)<sup>93</sup>, resulting in solidified fibers collecting on the grounded current collector. The resultant fibers are nanoscale fibers with large surface area to mass ratio, where typical specific surface area is  $10$  m<sup>2</sup>/g for fiber diameters around  $500$  nm and  $1000$  m<sup>2</sup>/g for diameters around  $50$  nm<sup>94</sup>.

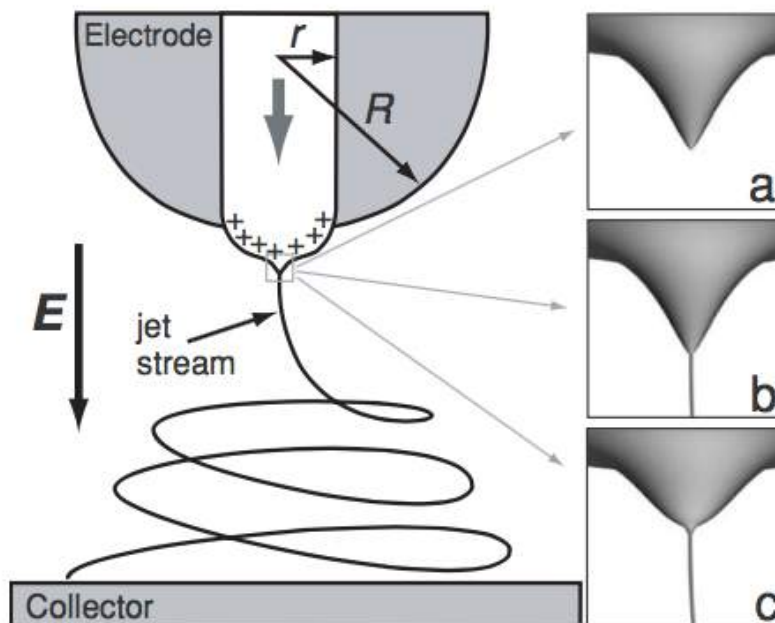


**Figure 1-17** Schematic of electrospinning set up (a) Formation of Taylor cone in an applied electric field. (b) Taylor cone ejects fluid jet. (c) Surface tension causes cone shape to relax.<sup>95</sup>

The electrospinning technique can be done with a variety of materials such as natural and synthetic fibers, metal oxides and precursors and ceramic precursors.<sup>96</sup> The morphology of the resultant fibers varies including beads<sup>94</sup>, aligned<sup>97-99</sup>, hollow<sup>100-102</sup>, core-shell<sup>103-105</sup>, flat ribbon<sup>106</sup>, porous<sup>107-109</sup>, etc. A variety of factors affect the electrospinning process and hence the final fiber morphology. These factors include properties of the solution including the type of polymer, polymer molecular weight, conductivity, surface tension and polymer viscosity, volatility of solvent. Operation variables include applied electric field strength; solution feed rate; spinneret diameter; distance between the spinneret and the collecting substrate. The final morphology can also be affected by environmental factors such as air temperature, humidity and air speed. All these factors must be well balanced to create the desired fiber morphology and diameter.<sup>95,110</sup>

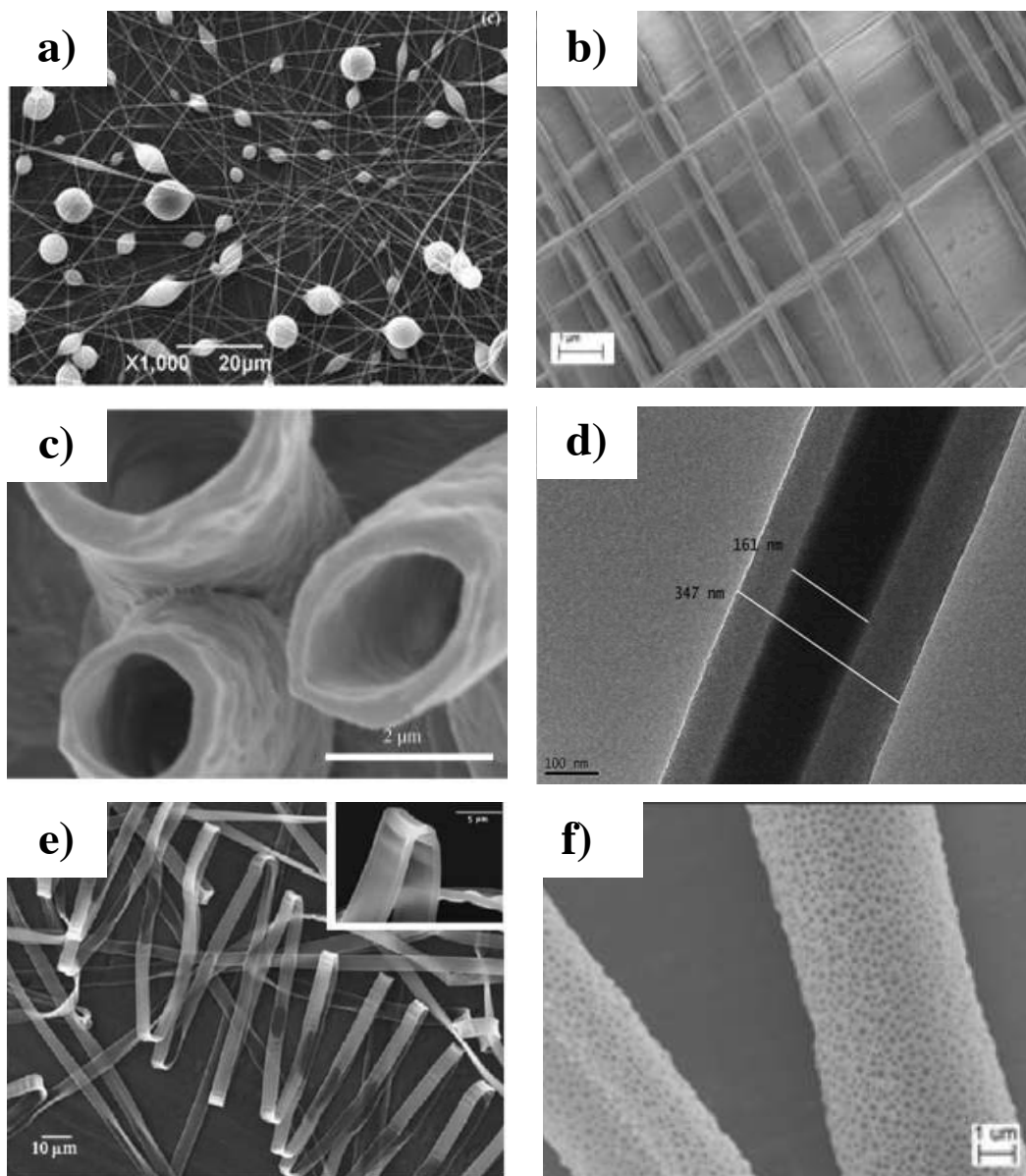


**Figure 1-18** Different fiber morphologies achieved by various researchers using the electrospinning technique: a) beaded<sup>112</sup> b) aligned<sup>113</sup> c) hollow<sup>114</sup> d) core-sheath<sup>115</sup> e) flat ribbon<sup>107</sup> f) porous<sup>116</sup>

## 1.4 Ceramic Precursors

There are a variety of liquid precursors of Si-O precursor including tetraethyl orthosilicate (TEOS), perhydropolysilazane (PHPS), polysiloxanes, polysilazanes, etc. TEOS is one of the most widely known silica precursors. TEOS can produce amorphous silica via the sol-gel process using either an acid or base catalyst.<sup>111</sup> The sol-gel precursors will hydrolyze to make silanols and alcohols. The silanol groups can then either react with precursor molecules or themselves to form siloxane groups via condensation. Multiple condensation and hydrolysis reactions will eventually result in a Si-O-Si network. However TEOS needs to be heated to high temperatures to fully convert, which can be damaging to most polymer. Most polymer would melt or degrade well before the required 600°C required for TEOS curing. Therefore, it's necessary to also consider precursors that can cure at room temperature.

Polysilazanes (PSZ) is a preceramic polymer with alternating silicon and nitrogen along the backbone. PSZ can be divided into two classes, organic PSZ, which contains hydrocarbon, and inorganic PSZ, which lack carbon. C.R. Krüger first described polysilazanes in 1964 by reacting chlorosilanes and ammonia gas without the presence of water or moisture.<sup>117</sup> However PSZs were not widely available due high cost of the material for decades. The high cost was a result of solvent stripping process that was required to remove the ammonium salt byproduct of the process.<sup>118</sup> However in 1999, Kion Corporation developed a liquid ammonia process, which made the production of polysilazanes more widely available and at a cheaper cost. Polysilazane precursors are a colorless or pale yellow liquid that releases an ammonium smell when exposed to air. They are widely used widely for conversion and protection functions such as corrosion inhibition, anti-graffiti, and high temperature performances.

PHPS is an inorganic polymer consisting of a Si-N backbone that has gained much attention for the use in making silica thin films.<sup>119</sup> PHPS has been converted to silica using a variety of methods including exposure to a vaporized ammonia atmosphere<sup>120</sup>, ultraviolet light radiation<sup>121</sup>, heating at high temperature<sup>122</sup>, curing at ambient temperature in a high humidity environment<sup>123</sup> among others. The latter of the previously mentioned methods seems promising, as it will not cause any damage to the polymers used. The curing of PHPS can be seen below in Figure 1-19.

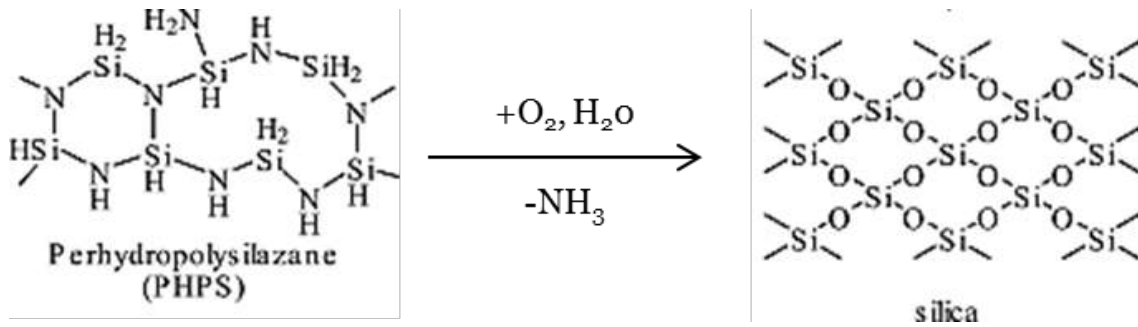


**Figure 1-19** Chemical structure of PHPS and its conversion to silica at ambient temperature

Organopolysilazane (OPSZ) contains both functional organic groups and polar reactive silazane groups resulting in a unique ceramic precursor.<sup>124</sup> Similar to PHPS, the Si-N groups can be converted to chemically and thermally inert Si-O bonds in the presence of heat and water. However the presence of hydrocarbon groups leads the final product to be a silicon carbonitride or a silicon oxycarbide ceramic.<sup>125</sup> They have been used for a variety of uses including superhydrophobic coatings<sup>124</sup>, polymer network dielectrics<sup>126</sup>, selective permeation membranes<sup>127</sup> etc.

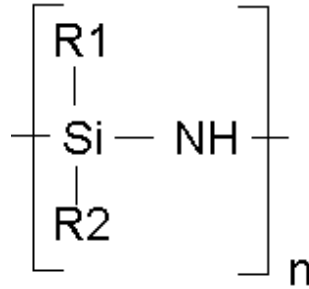


**Figure 1-20** The chemical formula of organopolysilazane where R<sub>1</sub> and R<sub>2</sub> can be organic pendant groups or hydrogen

Currently most application utilizing OPSZ materials use the pyrolysis method to cure the precursor into a ceramic. The conversion into a ceramic is done by the thermal decomposition of the organic groups usually above 600°C.<sup>128</sup> The temperature at which the pyrolysis is carried out is impact as it impacts the final structure of the ceramic. Heating to 1000°C results in amorphous ternary or quaternary Si-based ceramics.<sup>129</sup> Continued heating up to 1200 to 1600°C can induce the crystallization of amorphous phase ceramic to be in a crystalline phase. As the material heats up the characteristics of the material also; the density changes from 1 g/cm<sup>3</sup> for the liquid precursor to 2.3 g/cm<sup>3</sup> for the cured ceramic.

## References

1. Winter, M. & Brodd, R. J. What are batteries, fuel cells, and supercapacitors? *Chem. Rev.* **104**, 4245 (2004).
2. Whittingham, M. S., Savinell, R. F. & Zawodzinski, T. Introduction: Batteries and fuel cells. *Chem. Rev.* **104**, 4243–4244 (2004).
3. Reddy, T. *Linden's Handbook of Batteries (4th Edition)*. (McGraw-Hill Professional Publishing, 2010).
4. Besenhard, J. O. & Daniel, C. *Handbook of Battery Materials*. (Wiley-VCH, 2011).
5. Dunn, B., Kamath, H. & Tarascon, J.-M. Electrical energy storage for the grid: a battery of choices. *Science* **334**, 928 (2011).
6. Vervaet, A. A. K. & Baert, D. H. J. The lead acid battery: semiconducting properties and Peukert's law. *Electrochimica Acta* **47**, 3297–3302 (2002).
7. Pavlov, D. *Lead-acid batteries*. (Elsevier, 2011).
8. Galushkin, N., Yazvinskaya, N., Galushkin, D. & Galushkina, I. Probability Investigation of Thermal Runaway in Nickel-Cadmium Batteries with Sintered, Pasted and Pressed Electrodes. *Int. J. Electrochem. Sci.* **10**, 6645–6650 (2015).
9. Putois, F. Market for nickel-cadmium batteries. *J. Power Sources* **57**, 67–70 (1995).
10. David, J. in *Industrial Chemistry Library* (ed. G. Pistoia, J.-P. W. and S. P. W.) **10**, 147–176 (Elsevier, 2001).
11. Ruetschi, P., Meli, F. & Desilvestro, J. Nickel-metal hydride batteries. The preferred batteries of the future? *J. Power Sources* **57**, 85–91 (1995).
12. Nishi, Y. in *Lithium-Ion Batteries* (ed. Pistoia, G.) 21–39 (Elsevier, 2014).
13. Glaize, C. & Genies, S. *Lithium Batteries and other Electrochemical Storage Systems*. (John Wiley & Sons, 2013).
14. Goodenough, J. B. & Kim, Y. Challenges for rechargeable batteries. *J. Power Sources* **196**, 6688–6694 (2011).
15. Wakihara, M. & Yamamoto, O. *Lithium Ion Batteries: Fundamentals and Performance*. (John Wiley & Sons, 2008).
16. *Lithium Batteries: Science and Technology*. (Springer US, 2003).
17. Ibrahim, H. & Ilic, A. in *Energy Storage - Technologies and Applications* (ed. Zobia, A.) (InTech, 2013).

18. Tarascon, J.-M. & Armand, M. Issues and challenges facing rechargeable lithium batteries. *Nature* **414**, 359 (2001).
19. Patil, A., Patil, V., Wook Shin, D. & Choi, J.-W. Issue and challenges facing rechargeable thin film lithium batteries. *Mater. Res. Bull.* **43**, 1913–1942 (2008).
20. Gwon, H., Hong, J., Kim, H. & Seo, D.-H. Recent progress on flexible lithium rechargeable batteries. **7**, 538–551 (2014).
21. Song, M.-K., Park, S., Alamgir, F. M. & Cho, J. Nanostructured electrodes for lithium-ion and lithium-air batteries: the latest developments, challenges, and perspectives. *Mater. Sci. Eng. R* **72**, 203 (2011).
22. Nishi, Y. Lithium ion secondary batteries; past 10 years and the future. *J. Power Sources* **100**, 101–106 (2001).
23. Fergus, J. W. Recent developments in cathode materials for lithium ion batteries. *J. Power Sources* **195**, 939–954 (2010).
24. Fu, J., Bai, Y., Liu, C. & Yu, H. Physical characteristic study of LiCoO<sub>2</sub> prepared by molten salt synthesis method in 550–800°C. *Mater. Chem. Phys.* **115**, 105–109 (2009).
25. Julien, C. M., Mauger, A., Zaghbi, K. & Groult, H. Comparative Issues of Cathode Materials for Li-Ion Batteries. *Inorg. Basel* **2**, 132–154 (2014).
26. Lewandowski, A. & Świdarska-Mocek, A. Ionic liquids as electrolytes for Li-ion batteries—An overview of electrochemical studies. *J. Power Sources* **194**, 601–609 (2009).
27. Xu, K. Nonaqueous Liquid Electrolytes for Lithium-Based Rechargeable Batteries. *Chem. Rev.* **104**, 4303–4418 (2004).
28. Yang, M. & Hou, J. Membranes in Lithium Ion Batteries. *Membranes* **2**, 367–383 (2012).
29. Arora, P. & Zhang, Z. (John). Battery Separators. *Chem. Rev.* **104**, 4419–4462 (2004).
30. Djian, D., Alloin, F., Martinet, S. & Lignier, H. Lithium-ion batteries with high charge rate capacity: Influence of the porous separator. *J. Power Sources* **172**, 416–421 (2007).
31. Song, J. Y., Wang, Y. Y. & Wan, C. C. Review of gel-type polymer electrolytes for lithium-ion batteries. *J. Power Sources* **77**, 183–197 (1999).
32. Johnson, M. B. & Wilkes, G. L. Microporous membranes of polyoxymethylene from a melt-extrusion process: (I) effects of resin variables and extrusion conditions. *J. Appl. Polym. Sci.* **81**, 2944–2963 (2001).

33. Johnson, M. B. & Wilkes, G. L. Microporous membranes of isotactic poly(4-methyl-1-pentene) from a melt-extrusion process. I. Effects of resin variables and extrusion conditions. *J. Appl. Polym. Sci.* **83**, 2095–2113 (2002).
34. Venugopal, G., Moore, J., Howard, J. & Pendalwar, S. Characterization of microporous separators for lithium-ion batteries. *J. Power Sources* **77**, 34–41 (1999).
35. Sarada, T., Sawyer, L. C. & Ostler, M. I. Three dimensional structure of celgard® microporous membranes. *J. Membr. Sci.* **15**, 97–113 (1983).
36. Johnson, M. B. & Wilkes, G. L. Microporous membranes of polyoxymethylene from a melt-extrusion process: (II) effects of thermal annealing and stretching on porosity. *J. Appl. Polym. Sci.* **84**, 1762–1780 (2002).
37. Green, D. L., McAmish, L. & McCormick, A. V. Three-dimensional pore connectivity in biaxially stretched microporous composite membranes. *J. Membr. Sci.* **279**, 100–110 (2006).
38. Yu, W.-C. & Geiger, M. W. Shutdown, bilayer battery separator. (1996).
39. Hay, I., Bierenbaum, H., Daley, L. & Zimmerman, D. Process for preparing a thermoplastic microporous film involving a cold stretching step and multiple hot stretching steps. (1974).
40. Kurauchi, H., Akazawa, T. & Kawabata, A. Porous multi-layer film. (1997).
41. Zhang, S. S. A review on the separators of liquid electrolyte Li-ion batteries. *J. Power Sources* **164**, 351–364 (2007).
42. Bierenbaum, H. S., Isaacson, R. B., Druin, M. L. & Plovan, S. G. Microporous Polymeric Films. *Prod. RD* **13**, 2–9 (1974).
43. Kesting, R. E. *Synthetic Polymeric Membranes: A Structural Perspective*. (Wiley-Interscience, 1985).
44. Jacoby, P. & Bauer, C. W. Oriented porous polypropylene films. (1990).
45. Zhang, X. *et al.* Biaxially oriented porous membranes, composites, and methods of manufacture and use. (2011).
46. Han, J. Y., Oh, H.-H., Jun Choi, K. & Min, B. R. Characterization of poly(vinylidene fluoride) flat sheet membranes prepared in various ratios of water/ethanol for separator of lithium-ion batteries: Morphology and other properties. *J. Appl. Polym. Sci.* **122**, 2653–2665 (2011).
47. Zhang, S. S., Ervin, M. H., Xu, K. & Jow, T. R. Microporous poly(acrylonitrile-methyl methacrylate) membrane as a separator of rechargeable lithium battery. *Electrochimica Acta* **49**, 3339–3345 (2004).

48. Lee, M.-H., Kim, H. J., Kim, E., Rhee, S. B. & Moon, M. J. Effect of phase separation on ionic conductivity of poly(methyl methacrylate)-based solid polymer electrolyte. *Solid State Ion.* **85**, 91–98 (1996).
49. Jung, B., Yoon, J. K., Kim, B. & Rhee, H.-W. Effect of crystallization and annealing on polyacrylonitrile membranes for ultrafiltration. *J. Membr. Sci.* **246**, 67–76 (2005).
50. Shi, Q., Yu, M., Zhou, X., Yan, Y. & Wan, C. Structure and performance of porous polymer electrolytes based on P(VDF-HFP) for lithium ion batteries. *J. Power Sources* **103**, 286–292 (2002).
51. Hwang, Y. J., Nahm, K. S., Kumar, T. P. & Stephan, A. M. Poly(vinylidene fluoride-hexafluoropropylene)-based membranes for lithium batteries. *J. Membr. Sci.* **310**, 349–355 (2008).
52. Subramania, A., Sundaram, N. T. K. & Kumar, G. V. Structural and electrochemical properties of micro-porous polymer blend electrolytes based on PVdF-co-HFP-PAN for Li-ion battery applications. *J. Power Sources* **153**, 177–182 (2006).
53. Ma, T. *et al.* Preparation of PVDF based blend microporous membranes for lithium ion batteries by thermally induced phase separation: I. Effect of PMMA on the membrane formation process and the properties. *J. Membr. Sci.* **444**, 213–222 (2013).
54. Jung, B., Yoon, J. K., Kim, B. & Rhee, H.-W. Effect of molecular weight of polymeric additives on formation, permeation properties and hypochlorite treatment of asymmetric polyacrylonitrile membranes. *J. Membr. Sci.* **243**, 45–57 (2004).
55. Pu, W. *et al.* Preparation of P(AN–MMA) microporous membrane for Li-ion batteries by phase inversion. *J. Membr. Sci.* **280**, 6–9 (2006).
56. Ellison, C. J., Phatak, A., Giles, D. W. & Macosko, C. W. Melt blown nanofibers: Fiber diameter distributions and onset of fiber breakup. *Polymer* **48**, 3306–3316 (2007).
57. Yi, W., Xiaoli, D., Yunzhen, Y. & Yun, L. Study on wet-laid nonwoven separator of lithium-ion battery. *Text. Res. J.* **82**, 1659 (2012).
58. Boudriot, U., Dersch, R., Greiner, A. & Wendorff, J. H. Electrospinning approaches toward scaffold engineering - A brief overview. *Artif. ORGANS* **30**, 785–792 (2006).
59. Hao, J. *et al.* A novel polyethylene terephthalate nonwoven separator based on electrospinning technique for lithium ion battery. *J. Membr. Sci.* **428**, 11–16 (2013).

60. Raghavan, P., Manuel, J., Zhao, X. & Kim, D.-S. Preparation and electrochemical characterization of gel polymer electrolyte based on electrospun polyacrylonitrile nonwoven membranes for lithium batteries. *J. Power Sources* **196**, 6742–6749 (2011).
61. Choi, S. W., Kim, J. R., Jo, S. M. & Lee, W. S. Electrochemical and spectroscopic properties of electrospun PAN-based fibrous polymer electrolytes. *J. Electrochem. Soc.* **152**, A989–A995 (2005).
62. Cho, T. H., Sakai, T., Tanase, S. & Kimura, K. Electrochemical Performances of Polyacrylonitrile Nanofiber-Based Nonwoven Separator for Lithium-Ion Battery. *Electrochem. Solid-State Lett.* **10**, A159 (2007).
63. Carol, P., Ramakrishnan, P., John, B. & Cheruvally, G. Preparation and characterization of electrospun poly(acrylonitrile) fibrous membrane based gel polymer electrolytes for lithium-ion batteries. *J. Power Sources* **196**, 10156–10162 (2011).
64. Cho, T.-H. *et al.* Battery performances and thermal stability of polyacrylonitrile nano-fiber-based nonwoven separators for Li-ion battery. *J. Power Sources* **181**, 155–160 (2008).
65. Gopalan, A. I. *et al.* Development of electrospun PVdF–PAN membrane-based polymer electrolytes for lithium batteries. *J. Membr. Sci.* **325**, 683–690 (2008).
66. Miao, Y.-E., Zhu, G.-N., Hou, H. & Xia, Y.-Y. Electrospun polyimide nanofiber-based nonwoven separators for lithium-ion batteries. *J. Power Sources* **226**, 82–86 (2013).
67. Jiang, W., Liu, Z. H., Kong, Q. S. & Yao, J. H. A high temperature operating nanofibrous polyimide separator in Li-ion battery. *SOLID STATE Ion.* **232**, 44–48 (2013).
68. Costa, C. M., Nunes-Pereira, J., Sencadas, V., Silva, M. M. & Lanceros-Méndez, S. Effect of fiber orientation in gelled poly(vinylidene fluoride) electrospun membranes for Li-ion battery applications. *J. Mater. Sci.* **48**, 6833–6840 (2013).
69. Choi, S. w., Jo, S. m., Lee, W. s. & Kim, Y.-R. An Electrospun Poly(vinylidene fluoride) Nanofibrous Membrane and Its Battery Applications. *Adv. Mater.* **15**, 2027–2032 (2003).
70. Gao, K., Hu, X., Dai, C. & Yi, T. Crystal structures of electrospun PVDF membranes and its separator application for rechargeable lithium metal cells. *Mater. Sci. Eng. B* **131**, 100–105 (2006).
71. Raghavan, P. *et al.* Electrochemical studies on polymer electrolytes based on poly(vinylidene fluoride-co-hexafluoropropylene) membranes prepared by electrospinning and phase inversion—A comparative study. *Mater. Res. Bull.* **45**, 362–366 (2010).

72. Kader, M. A., Kwak, S. K., Kang, S. L., Ahn, J.-H. & Nah, C. Novel microporous poly(vinylidene fluoride)-graft-poly(tert-butyl acrylate) electrolytes for secondary lithium batteries. *Polym. Int.* **57**, 1199–1205 (2008).
73. Angulakshmi, N. & Stephan, A. M. Electrospun Trilayer Polymeric Membranes as Separator for Lithium-ion Batteries. *Electrochimica Acta* **127**, 167–172 (2014).
74. Jeong, H.-S., Noh, J. H., Hwang, C.-G., Kim, S. H. & Lee, S.-Y. Effect of Solvent–Nonsolvent Miscibility on Morphology and Electrochemical Performance of SiO<sub>2</sub>/PVdF-HFP-Based Composite Separator Membranes for Safer Lithium-Ion Batteries. *Macromol. Chem. Phys.* **211**, 420–425 (2010).
75. Fu, D., Luan, B., Argue, S., Bureau, M. N. & Davidson, I. J. Nano SiO<sub>2</sub> particle formation and deposition on polypropylene separators for lithium-ion batteries. *J. Power Sources* **206**, 325–333 (2012).
76. Takemura, D. *et al.* A powder particle size effect on ceramic powder based separator for lithium rechargeable battery. *J. Power Sources* **146**, 779–783 (2005).
77. Choi, J.-A., Kim, S. H. & Kim, D.-W. Enhancement of thermal stability and cycling performance in lithium-ion cells through the use of ceramic-coated separators. *J. Power Sources* **195**, 6192–6196 (2010).
78. Kang, S. M., Ryou, M.-H., Choi, J. W. & Lee, H. Mussel- and Diatom-Inspired Silica Coating on Separators Yields Improved Power and Safety in Li-Ion Batteries. *Chem. Mater.* **24**, 3481–3485 (2012).
79. Zhu, X., Jiang, X., Ai, X., Yang, H. & Cao, Y. A Highly Thermostable Ceramic-Grafted Microporous Polyethylene Separator for Safer Lithium-Ion Batteries. *ACS Appl. Mater. Interfaces* **7**, 24119–24126 (2015).
80. Zhang, S. S., Xu, K. & Jow, T. R. An inorganic composite membrane as the separator of Li-ion batteries. *J. Power Sources* **140**, 361–364 (2005).
81. Zhang, S. S., Xu, K. & Jow, T. R. Alkaline composite film as a separator for rechargeable lithium batteries. *J. Solid State Electrochem.* **7**, 492–496 (2003).
82. Cho, T. H., Tanaka, M., Onishi, H. & Kondo, Y. Silica-composite nonwoven separators for lithium-ion battery: Development and characterization. *J. Electrochem. Soc.* **155**, A699–A703 (2008).

83. Cho, T.-H., Tanaka, M., Ohnishi, H. & Kondo, Y. Composite nonwoven separator for lithium-ion battery: Development and characterization. *J. Power Sources* **195**, 4272–4277 (2010).
84. Sethupathy, M., Sethuraman, V. & Manisankar, P. Preparation of PVDF/SiO<sub>2</sub> Composite Nanofiber Membrane Using Electrospinning for Polymer Electrolyte Analysis. *Soft Nanosci. Lett.* **03**, 37–43 (2013).
85. Zhang, J. *et al.* A Heat-Resistant Silica Nanoparticle Enhanced Polysulfonamide Nonwoven Separator for High-Performance Lithium Ion Battery. *J. Electrochem. Soc.* **160**, A769–A774 (2013).
86. Yanilmaz, M., Lu, Y., Dirican, M., Fu, K. & Zhang, X. Nanoparticle-on-nanofiber hybrid membrane separators for lithium-ion batteries via combining electrospraying and electrospinning techniques. *J. Membr. Sci.* **456**, 57–65 (2014).
87. Jung, H.-R., Ju, D.-H., Lee, W.-J. & Zhang, X. Electrospun hydrophilic fumed silica/polyacrylonitrile nanofiber-based composite electrolyte membranes. *Electrochimica Acta* **54**, 3630–3637 (2009).
88. Kim, J.-K. *et al.* Preparation and electrochemical characterization of electrospun, microporous membrane-based composite polymer electrolytes for lithium batteries. *J. Power Sources* **178**, 815–820 (2008).
89. Yanilmaz, M., Dirican, M. & Zhang, X. Evaluation of electrospun SiO<sub>2</sub>/nylon 6,6 nanofiber membranes as a thermally-stable separator for lithium-ion batteries. *Electrochimica Acta* **133**, 501–508 (2014).
90. Liang, Y. *et al.* Preparation and electrochemical characterization of ionic-conducting lithium lanthanum titanate oxide/polyacrylonitrile submicron composite fiber-based lithium-ion battery separators. *J. Power Sources* **196**, 436–441 (2011).
91. Ding, B. & Yu, J. *Electrospun Nanofibers for Energy and Environmental Applications*. (Springer Science & Business Media, 2014).
92. Wendorff, J. H., Agarwal, S. & Greiner, A. *Electrospinning: Materials, Processing, and Applications*. (John Wiley & Sons, 2012).
93. Kalra, V., Lee, J. H., Park, J. H., Marquez, M. & Joo, Y. L. Confined Assembly of Asymmetric Block-Copolymer Nanofibers via Multiaxial Jet Electrospinning. *Small* **5**, 2323–2332 (2009).

94. Fong, H., Chun, I. & Reneker, D. H. Beaded nanofibers formed during electrospinning. *Polymer* **40**, 4585–4592 (1999).
95. Burger, C., Hsiao, B. S. & Chu, B. Nanofibrous materials and their applications. *Annu. Rev. Mater. Res.* **36**, 333–368 (2006).
96. Li, D., McCann, J. T., Xia, Y. & Marquez, M. Electrospinning: A Simple and Versatile Technique for Producing Ceramic Nanofibers and Nanotubes. *J. Am. Ceram. Soc.* **89**, 1861 (2006).
97. Li, D., Wang, Y. L. & Xia, Y. N. Electrospinning of polymeric and ceramic nanofibers as uniaxially aligned arrays. *NANO Lett.* **3**, 1167–1171 (2003).
98. Subramanian, A., Krishnan, U. M. & Sethuraman, S. Fabrication of uniaxially aligned 3D electrospun scaffolds for neural regeneration. *Biomed. Mater. Bristol Engl.* **6**, 025004 (2011).
99. Jalili, R., Morshed, M., Abdolkarim, S. & Ravandi, H. Fundamental parameters affecting electrospinning of PAN nanofibers as uniaxially aligned fibers. *J. Appl. Polym. Sci.* **101**, 4350–4357 (2006).
100. Li, D. & Xia, Y. Direct Fabrication of Composite and Ceramic Hollow Nanofibers by Electrospinning. *Nano Lett.* **4**, 933–938 (2004).
101. Cheng, L., Ma, S. Y., Wang, T. T. & Li, X. B. Synthesis and characterization of SnO<sub>2</sub> hollow nanofibers by electrospinning for ethanol sensing properties. *Mater. Lett.* **131**, 23–26 (2014).
102. Li, W. Q., Ma, S. Y., Li, Y. F. & Li, X. B. Preparation of Pr-doped SnO<sub>2</sub> hollow nanofibers by electrospinning method and their gas sensing properties. *J. Alloys Compd.* **605**, 80–88 (2014).
103. Yao, P. J., Wang, J., Qiao, Q. & Du, H. Y. Direct fabrication of La<sub>0.7</sub>Sr<sub>0.3</sub>FeO<sub>3</sub> nanofibers with tunable hollow structures by electrospinning and their gas sensing properties. *J. Mater. Sci.* **50**, 1338–1349 (2015).
104. Yuan, J. & Müller, A. H. E. One-dimensional organic–inorganic hybrid nanomaterials. *Polymer* **51**, 4015–4036 (2010).
105. Wu, X.-F., Rahman, A., Zhou, Z. & Pelot, D. D. Electrospinning core-shell nanofibers for interfacial toughening and self-healing of carbon-fiber/epoxy composites. *J. Appl. Polym. Sci.* **129**, 1383 (2013).

106. Li, X., Hao, X., Yu, H. & Na, H. Fabrication of Polyacrylonitrile/polypyrrole (PAN/Ppy) composite nanofibres and nanospheres with core-shell structures by electrospinning. *Mater. Lett.* **62**, 1155–1158 (2008).
107. Reneker, D. H. & Yarin, A. L. Electrospinning jets and polymer nanofibers. *Polymer* **49**, 2387–2425 (2008).
108. Li, D. & Xia, Y. N. Electrospinning of nanofibers: Reinventing the wheel? *Adv. Mater.* **16**, 1151–1170 (2004).
109. Bognitzki, M., Frese, T., Steinhart, M. & Greiner, A. Preparation of fibers with nanoscaled morphologies: Electrospinning of polymer blends. *Polym. Eng. Sci.* **41**, 982–989 (2001).
110. Yu, X., Xiang, H., Long, Y. & Zhao, N. Preparation of porous polyacrylonitrile fibers by electrospinning a ternary system of PAN/DMF/H<sub>2</sub>O. *Mater. Lett.* **64**, 2407–2409 (2010).
111. Sinkó, K. Influence of Chemical Conditions on the Nanoporous Structure of Silicate Aerogels. *Materials* **3**, 704–740 (2010).
112. Huang, Z.-M., Zhang, Y.-Z., Kotaki, M. & Ramakrishna, S. A review on polymer nanofibers by electrospinning and their applications in nanocomposites. *Compos. Sci. Technol.* **63**, 2223–2253 (2003).
113. Li, L., Jiang, Z., Li, M. & Li, R. Hierarchically structured PMMA fibers fabricated by electrospinning. *RSC Adv* **4**, 52973–52985 (2014).
114. Su, Z. Q., Li, J. F., Li, Q. & Ni, T. Y. Chain conformation, crystallization behavior, electrical and mechanical properties of electrospun polymer-carbon nanotube hybrid nanofibers with different orientations. *CARBON* **50**, 5605–5617 (2012).
115. Dror, Y., Salalha, W., Avrahami, R. & Zussman, E. One-step production of polymeric microtubes by co-electrospinning. *Small Weinh. Bergstr. Ger.* **3**, 1064 (2007).
116. Nguyen, T. T. T., Lee, J. G. & Park, J. S. Fabrication and characterization of coaxial electrospun polyethylene glycol/polyvinylidene fluoride (Core/Sheath) composite non-woven mats. *Macromol. Res.* **19**, 370–378 (2011).
117. Krüger, C. R. & Rochow, E. G. Polyorganosilazanes. *J. Polym. Sci. A* **2**, 3179–3189 (1964).
118. Alexander Lukacs III. Polysilazane Precursors to Advanced Ceramics. *Am. Ceram. Soc. Bull.* **86**, 9301–9306 (2007).

119. Kozuka, H., Nakajima, K. & Uchiyama, H. Superior Properties of Silica Thin Films Prepared from Perhydropolysilazane Solutions at Room Temperature in Comparison with Conventional Alkoxide-Derived Silica Gel Films. *ACS Appl. Mater. Interfaces* **5**, 8329–8336 (2013).
120. Fang, Q., Kim, D.-P., Li, X., Yoon, T.-H. & Li, Y. Facile fabrication of a rigid and chemically resistant micromixer system from photocurable inorganic polymer by static liquid photolithography (SLP). *Lab. Chip* **11**, 2779–2784 (2011).
121. Prager, L. *et al.* Conversion of Perhydropolysilazane into a SiO<sub>x</sub> Network Triggered by Vacuum Ultraviolet Irradiation: Access to Flexible, Transparent Barrier Coatings. *Chem. – Eur. J.* **13**, 8522–8529 (2007).
122. Kamiya, K., Oka, A., Nasu, H. & Hashimoto, T. Comparative Study of Structure of Silica Gels from Different Sources. *J. Sol-Gel Sci. Technol.* **19**, 495–499 (2000).
123. Bauer, F. *et al.* Preparation of moisture curable polysilazane coatings: Part I. Elucidation of low temperature curing kinetics by FT-IR spectroscopy. *Prog. Org. Coat.* **53**, 183–190 (2005).
124. Koo, S. H. *et al.* Robust multifunctional superhydrophobic organic–inorganic hybrid macroporous coatings and films. *Polymer* **55**, 2661–2666 (2014).
125. Kroke, E. *et al.* Silazane derived ceramics and related materials. *Mater. Sci. Eng. R Rep.* **26**, 97–199 (2000).
126. Lee, H. S. *et al.* Interpenetrating polymer network dielectrics for high-performance organic field-effect transistors. *J. Mater. Chem.* **21**, 6968–6974 (2011).
127. Miyajima, K., Eda, T., Nair, B. N. & Iwamoto, Y. Organic–inorganic layered membrane for selective hydrogen permeation together with dehydration. *J. Membr. Sci.* **421–422**, 124–130 (2012).
128. Liu, Q., Shi, W., Babonneau, F. & Interrante, L. V. Synthesis of Polycarbosilane/Siloxane Hybrid Polymers and Their Pyrolytic Conversion to Silicon Oxycarbide Ceramics. *Chem. Mater.* **9**, 2434–2441 (1997).
129. Kousaalya, A. B., Kumar, R. & Packirisamy, S. Characterization of free carbon in the as-thermolyzed Si-B-C-N ceramic from a polyorganoborosilazane precursor. *J. Adv. Ceram.* **2**, 325–332 (2013).

## CHAPTER 2 Objectives and Motivation

The separator is an essential component of a lithium ion battery, which lies in between the cathode and anode. Though it doesn't take part in the electrochemical reaction of the battery, it is necessary to prevent short-circuiting of battery and also provides a path for ionic conduction. As a result, the physical properties of separators can affect the cell capacity, cell resistance, rate performance, and long-term cycling capability of lithium-ion batteries. Current polyolefin separators have excellent mechanical strength and chemical stability. However, the hydrophobic nature of the polymers used to manufacture these membranes leads to poor wettability and thermal stability. Low affinity of polyolefin to liquid electrolyte also leads to high cell resistance that negatively affects the cycling performance and rate performance. In addition, the semi-crystalline polymer used leads to low porosity of the membranes (~40%), further impacting the ionic conductivity of the membranes.

Researchers have utilized the electrospinning technique in order to create non-woven membranes for the use as separators in non-woven membranes. The electrospinning technique produces micro to nanometers sized continuous fibers creating a highly porous interconnected network. Due to the high surface area, high porosity and small pore size of electrospun membranes, they have proven to be excellent separators in high performance lithium ion batteries. In addition, the performance of electrospun mats can be further improved by introducing ceramic components into the matrix. Incorporating ceramic fillers can improve the mechanical, thermal and electrochemical stability of the membranes.

Current methods of incorporating preformed ceramic fillers into the matrix include either dip coating the electrospun membrane into ceramic slurry or incorporating fillers directly into the polymer matrix. Both steps require extensive either pre or post-processing steps to distribute the

ceramic. Coated membranes however face the risk of the ceramic delaminating from the surface of the membrane, which then would negatively affect the electrochemical performance. Integrating the ceramic into polymer matrix requires sonication of to ensure even distribution of the ceramic. In addition, when ceramics are added at a high loading, there is the risk of aggregation of the particles which also leads to poor cycling performance.

The objective of this work is to create polymer/ceramic hybrid electrospun nanofiber membrane with high ceramic loading via a one-step process. In this research, a novel approach was used in order to create high performance membrane separators. Instead of using pre-prepared nanoparticles as previous researchers have done, we chose to use a sol-gel technique to create hybrid membranes. The hydrolysis and polycondensation of liquid precursors allows for composite with high ceramic loading.

### **(I) Polyacrylonitrile/Polymer Derived Ceramic Co-continuous Nanofiber Membranes via Room-Curable Organopolysilazane for Improved Lithium Ion Battery Performance**

Polymer/Ceramic hybrid materials were prepared using polyacrylonitrile as the polymer matrix and Kion Slow Cure organopolysilazane (OPSZ) as the ceramic precursor. The amount of precursor added was varied from 10 to 30 percent to characterize the effects of various loadings on the mechanical, thermal and electrochemical performance on the hybrid membranes. The results of this work are discussed in Chapter 4.

### **(II) Impact of Various Room-Curable Organopolysilazane on the Performance of Electrospun PAN/Polymer Derived Ceramic Composite Nanofiber Membranes for Lithium Ion Battery Separators**

Various organopolysilazane precursors were incorporated into PAN polymer at the same loading. The three precursors have a similar chemical backbone but differ on the ratios of the tetraethyl orthosilicate (TEOS) pendant chain attached to the polysilazane (PSZ) backbone. The aim of this work is to investigate the effect of precursor structure used on the mechanical,

thermal and electrochemical performance on the hybrid membranes. The results of this work are discussed in Chapter 5.

### **(III) Effect of Ceramic Morphology on the Properties of Bi-Component Polyacrylonitrile/Polymer-Derived Ceramic Nanofibers for the use as Separator Membranes in Lithium-ion Batteries**

Organopolysilazane along with three other siloxane precursors were incorporated into PAN polymer. The resultant fibers showed fibers with different polymer/ceramic morphology, with some fibers containing ceramic on the surface of the fiber, while others only had ceramic on the interior of the fiber. We aim to show that the presence of ceramic precursor on the surface has a great impact on the ionic conductivity and hence the cycle performance on lithium ion full cells. The results of this work are discussed in Chapter 6.

## Chapter 3 Experimental Procedure

### 3.1 Materials

Polyacrylonitrile ( $M_w = 200,000$ , Polysciences), N,N-Dimethylformamide (DMF), Durazane 1500 Slow Cure (EMD Performance Materials), Durazane 1500 Rapid Cure (EMD Performance Materials), Durazane 33 (EMD Performance Materials), Methylsilsesquioxane (MSQ, Nepes Corporation), Methylsiloxane (MSX, Nepes Corporation), Polysilsesquioxane (PSSQ, Dongjin SemiChem Ltd.), Celgard 2400 (MTI Corporation), Lithium Cobalt Oxide ( $\text{LiCoO}_2$ , MTI Corporation), Graphite (MTI Corporation), 1M  $\text{LiPF}_6\text{-EC/DMC/DEC}$  (MTI Corporation), 812 EmBed Resin (Electron Microscopy Sciences), Hardner (Electron Microscopy Sciences)

### 3.2 Material Preparation

The electrospinning solution was prepared by combining PAN with DMF to form a 8wt% solution. The solution either left in a  $95^\circ\text{C}$  oven for 8 hours or stirred for 8 hours on a  $60^\circ\text{C}$  hot plate to thoroughly dissolve the polymer. The solution was then allowed to cool to room temperature before adding the pre-ceramic precursor. Polymer to ceramic ratio and corresponding spinning conditions are listed in Table 1. After the ceramic is added, the solution is mixed on a vortex mixer in order to mix the components. The solution was then allowed to sit for 10 minutes to allow for bubbles formed in the solution to disappear. A 20-gauge needle was used for all solutions. All samples were spun onto aluminum foil folded over a copper plate. After the membrane has spun for the appropriate amount of time, the nanofiber membrane was peeled off the foil. If the membrane is not peeled off the foil initially, it will stick to the foil and it will be impossible to remove from the foil. The membrane is then placed back on the foil, covered and placed in a  $120^\circ\text{C}$  oven for 12 hours.

Precursor	Polymer:Added Ceramic Ratio	Feed rate (mL/hr)	Voltage (KV)	Distance (cm)	Duration (mins)
	100:0	1.2	17.5	16	25
Durazane Slow Cure	90:10	0.90	17.5	16	30
	80:20	0.90	17.5	16	30
	70:30	0.60	17.5	16	45
Durazane Rapid Cure	70:30	0.60	17.5	16	45
Durazane 33	70:30	0.72	17	16	45
MSQ	60:40	1.80	15	16	15
MSX	60:40	2.40	16	16	25
PSSQ	90:10	0.90	17.5	20	45

**Table 3-1** Spinning conditions of various polymer/ceramic hybrid membranes. Note: MSQ and MSX a solutions are only 12 percent ceramic precursor. While the others are 100 percent precursor.

### 3.3 Membrane Characterization

The presence of ceramic elements in the final fiber was determined using Fourier transform infrared spectroscopy (FTIR) under ambient conditions within the range of 700 – 4000  $\text{cm}^{-1}$  with a resolution of 4  $\text{cm}^{-1}$  for 512 scans.

The fiber morphology and diameter were examined using scanning electron microscopy (Teca Mira3 Field Emission SEM) with an accelerating voltage of 5KV. Samples were coated with gold/palladium for 30 seconds to prevent charging during the imaging process. The average fiber diameters were determined by choosing 100 randomly selected fibers using Image J.

The internal morphology of the fibers was investigated by transmission electron microscopy (FEI Tecnai G2 T12 Spirit TEM STEM). Small pieces of membranes (5mm x 10mm) were embedded in an epoxy resin. The resin was prepared by combining the resin and the hardner at a 7.5:1 ratio and then thoroughly mixing the two components. The membranes are placed in a flat embedding molds and covered with the epoxy resin. The molds were then placed in a 50°C oven overnight. An ultramicrotome was used to create 70-100 nm slices that were collected onto 300 mesh hexagonal copper grids.

Ceramic content was approximated using thermogravimetric analysis (TGA) under nitrogen from 25°C to 1000°C at a 10°C heating rate. Thermal stability was characterized using differential scanning calorimetry (DSC, TA Instrument Q200) under nitrogen from 40°C to 350°C at a 10°C heating rate.

Wide angle X-ray diffraction (XRD) patterns were recorded from 10° to 70° for all prepared electrospun membranes using Theta-Theta X-ray Diffractometer (Scintag) with Cu radiation ( $\lambda = 1.5405\text{\AA}$ ; 40 mA and 40 kV). Separator sized samples were scanned at a 0.4°/min using #1 slit in the divergent beam slit, a #3 slit in the scatter slit on the x-ray tube side, a #0.3 in the diffracted beam slit and a #0.5 in scatter slit on the x-ray detector side.

The separator/electrolyte interaction was estimated by measuring the dynamic change in contact angle between the electrolyte and the separator. A single drop of electrolyte was dropped on each separator sample and using a high-speed camera images were captured every 0.001 sec. Electrolyte uptake is calculated using the following relation:

$$Uptake (\%) = \frac{M_a - M_i}{M_i} \times 100 \quad (1)$$

where  $M_a$  and  $M_i$  are the masses of the wet and dry membrane respectively. After weighing the dry membrane, it was soaked in the electrolyte for 30 minutes in a glove box filled with argon. The membranes were then removed and placed in between two pieces of filter paper to remove excessive electrolyte.

The porosity ( $P$ ) of the fabricated membranes was calculated by using the measured data and the materials' densities with the equation below.<sup>[31]</sup>

$$P = 1 - \left( \frac{W}{\rho \cdot V} \right) \quad (2)$$

where  $W$  is the dried membrane weight,  $\rho$  the membrane density, and  $V$  the apparent volume of the membrane. The membrane thickness was measured by a digital thickness gauge. A capillary flow porometry (Porous Media Inc., NY) was used to characterize pore size distribution of the fabricated membranes from the dry and wet flow curves. Silwick 20 was used as the wetting liquid in all cases

### 3.4 Electrochemical Characterization

Electrochemical test are carried out in a 2302 coin cell. Cell impedance was measured by sandwiching the separator membrane between two lithium disks inside a cell. The cells were tested on a PARSTAT 4000 (Princeton Applied Research), with the impedance measurements at amplitude of 5 mV over a frequency range of 20000 kHz to 1 Hz.

Full cell consisted of a LiCoO<sub>2</sub> cathode (MTI Corporation) with an active material loading of 14.5 mg/cm<sup>2</sup>, a graphite anode (MTI Corporation) with an active material loading of 11.7 mg/cm<sup>2</sup>, and LiPF<sub>6</sub>-EC/DMC/DEC as the electrolyte. Full cells for C-rate testing had slightly lighter active material loadings with the cathode and anode having loadings of 9.3 mg/cm<sup>2</sup> and

9.0 mg/cm<sup>2</sup> respectively. Both the cathode and anode were dried overnight in an 80°C vacuum oven to remove excess moisture. Cells were assembled in a argon filled glove box with water content approximately 0.6 ppm and oxygen content < 0.01 ppm. Full cell arrangement is presented in Figure 3-1. Cycling was carried out at a voltage range between 2.5 – 4.2 V at a 0.2 C and 0.5C charge and discharge rate. Cells that were cycled at 0.5C were cycled for the first cycle at 0.2C. Discharge rate capabilities was tested by charging cells to 4.2 V at 0.1 C rate for the first and last cycle and 0.2 C rate for all other cycles. Cells were discharged at 0.1 C, 0.2 C, 0.5 C, 1 C, 2 C, 5 C and 0.1 C respectively.

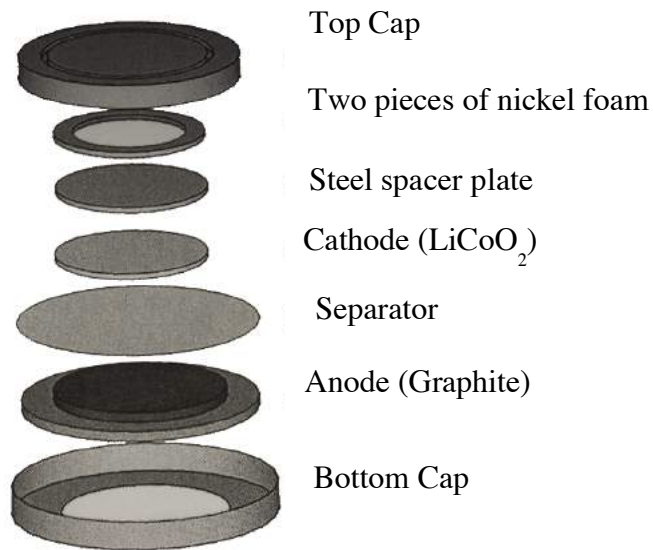


**Figure 3-1** Configuration of a typical full cell

## **Chapter 4 Polyacrylonitrile/Polymer Derived Ceramic Co-continuous Nanofiber Membranes via Room-Curable Organopolysiloxazane for Improved Lithium Ion Battery Performance**

### **Abstract**

Polyacrylonitrile (PAN) and ambient temperature curable organopolysiloxazane (OPSZ) were combined to successfully fabricate PAN/polymer derived ceramic (PDC) hybrid nanofiber separator using a single step electrospinning process. The amount of precursor added was varied from 10 to 30 percent to characterize the effects of various loadings on the mechanical, thermal and electrochemical performance on the hybrid membranes. TEM images reveal the ceramic phase formed a continuous interconnected network within the nanofiber at high concentrations. The well-formed 3D porous network created by the electrospinning process along with the inclusion of PDC ceramic increased the ionic conductivity of the separators; with the 30 wt% PDC sample having an ionic conductivity of 1.05 mS/cm compared to 0.29 mS/cm of pristine PAN separator. Due to the improved ionic conductivity and electrolyte uptake compared to pristine PAN, the electrochemical performance of the PAN/PDC separators also improved. All separators with additional PDC content showed increased initial capacity and capacity retention at a 0.2C charging and discharging rate; with the 90:10 wt%, 80:20 wt%, and 70:30 wt% of PAN:PDC showing 93%, 90% and 89% capacity retention over 100 cycles, respectively. In rate capability testing, PAN/PDC fibers demonstrated increased capacity retention even at increased charge rates.

### **4.1 Introduction**

Lithium ion batteries are used worldwide in a variety of electronic devices due to their high energy density, high efficiency, and long life cycle.<sup>[1]</sup> A separator plays a key role within the battery, acting as a physical barrier between the cathode and the anode, while aiding in ionic

transport. An ideal separator should allow for the rapid transport of ionic charge carriers while maintaining good thermal and mechanical stability as well as being chemically inert.<sup>[2]</sup> Current commercially available polyolefin separators fulfill some of the previously mentioned criteria but they also possess many disadvantages. Due to the intrinsic hydrophobic nature of polypropylene and polyethylene polymers used to manufacture the separators, the separators have low wettability and electrolyte uptake.<sup>[3]</sup> In addition to low wettability, polyolefin separators have low porosity approximately 40-50 percent, limiting the ion transport pathway.<sup>[1]</sup> These combined factors of poor wettability and low porosity lead to poor ionic transport over the lifetime of the batteries containing polyolefin separators.

Interest in non-woven separators has risen over the last decade to overcome some of the shortcomings of the polyolefins.<sup>[4-7]</sup> Using the electrospinning method, nonwoven separators have been fabricated from a variety of polymers including polyethylene terephthalate (PET),<sup>[8]</sup> polyacrylonitrile (PAN),<sup>[9-10]</sup> polyvinylidene fluoride (PVDF),<sup>[11-12]</sup> meta-aramid<sup>[13]</sup> and polyimide (PI)<sup>[14]</sup>. The porous 3-D structure of the electrospun fiber network resulted in a dramatic increase in porosity of separator membranes from 40-50 percent to 60-80 percent. This increase in porosity is correlated with an increase in ionic conductivity due to a higher effective diffusivity of the electrospun membranes. In addition, using more hydrophilic polymers instead of hydrophobic olefins allows for greater uptake of the electrolyte solution and better electrolyte retention in the batteries. Due to the increased porosity and increased wettability, electrospun nonwoven separators showed increased initial recharge capacity and capacity retention compared to the commercial polyolefin separator, Celgard.<sup>[15-16]</sup>

To further improve the performance of separators, researchers are also including ceramic components, such as SiO<sub>2</sub> and Al<sub>2</sub>O<sub>3</sub> to non-woven separators.<sup>[17-20]</sup> The inclusion of ceramics

resulted in composite separators with good ionic conductivity, high thermal stability and improved cycling performance.<sup>[21]</sup> The inclusion of ceramics into nonwovens is usually done via three methods: incorporating the ceramic directly into the polymer,<sup>[10]</sup> coating the non-woven in a ceramic<sup>[22]</sup> or a multi-layer rolling process.<sup>[23]</sup> Jung et al. incorporated fumed silica into PAN fibers to form separators with excellent cycling performance but could only improve electrochemical performance up to 12 wt%. Due to issues with dispersion of the silica within the PAN matrix, there was a limit to the enhancements from the silica particles. The coating and rolling methods also enhanced the battery performance. However, using either the rolling or coating methods often result in either delamination of the ceramic from the polymer or a phase separation which negates any benefits of adding a ceramic component.

In this work, a polymer/ceramic non-woven separator is created in a one-stop electrospinning process similar to Jung *et al.* Combining ceramics such as SiO<sub>2</sub> and nanoclay into polymer solutions usually require extensive ultra-sonication to achieve good dispersion of the inorganic ceramic within the fiber due to their tendency to aggregate. However, organopolysilazane is 100% miscible with PAN thus allowing uniform distribution of PDC along the fiber axis without the need for an additional preparation process. By combining PAN with a ceramic precursor, we were able to produce polymer/ceramic hybrid nanofiber separators at room temperature with high ceramic loading with no need for ultra-sonication nor any further post treatment processes. In addition, incorporating the ceramic directly into the nanofiber eliminates any issues of phase separation or delamination of the two components, a major drawback of the previous works using multilayer hybrid ceramics. In this work, we varied the amount of precursor to demonstrate the effect of ceramic content on cycling performance compared to a pure PAN non-woven separator. We also present how an increase in ceramic

content lead to an increase in ionic conductivity, initial capacity and overall capacity retention over the lifetime of the battery.

## **4.2 Experimental Section**

The PAN/ceramic non-woven separator was prepared using the electrospinning method. The electrospinning solution was prepared by combining Polyacrylonitrile (PAN,  $M_w = 200,000$ , Polysciences) with N,N-Dimethylformamide (DMF) to form a 8wt% solution. The solution was placed in a 95°C oven for 12 hours to thoroughly dissolve the polymer. The PAN/DMF was then left to cool at room temperature for 1 hour. The ceramic precursor, organopolysilazane (OPSZ, EMD Performance Materials), was added to obtain the desired weight percentage (10, 20 and 30wt%) in relation to PAN. The mixture was stirred on a vortex mixer for two minutes to ensure thorough mixing of the components. The solution was let to sit for 10 minutes to allowed any bubbles within the solution is disappear before spinning the solution.

The PAN/OPSZ solution was electrospun at a flow rate of 0.9 mL/hr for the 10 wt% and 20 wt% solution and 0.6 mL/hr for the 30 wt% solution using a 20-gauge needle. A 17.5 KV voltage and 15 cm distance between the needle and the collector plate was used for all samples. The collected samples were then annealed at 120°C for 12 hours to ensure the removal of all residual solvent.

### **4.2.1 Material Characterization**

The presence of ceramic elements in the final fiber was determined using Fourier transform infrared spectroscopy (FTIR) under ambient conditions within the range of 700 – 4000  $\text{cm}^{-1}$  with a resolution of 4  $\text{cm}^{-1}$  for 512 scans. The fiber morphology and diameter were examined using

scanning electron microscopy (Tescan Mira3 Field Emission SEM) with an accelerating voltage of 5KV. The average fiber diameters were determined by choosing 100 randomly selected fibers using Image J. The morphology of the cross section of the fibers was investigated by transmission electron microscopy (FEI Tecnai G2 T12 Spirit TEM STEM). Ceramic content was approximated using thermogravimetric analysis (TGA) under nitrogen from 25°C to 1000°C at a 10°C heating rate. Thermal stability was characterized using differential scanning calorimetry (DSC, TA Instrument Q200) under nitrogen from 40°C to 350°C at a 10°C heating rate. Wide angle X-ray diffraction (XRD) patterns were recorded from 10° to 70° for all prepared electrospun membranes using Theta-Theta X-ray Diffractometer (Scintag) with Cu radiation ( $\lambda = 1.5405\text{\AA}$ ; 40 mA and 40 kV). The separator/electrolyte interaction was estimated by measuring the dynamic change in contact angle between the electrolyte and the separator using a high speed camera capturing images every 0.001 sec. Electrolyte uptake is calculated using the following relation:

$$Uptake (\%) = \frac{M_a - M_i}{M_i} \times 100 \quad (1)$$

where  $M_a$  and  $M_i$  are the masses of the wet and dry membrane respectively. The porosity (P) of the fabricated membranes was calculated by using the measured data and the density of material with the equation below.<sup>[31]</sup>

$$P = 1 - \left( \frac{W}{\rho \cdot V} \right) \quad (2)$$

where  $W$  is the dried membrane weight,  $\rho$  the membrane density, and  $V$  the apparent volume of the membrane. The membrane thickness was measured by a digital thickness gauge. A capillary

flow porometry (Porous Media Inc., NY) was used to characterize pore size distribution of the fabricated membranes from the dry and wet flow curves.

#### **4.2.2 Electrochemical Characterization**

Electrochemical test are carried out in a 2302 coin cell. Cell impedance was measured by sandwiching the separator membrane between two lithium disks inside a cell. The cells were tested on a PARSTAT 4000 (Princeton Applied Research), with the impedance measurements at an amplitude of 5 mV over a frequency range of 20000 kHz to 1 Hz.

Full cell consisted of a LiCoO<sub>2</sub> cathode (MTI Corporation), a graphite anode (MTI Corporation), and LiPF<sub>6</sub>-EC/DMC/DEC; cycling was carried out at a voltage range between 2.5 – 4.2 V at a 0.2 C charge and discharge rate. Discharge rate capabilities was tested by charging cells to 4.2 V at 0.1 C rate for the first and last cycle and 0.2 C rate for all other cycles. Cells were discharged at 0.1 C, 0.2 C, 0.5 C, 1 C, 2 C, 5 C and 0.1 C respectively.

### **4.3 Results and Discussion**

#### **4.3.1 Physical Properties**

FTIR results of the uncured OPSZ liquid a) reveal the following characteristic peaks: Si-NH-Si bending mode at 1159 cm<sup>-1</sup>, NH stretching mode at 3380 cm<sup>-1</sup>, and a doublet peaks 1104 and 1074 cm<sup>-1</sup> indicating the presence of SiOCH<sub>2</sub>CH<sub>3</sub>. The liquid precursor was left at ambient temperature open to air for 3 weeks to cure via moisture cure crosslinking. Once the liquid is fully cured, the peaks at 1159 cm<sup>-1</sup> and 3380 cm<sup>-1</sup> disappear. Additionally a peak at 1037 cm<sup>-1</sup> indicating a Si-O-Si stretching mode is present, while the peak at 812 cm<sup>-1</sup> consistent with the

bending mode of the Si-O-Si bond is also present. The peak shifts from the OPSZ liquid to the PDC indicate the liquid is able to undergo a crosslink curing with itself at ambient conditions. The FTIR results of the PAN/PDC fibers can be seen in Figure 4-1b; all samples contain a peak at  $1037\text{ cm}^{-1}$  indicating the presence of Si-O-Si within the fiber. Furthermore, the absence of peaks at  $1159\text{ cm}^{-1}$ ,  $3380\text{ cm}^{-1}$ ,  $1104$  and  $1074\text{ cm}^{-1}$  show the OPSZ has undergone both a TEOS reaction and the Si-N reaction along the backbone of the fiber. During the electrospinning process, the OPSZ precursor was able to react with water in the air to cure into a PDC. These results show that we have successfully made PAN/PDC nanofibers.

It is important that a non-woven separator membrane has uniform fiber morphology to ensure the best performance. The morphology of the non-woven fibers can be seen in Figure 4-2. SEM images of the nonwoven mat shows the separator consists of porous networks composed of uniform, well-formed nanofibers. The fiber diameters range from approximately 390nm to 450nm; with the fiber diameter slightly increasing with the increased ceramic content (Figure 4-2).

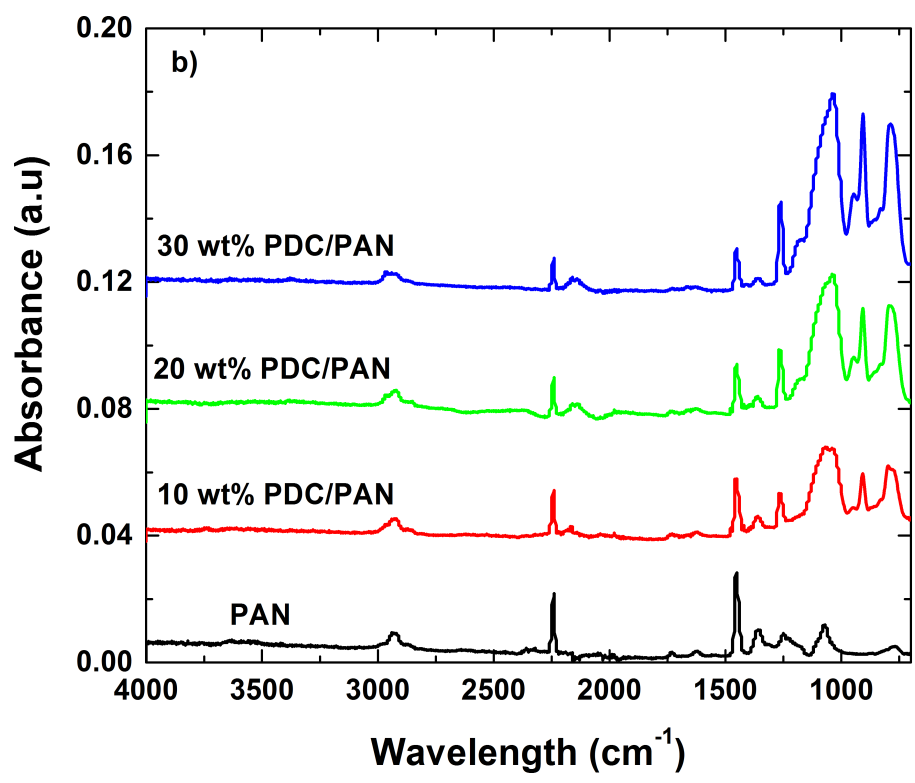
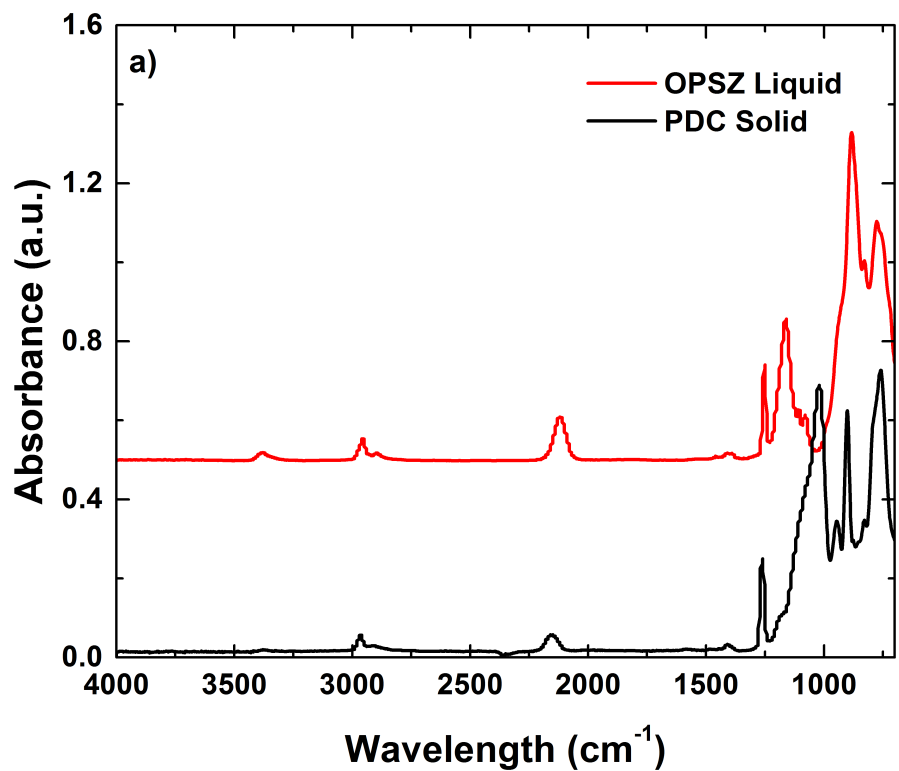


**Figure 4-1** a) FTIR spectra of liquid OPSZ and cured PDC b) FTIR spectra of PAN and PAN/OPZ electrospun membranes

TEM images (Figure 4-3) show the distribution of polymer derived ceramic within the PAN polymer matrix. All three examples show a phase-separated hybrid system with the ceramic phase well distributed across the cross-section the fiber. As the concentration of ceramic increases, the domain sizes also increase from an average of 10 nm for the 90/10wt% fiber (Figure 4-3a-b), 25 nm for the 80/20wt% (Figure 4-3c-d) to 40 nm for the 70/30wt% fiber (Figure 4-3e-f). For the lowest OPZ loading, the larger particles are located toward the center and get smaller in diameter along the radius. The 80/20 wt% fibers, particle sizes become larger and more uniform across the fiber diameter. As the concentration of OPSZ increases, there are more opportunities for the organopolysiloxazane to complete the moisture cure reaction, resulting in larger particles. This is confirmed in the 70/30 wt% sample (Figure 4-3e-f), with the particles appearing larger and more elongated along the fiber axis compared to the two previous samples. For all loadings, there is a thin, 4-6 nm sheath layer on the outside of each nanofiber. EDX measurements done on this area reveal a sheath layer rich in silicon and oxygen (17% Oxygen, 23% silicon), indicating the ceramic forms a sheath layer during the spinning process.

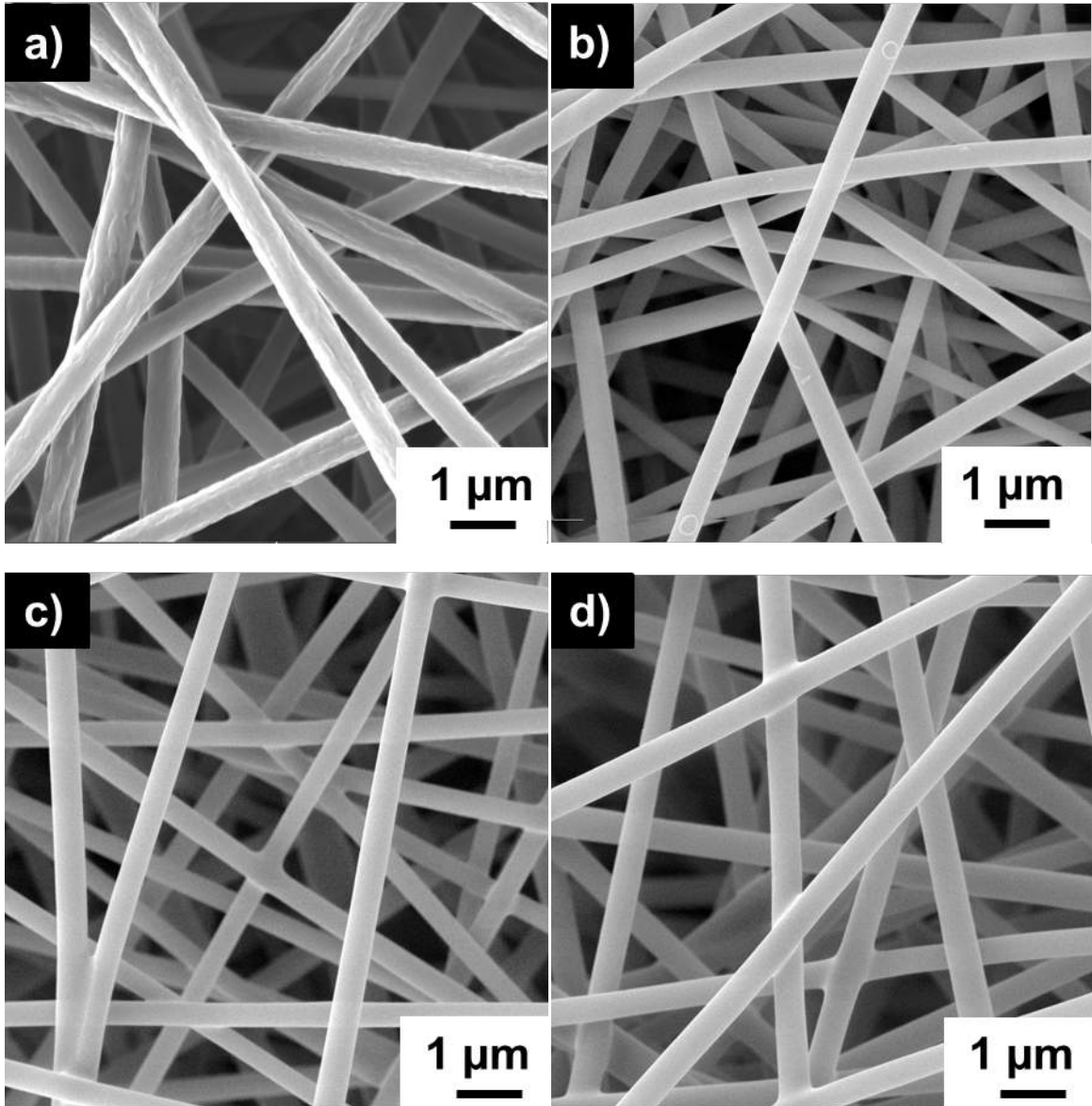


**Figure 4-2** SEM images of electrospun membranes. a) PAN B) PAN/PDC 90:10 wt% c) PAN/PDC 80:20 wt% d) PAN/PDC 70:30 wt%

	Fiber Diameter (nm)	Pore Size Distribution (nm)	Porosity
PAN	439±48	358±58	82
PAN/PDC 90:10	390±74	843±76	83
PAN/PDC 80:20	392±50	463±72	80
PAN/PDC 70:30	490±66	423±100	82

**Table 4-1** Characteristics of PAN/PDC composite separators of various PDC inclusions

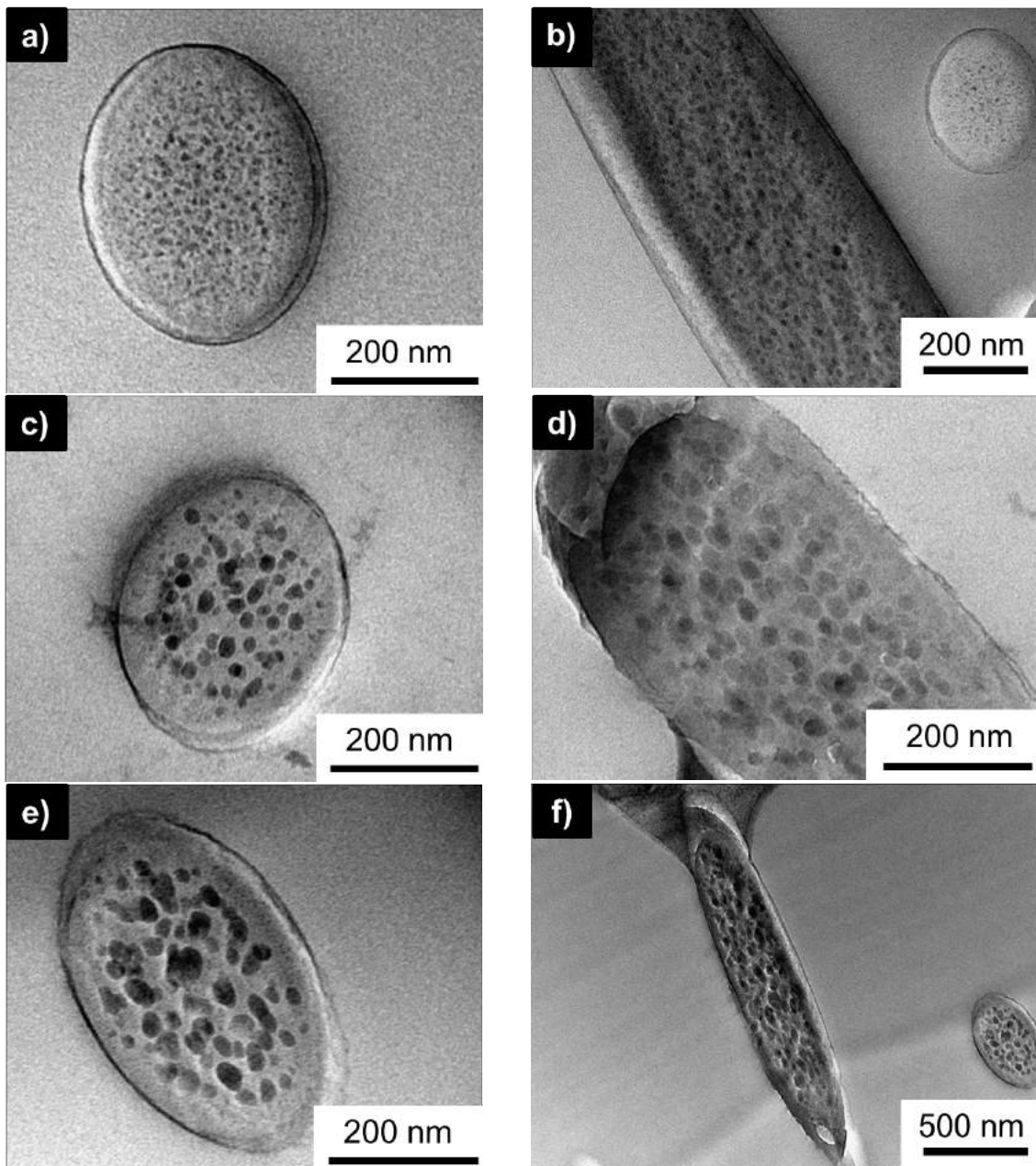


**Figure 4-3** TEM images of PAN/OPZ composite fibers. a-b) cross section and longitudinal view of 10 wt% fibers. c-d) cross section and longitudinal view of 20 wt% fibers. e-f) cross section and longitudinal view of 30 wt% fibers.

Using DMF, the PAN from the composite was removed to reveal the ceramic structure within the fiber. For the 10wt% loading, the ceramic forms small discrete domains as seen in Figure 4-4a. However, as the ceramic content increases the ceramic domain forms a continuous network independent of the polymer matrix. In Figure 4-4b and c, SEM images reveal the ceramic still maintains a fibrous structure, proving the ceramic portion forms its own interconnected domain. At high loadings, the inclusion of PDC leads to a unique co-continuous polymer/ceramic nanofiber morphology.

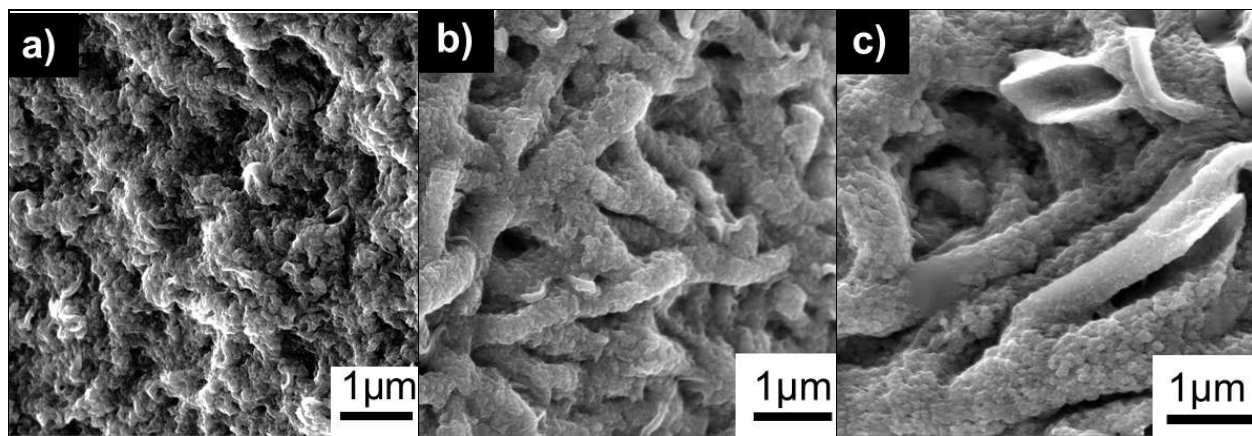


**Figure 4-4** SEM images of fiber mats after PAN has been removed with DMF. a) 10 wt% b) 20 wt% c) 30 wt%

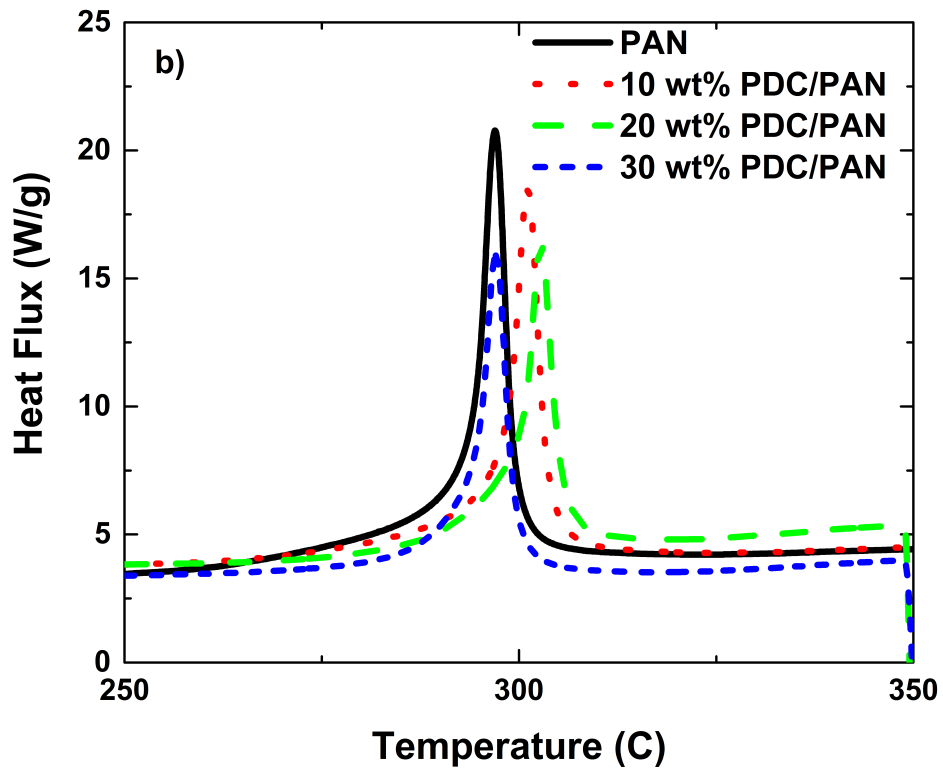
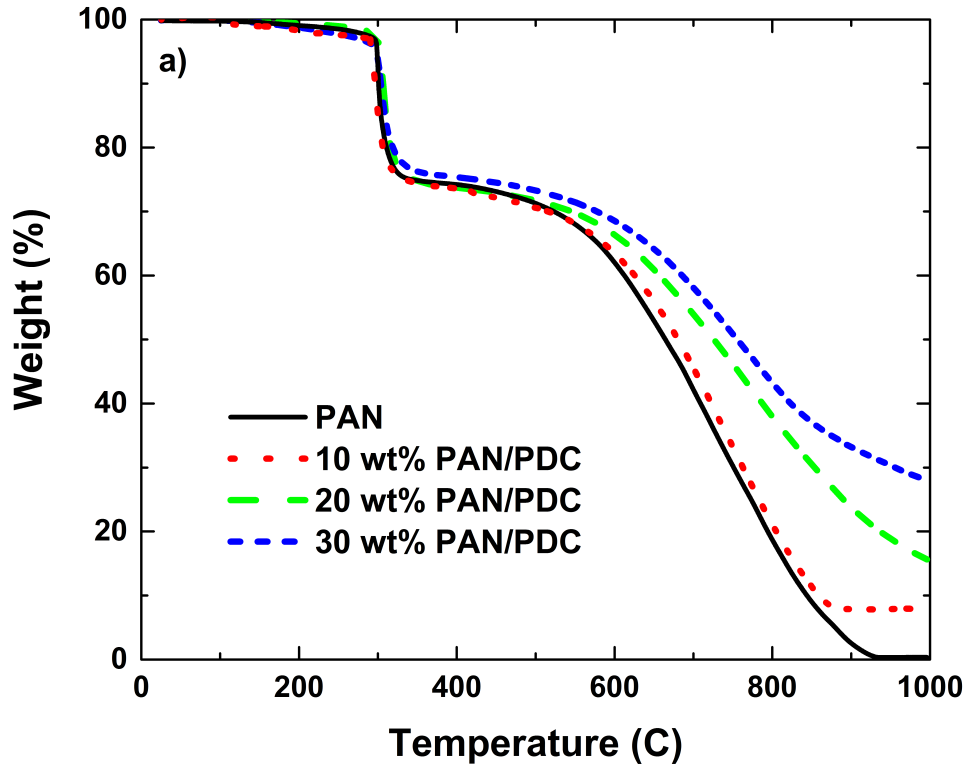


**Figure 4-5** a) TGA isotherms of PAN and PAN/PDC mats. B) DSC measurement showing the cyclization temperature, an exothermic process, of the PAN polymer

TGA analysis was used to confirm both the weight percent inclusion of PDC in the nanofibers and to demonstrate the thermal stability of the non-woven membranes. As the TGA results shown in Figure 4-5a indicate, there is 26%, 17% and 8% residual material after 1000°C for the 30, 20 and 10 wt% samples respectively. These results confirm the OPSZ precursor material fully converted to a ceramic during the electrospinning and annealing process. DSC results (Figure 4-5b) show that the inclusion of PDC also has an effect on the onset of cyclization of the PAN polymer. Pure PAN had a cyclization temperature ( $T_c$ ) of 292°C while the 90/10wt% and 80/20 wt% fibers have  $T_c$  of 294°C and 296°C respectively. This shows the ceramic in having a positive interaction with the polymer network. Similar to previously studied polymer/ceramic matrices, PDC enhances the thermal stability of the polymer matrix.<sup>[24-25]</sup> The increase in cyclization temperature is thought to be a result of the ceramic inhibiting the formation and escape of volatile byproducts generated during the dehydrogenation of PAN. However as the ceramic inclusion increases to 30 wt%,  $T_c$  decreases back to 292°C. This behavior suggests the ceramic and the polymer are now acting as two separate components with no interaction between the two.

In addition to improved thermal stability, good mechanical stability is a desired property of separators for electrochemical applications. Figure 4-6 shows the typical stress/strain curve of PAN and PAN/PDC membranes at various loadings. Young's modulus increased at all loading compared to the pristine PAN membrane; increasing from 101±26 MPa for the PAN separator to 343±32 MPa for the 30wt% loading. In addition for all loadings there is an increase in stress at break. However, it is clear there is a limit on how much ceramic can be added to improve the stress at break. The 20wt% membrane has a stress at break 3 times that is pristine PAN. However as the loading increases to 30wt%, the membrane begins to exhibit brittle behavior due

to the high ceramic loading. The 30wt% sample breaks at the yield point, exhibiting no ductile behavior. However even considering this drawback, the 30wt% membrane still has superior strength compared to the PAN membrane.

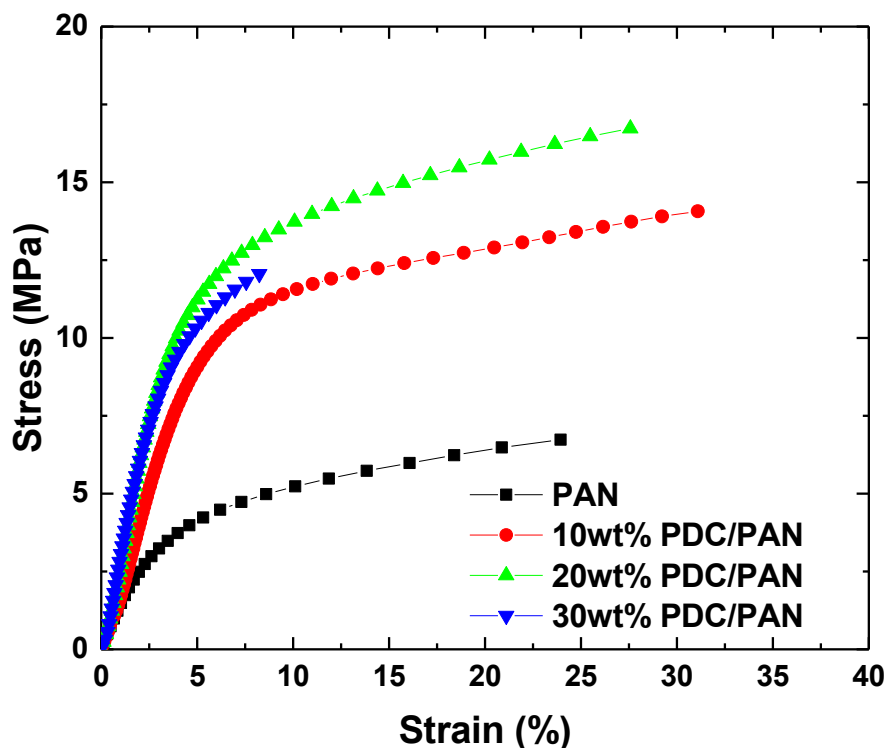


**Figure 4-6** DMA showing the mechanical stability of PAN and PAN/PDC membranes

Figure 4-7 shows the XRD patterns of the PAN membrane as well as the PAN/PDC membranes with various ceramic loadings. The XRD pattern of the pure PAN membrane shows a strong peak at  $17^\circ$  and a weak broad peak at  $28^\circ$ ; the peak at  $17^\circ$  corresponding to (0 1 0) plane with d spacing of  $5.3 \text{ \AA}$ .<sup>[26-27]</sup> As more ceramic is added the peak at  $17^\circ$  becomes weaker and the peak at  $28^\circ$  disappears. This indicates that the inclusion of PDC ceramic enhances the amorphous phase of the PAN polymer.

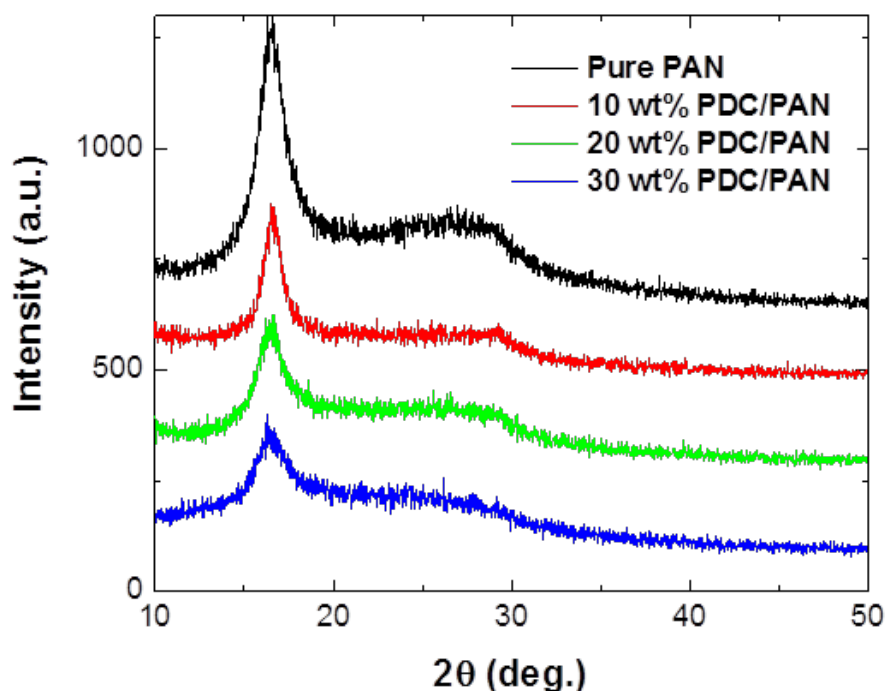


**Figure 4-7** XRD patterns of electrospun PAN/PDC composite membranes with various ceramic contents

How well a separator wets with electrolyte is a good indication of how well the electrolyte is diffusing in the separator and also how effectively the separator can retain electrolyte.<sup>[3]</sup> Figure 4-8 shows the dynamic contact angle measurements of the microporous PP, PAN and the PAN/PDC nonwovens. All nonwoven membranes show superior electrolyte uptake due to increased porosity. The hydrophobic nature of the PDC ceramic works well with the organic EC/DMC/DEC electrolyte used in the system to create a more favorable interaction between the separator and electrolyte. As time increases, the contact angle between the PAN/PDC separators is decreasing more rapidly than the PAN separator. This indicates better absorption of the electrolyte into the pores of the polymer/ceramic separators. Comparing the PAN/PDC samples, it's clear an increase in ceramic material also correlates with a decrease in contact angle. Improved polymer membrane/electrolyte interaction is further evidenced in Figure

4-8b with electrolyte uptake results. The electrolyte uptake of microporous polyolefin membrane is 148% which is more than 5 times less than that of the pure PAN sample. The low porosity (~42%) of the polyolefin membrane and the hydrophobic nature of the polymers leads to its low electrolyte uptake. However the high porosity of the PAN and PAN/PDC increases the uptake significantly by being able to trap and retain more electrolyte. Comparing the PAN and the PAN/PDC membranes, there is an increase in the electrolyte uptake with increased ceramic content. This is due to an increase in the amorphous nature of the PAN polymer, while in the ceramic as seen in Figure 4-7. The ceramic present in the membranes is also amorphous, and thus solely increasing the amount of ceramic, increases the overall amorphous content of the membrane.

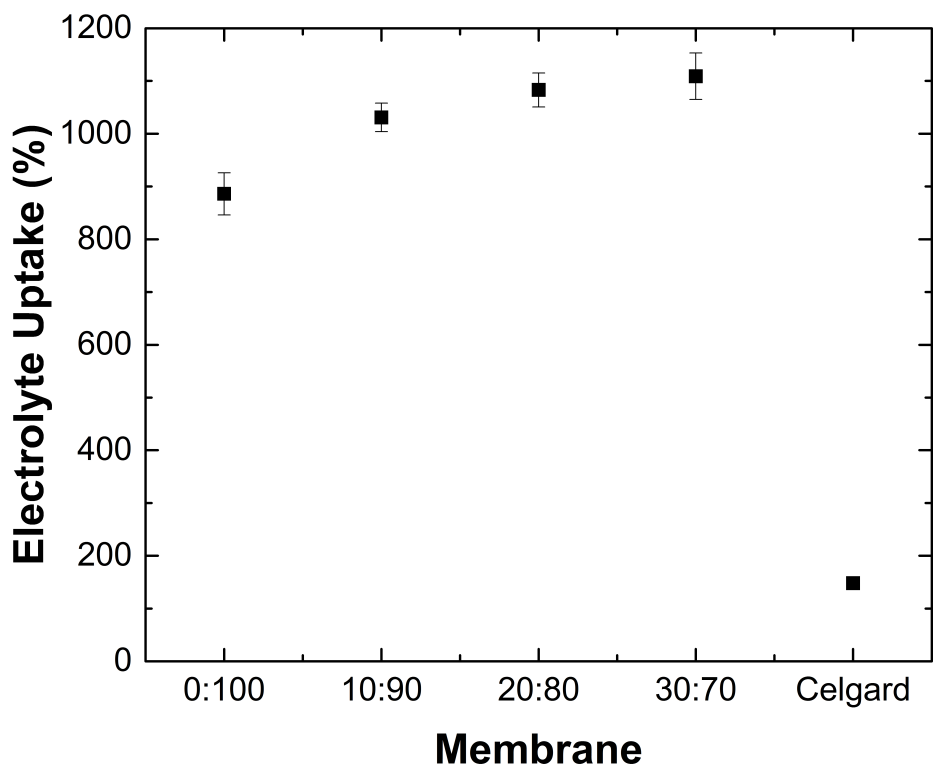
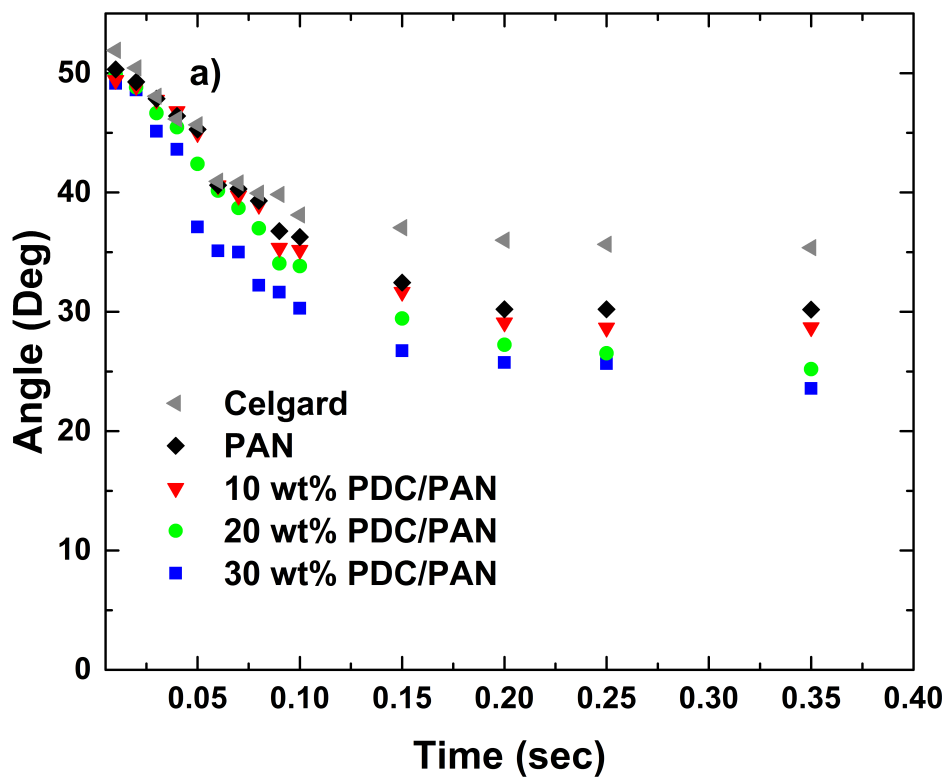


**Figure 4-8** a) Dynamic contact angle measurements as a function of time using various membranes b) Variations of electrolyte uptake in electrospun PAN/PDC composite membranes with PDC content.

### 4.3.2 Electrochemical Performance

The ionic conductivity of a li-ion separator helps with the transport of ions during the charge-discharge process of the batteries. The Nyquist plot of the results for all separators can be seen in Figure 4-9. The high frequency intercept of the semi-circle with the  $ZRe$  intercept represents the bulk resistance,  $R_b$ . Since the graph doesn't intercept, the curve is fitted using  $Zview$  using the equivalent circuit seen in insert. Ionic conductivity can then be determined using

$$\delta = \frac{d}{S \times R_b}$$

where,  $\delta$  is ionic conductivity,  $d$  is the thickness of the separator membrane,  $S$  is the area of the lithium electrode and  $R_b$  is the bulk resistance. The calculated ionic conductivity of all separators tested displayed in Table 4-2. Similar to previous works, the ionic conductivity of PAN is improved compared to Celgard 2400 due to increased porosity and electrolyte uptake. The results show the PAN/ceramic separators have a higher ionic conductivity compared to the PAN electrospun membrane. As the concentration of PDC increases, there is an increase in the ionic conductivity, with the 70wt% PAN/PDC separator having an ionic conductivity value three times that of the plain PAN separator membrane. Increase in ionic conductivity due to ceramic inclusion has been well documented.<sup>[28-30]</sup> The increase in ionic conductivity can be attributed to a number of factors including: pore structure within the membrane to trap the electrolyte, increase in amorphous regions of the polymer due to inorganic inclusion, and ceramics acting as the Lewis acid-base center that promote salt disassociation which could free more cations.<sup>[29][30]</sup> Referring to Table 4-1, the pore sizes of 70wt% PAN/PDC membrane is the smallest among the polymer/ceramic samples, this enabled it to provide good ionic channels and high liquid electrolyte uptake in pores without leakage. The membranes with the highest ceramic content

also have the lowest crystallinity and highest electrolyte uptake, leading to the increase in ionic conductivity.

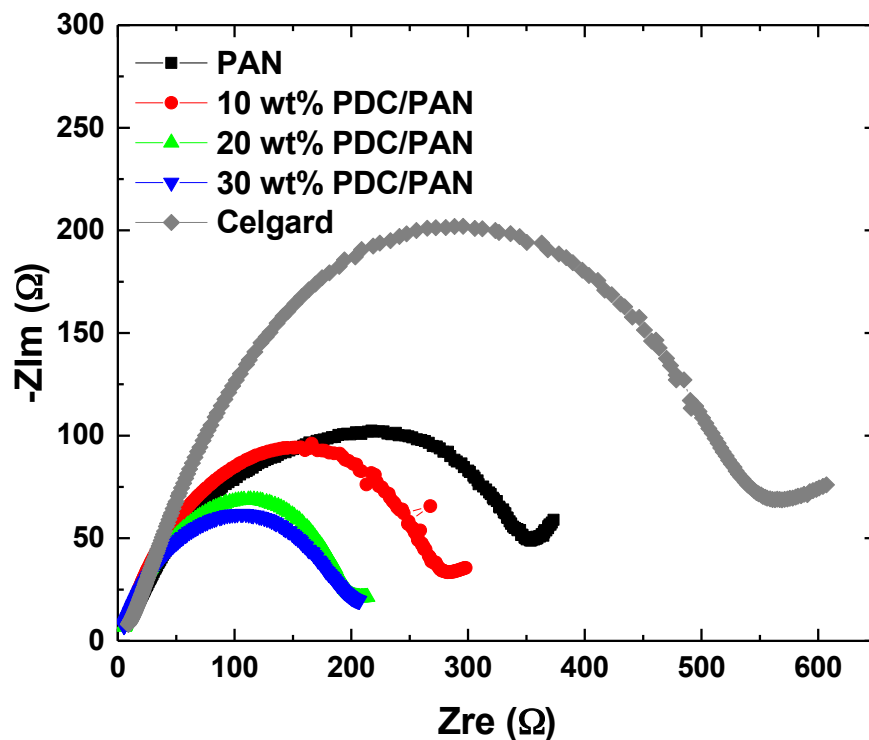


**Figure 4-9** Nyquist plots for the cells with Celgard, PAN membrane, 90:10wt%, 80:20wt%, 70:30wt% PAN/PDC membranes respectively.

Membrane	Ionic Conductivity (mS/cm)
Celgard	0.22
PAN	0.29
PAN/10wt% PDC	0.51
PAN/20wt% PDC	0.80
PAN/30wt% PDC	1.14

**Table 4-2** Electrochemical impedance spectra (EIS) of various separators

Figure 4-10 shows the discharge capacity of LiCoO<sub>2</sub>/graphite full cells using various separators. Figure 4-10a show the cycling performance at a 0.2C rate. The initial discharge

capacities for Celgard was 131 mAh/g, while the initial discharge capacity for the PAN/PDC cells were 135 mAh/g. Over the life cycle of the battery, the PAN/PDC membranes had the highest capacity retention, 93%, 90% and 89% for the 10, 20 and 30wt% PAN/PDC membranes respectively compared to 85% retention for Celgard. Increase in initial capacity and capacity retention can be attributed to the increased electrolyte uptake and ionic conductivity caused by ceramic inclusion. When the charge rate is increased to 0.5C, a similar trend is seen (Figure 4-10b). The membrane with the highest ceramic loading, 30 wt%, maintained a 92 percent capacity retention after 100 cycles. The pure PAN membrane is only able to maintain an 80% capacity retention and the Celgard membrane performance has the poorest performance with a 63 percent capacity retention after 100 cycles.

Rate capability of cells with various separators can be seen in Figure 4-11. Similar to the 0.5C testing, PAN/PDC cells begin with a higher initial discharge capacity, 135 mAh/g for the PAN/PDC 70:30wt% cell compared to 128 mAh/g for the PAN cell. As the cycling continues, PAN/PDC separators continuously exhibit an average 10 mAh/g improvement over the PAN separator. PAN/PDC separators demonstrate very stable cycling behavior over a range of charge rates maintaining over a 90% retention of the 0.1C capacity at 1C, while the PAN cell has fallen to 80% retention at 1C. As the charge rate is increased to 5C, the rate retention rates are 38%, 41%, 53%, and 53% for the PAN, PAN/PDC 90:10 wt%, 80:20 wt%, and 70:30 wt% cells respectively. As the cells are brought back to a gentler cycling rate, 0.1C, it is clear the separator used as an impact on the battery's ability to recover after such a high charge rate. The PDC samples all immediately regain discharge capacities similar to the capacities at 0.2C charge rate, approximately 90% of the initial C/10 capacity. While the PAN separator is only able to recover to a previous 1C conditions, with a 105 mAh/g capacity, 80% of the initial C/10 capacity.

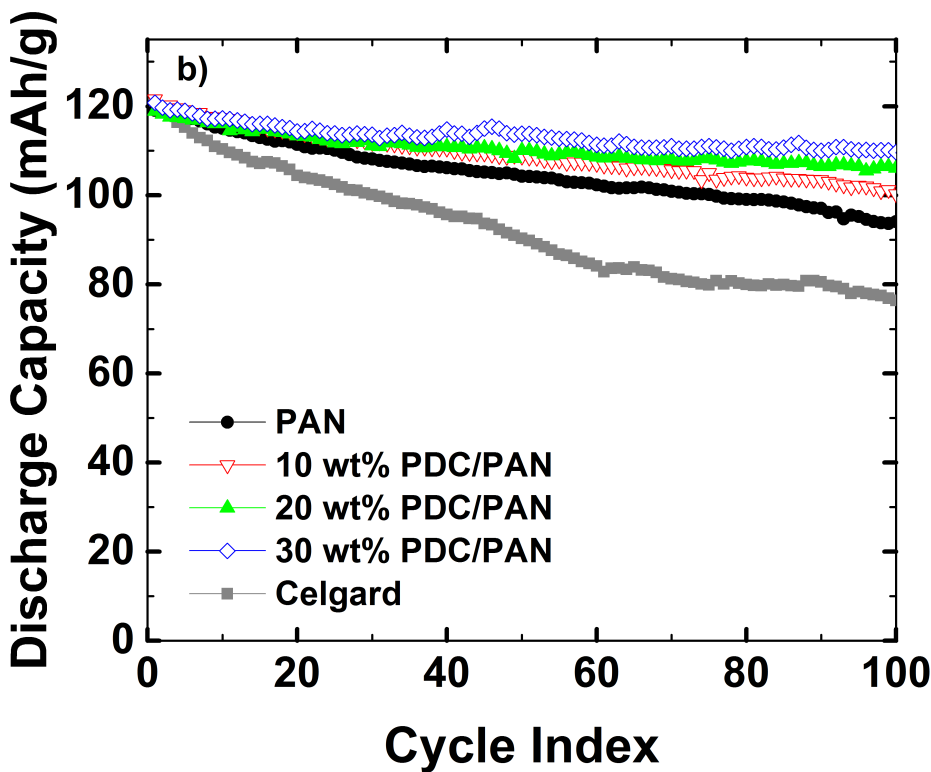
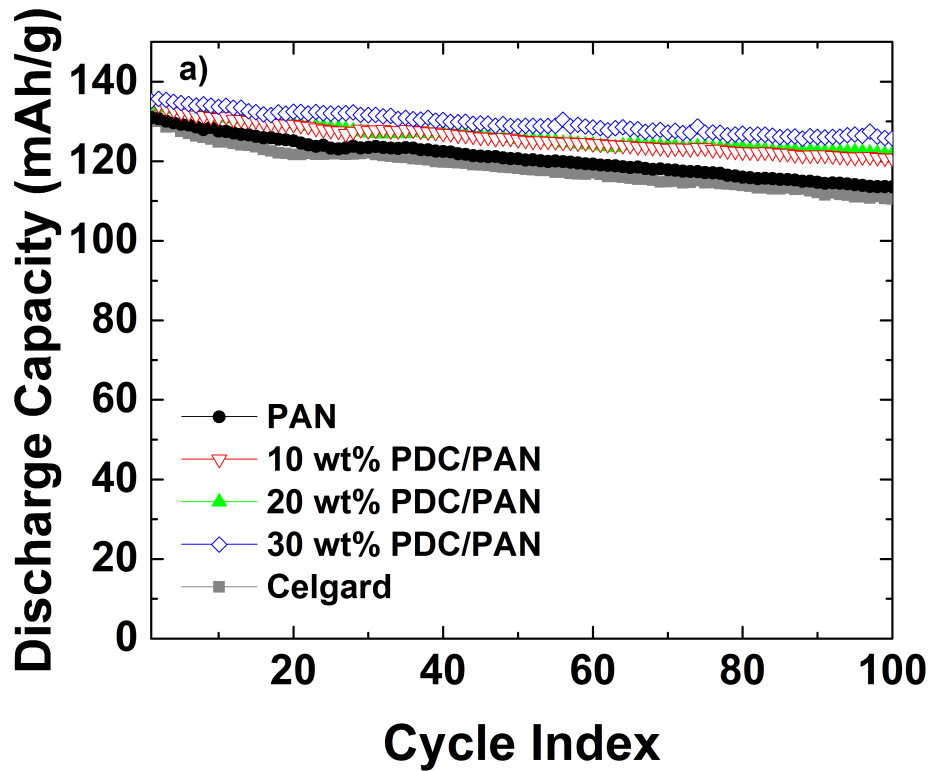


**Figure 4-10** Cycle performance of LiCoO<sub>2</sub>/graphite full cells with various separator membranes at 0.2C

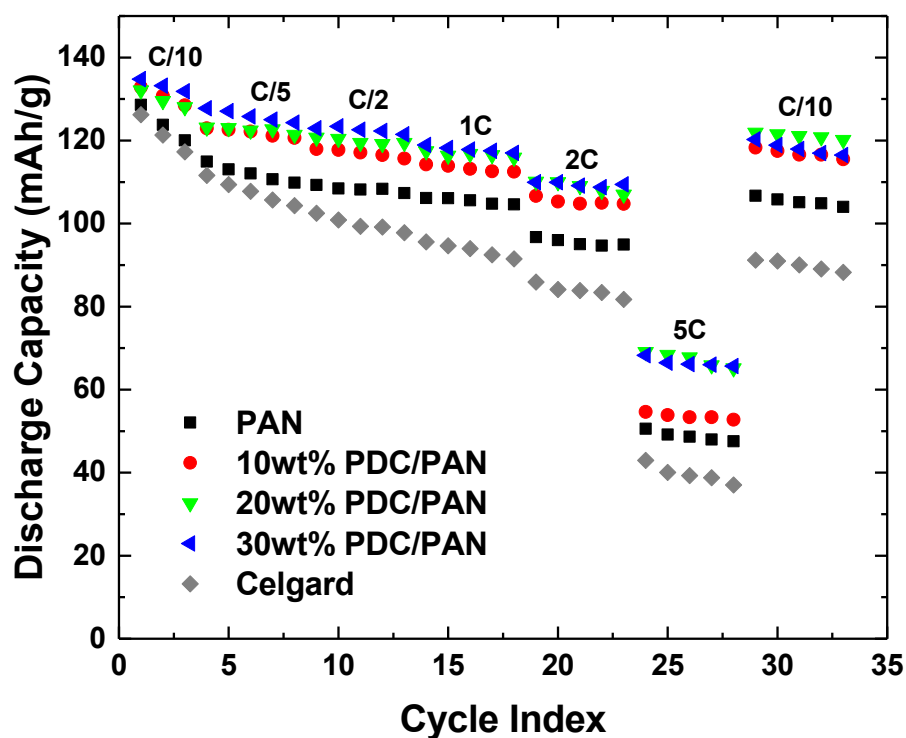


**Figure 4-11** Results of rate capability tests for the LiCoO<sub>2</sub>/graphite full cells with various separator membranes

#### 4.4 Conclusion

We have successfully created a PAN/PDC hybrid nanofiber using the electrospinning method. Fiber membranes created had an average thickness of 27  $\mu\text{m}$ , with porosity averaging 80%. TEM images confirmed the PDC is well distributed within the fiber, forming an interconnected ceramic network within the fiber, while a thin sheath layer of ceramic is observed on the fiber surface. Incorporation of PDC in the PAN leads to an increase in both thermal and mechanical stability over the pristine fiber. Additionally, there was a decrease in contact angle between the membranes and electrolyte and an increase in electrolyte uptake leading to an increase in ionic conductivity. Over 100 cycles, the PAN/PDC membranes demonstrated increased initial

discharge capacity and capacity retention compared to the PAN compound and microporous polyolefin membranes. These results suggest that the increased ionic conductivity is correlated to an increase in battery performance and capacity retention especially at high charge/discharge rates. All nanofiber based separators in the current study have the similar porosity around 80%, and they exhibit a wide range of the rate capability performances due to their different internal and surface morphologies of nanofibers which in turn affect the ionic conductivity.

## References

- [1] P. Arora, Z. Zhang, *Chem. Rev.* **2004**, *104*, 4419.
- [2] X. Huang, *J. Solid State Electrochem.* **2010**, *15*, 649.
- [3] S.S. Zhang, *J. Power Sources* **2007**, *164*, 351.
- [4] S. Cavaliere, S. Subianto, I. Savych, D.J. Jones, J. Rozière, *Energy Environ. Sci.* **2011**, *4*, 4761.
- [5] M.-H. Ryou, D.J. Lee, J.-N. Lee, Y.M. Lee, J.-K. Park, J.W. Choi, *Adv. Energy Mater.* **2012**, *2*, 645.
- [6] J. Miao, M. Miyauchi, T.J. Simmons, J.S. Dordick, R.J. Linhardt, *J. Nanosci. Nanotechnol.* **2010**, *10*, 5507.
- [7] C.M. Costa, J. Nunes-Pereira, L.C. Rodrigues, M.M. Silva, J.L.G. Ribelles, S. Lanceros-Méndez, *Electrochimica Acta* **2013**, *88*, 473.
- [8] J. Hao, G. Lei, Z. Li, L. Wu, Q. Xiao, L. Wang, *J. Membr. Sci.* **2013**, *428*, 11.
- [9] T.-H. Cho, M. Tanaka, H. Onishi, Y. Kondo, T. Nakamura, H. Yamazaki, S. Tanase, T. Sakai, *J. Power Sources* **2008**, *181*, 155.
- [10] H.-R. Jung, D.-H. Ju, W.-J. Lee, X. Zhang, *Electrochimica Acta* **2009**, *54*, 3630.
- [11] C. Yang, Z. Jia, Z. Guan, L. Wang, *J. Power Sources* **2009**, *189*, 716.
- [12] Y. Liang, S. Cheng, J. Zhao, C. Zhang, S. Sun, N. Zhou, Y. Qiu, X. Zhang, *J. Power Sources* **2013**, *240*, 204.
- [13] K.S. Jeon, R. Nirmala, R. Navamathavan, K.J. Kim, S.H. Chae, T.W. Kim, H.Y. Kim, S.J. Park, *Mater. Lett.* **2014**, *132*, 384.

- [14] Y.-E. Miao, G.-N. Zhu, H. Hou, Y.-Y. Xia, *J. Power Sources* **2013**, 226, 82.
- [15] A.I. Gopalan, P. Santhosh, K.M. Manesh, J.H. Nho, S.H. Kim, C.-G. Hwang, K.-P. Lee, *J. Membr. Sci.* **2008**, 325, 683.
- [16] T.H. Cho, T. Sakai, S. Tanase, K. Kimura, *Electrochem. Solid-State Lett.* **2007**, 10, A159.
- [17] E.-S. Choi, S.-Y. Lee, *J. Mater. Chem.* **2011**, 21, 14747.
- [18] H.-S. Jeong, E.-S. Choi, S.-Y. Lee, *Electrochimica Acta* **2012**, 86, 317.
- [19] H. Liu, J. Xu, B. Guo, X. He, *Ceram. Int.* **2014**, 40, 14105.
- [20] H.-S. Jeong, S.C. Hong, S.-Y. Lee, *J. Membr. Sci.* **2010**, 364, 177.
- [21] H.-S. Jeong, E.-S. Choi, S.-Y. Lee, J.H. Kim, *J. Membr. Sci.* **2012**, 415–416, 513.
- [22] J.-A. Choi, S.H. Kim, D.-W. Kim, *J. Power Sources* **2010**, 195, 6192.
- [23] X. Huang, D. Bahrolloomi, X. Xiao, *J. Solid State Electrochem.* **2013**, 18, 133.
- [24] L. Ji, X. Zhang, *Mater. Lett.* **2008**, 62, 2161.
- [25] M. Naffakh, A.M. Díez-Pascual, *Inorganics* **2014**, 2, 291.
- [26] S.W. Choi, J.R. Kim, S.M. Jo, W.S. Lee, *J. Electrochem. Soc.* **2005**, 152, A989.
- [27] M. Sokół, E. Turska, *Acta Polym.* **1984**, 35, 135.
- [28] J. Li, X. Huang, L. Chen, *J. Electrochem. Soc.* **2000**, 147, 2653.
- [29] S.H. Chung, Y. Wang, L. Persi, F. Croce, S.G. Greenbaum, B. Scrosati, E. Plichta, *J. Power Sources* **2001**, 97–98, 644.
- [30] F. Croce, G.B. Appetecchi, L. Persi, B. Scrosati, *Nature* **1998**, 394, 456.
- [31] L. Xu, F. Xu, F. Chen, J. Yang, M. Zhong, L. Xu, F. Xu, F. Chen, J. Yang, M. Zhong, *J. Nanomater. J. Nanomater.* **2011**, 2012, 2012, e457967.
- [32] X. Huang, *J. Power Sources* **2011**, 196, 8125.

## **Chapter 5 Impact of The Structure of Room-Curable Organopolysilazane on the Performance of Electrospun PAN/Polymer Derived Ceramic Composite Nanofiber Membranes for Lithium Ion Battery Separators**

### **Abstract**

Electrospun polyacrylonitrile(PAN)/ceramic fibers were created by combining the PAN polymer and various room temperature curing organopolysilazane (OPSZ) precursors in a one step electrospinning process. The resultant PAN/ceramic (70:30) hybrid fibers mats consisted of well-formed uniform fibers with evenly distributed ceramic both in the longitudinal and cross-sections of the fibers. The presence of tetraethyl orthosilicate (TEOS) pendant chain attached to the polysilazane (PSZ) backbone impacted the ability of the ceramic to form a continuous ceramic network within the polymer network. Results show the membranes with an interconnected ceramic domain showed superior mechanical and electrochemical properties. Batteries containing 40 wt% TEOS:PSZ and 20 wt% TEOS:PSZ separators showed greater than 90 percent capacity retention at a C/5 discharge rates after 100 cycles. Rate capability tests show a similar trend with 40 wt% TEOS:PSZ and 20 wt% TEOS:PSZ membranes maintaining greater capacity retention even at high charge rates.

### **5.1 Introduction**

Lithium ion batteries (LIB) play a crucial role in the expanding growth of portable electronic devices (e.g. digital camera, laptop, smartphone) and the electronic vehicles (EV) market, due to their high energy density, light-weight, long lifespan, and environmental friendliness.<sup>1-4</sup> As our use of these devices continues to increase, the need for more efficient lithium ion batteries becomes more apparent. The separator is a membrane which lies between the cathode and anode in electrochemical cell that requires a liquid electrolyte, serves as a physical barrier to prevent short circuiting. Though the separator must be present within a small

compact battery, it should be as thin as possible as to reduce cell resistance and also porous to aid in ion transport. In addition, separators should be mechanically, thermally, and electrochemically stable over the operative temperature range of the battery.<sup>5</sup> Commercially, the most widely commonly used separators are polyolefin membranes, which fulfill some of the previously mentioned criteria but they also possess many disadvantages. Due to the hydrophobic nature of polyolefins polymer used to make the membranes, there are issues with low electrolyte uptake and wettability.<sup>6</sup> These combined factors of poor wettability and low porosity lead to poor ionic transport over the lifetime of the early batteries containing polyolefin separators.

In order to improve the ionic transport, researchers first increased the porosity of separator membranes by producing non-woven membranes made by the electrospinning technique.<sup>7-9</sup> Electrospun membranes have been made from a variety of polymers including polyethylene terephthalate (PET)<sup>10</sup>, polyacrylonitrile (PAN)<sup>11,12</sup>, and polyvinylidene fluoride (PVDF)<sup>13</sup>. Electrospun membranes result in a highly porous fiber network with an average porosity of 70-80 percent, with Jung et al.<sup>11</sup> reporting porosities as high as 90 percent. This increase in porosity is correlated with an increase in ionic conductivity due to a higher effective diffusivity of the electrospun membranes. In addition, the use of less hydrophobic materials leads to increases in electrolyte uptake and retention. All these factors lead to batteries with higher discharge capacity and superior capacity retention compared to Celgard.

Both commercially and in academic institutions, researchers are incorporating inorganic ceramic fillers and coating to their polymer separators. The most commonly used ceramic are aluminum oxide ( $\text{Al}_2\text{O}_3$ )<sup>14-18</sup> and silicon dioxide ( $\text{SiO}_2$ )<sup>19-22</sup>. These polymer/ceramic composite membranes are made by two methods: 1) incorporating the ceramic directly into the polymer matrix<sup>11,23,24</sup>, 2) coating of the membrane.<sup>25</sup> Membranes with ceramic have shown superior

electrochemical performance compared to the neat polymer membranes and polyolefin separators. The improved electrochemical performance is attributed to ceramics deterring polymer crystallization or contributes to highly conductive interfaces between the ceramic and polymer.<sup>19,26</sup> Ceramics can also increase the surface area of the membrane by introducing mesopores (~2-50nm) which dramatically increases the ionic conductivity.<sup>11,24</sup> However, the dip-coating method can lead to issues of ceramic delamination which could lessen the impact of the ceramic in the battery.<sup>27</sup> In addition, the use of particles within the polymer matrix requires extensive sonication to ensure good ceramic particle dispersion and the amount of ceramic that can be incorporated into the polymer is limited. After a certain percentage, ceramic particles will not disperse well leading to aggregation and a reduction in ionic conductivity and cycling performance.<sup>11</sup>

In this paper, polymer/ceramic non-wovens were created using a one-step electrospinning process using three different organopolysiloxazane(OPSZ). The three precursors have a similar chemical backbone but differ on the ratios of the tetraethyl orthosilicate (TEOS) pendant chain attached to the polysilazane (PSZ) backbone. All OPSZ solutions are miscible in the PAN/DMF polymer solution allowing the OPSZ to be mixed easily in the solution creating a solution that is easy to electrospin into polymer/ceramic nanofibers without the need for sonication for further post treatment. The three different precursors used resulted in three different polymer derived ceramic (PDC) with varying elemental ratios. The presence of TEOS chains enables the ceramic to form an independently connected ceramic network within the polymer differing it from the discrete ceramic materials that have been used in the past. TEM images show the resultant fibers contain both ceramic inside the fiber as well as a sheath layer on the outside. This unique

morphology had an impact on the mechanical, thermal and electrochemical performances of separators.

## **5.2 Experimental**

### **5.2.1 Material Preparation**

The PAN/ceramic non-woven separator was prepared using the electrospinning method. The electrospinning solution was prepared by combining polyacrylonitrile (PAN,  $M_w = 200,000$ , Polysciences) with N,N-Dimethylformamide (DMF) to form a 8wt% solution. The solution was placed in a 95°C oven for 12 hours to thoroughly dissolve the polymer. The PAN/DMF solution was then left to cool to room temperature. Ceramic precursors, organopolysilazanes (EMD Performance Materials), were added to obtain 30 wt% ceramic in relation to the PAN. The mixture was stirred on a vortex mixer for two minutes to ensure thorough mixing of the components. The solution was let to sit for 10 minutes to allowed any bubbles within the solution is disappear before spinning the solution.

The PAN/OPSZ solution was electrospun at a flow rate of 0.6 mL/hr for both the 20 wt% and 40wt% TEOS:OPSZ solutions and 0.72 mL/hr for the 0 wt% TEOS:PSZ solution using a 20-gauge needle. A 17.5 kV voltage and 16 cm distance between the needle and the collector plate was used for all samples. The collected samples were then annealed at 120°C for 12 hours to ensure the removal of all residual solvent.

### **5.2.2 Characterization**

The fiber morphology and diameter were examined using scanning electron microscopy (Tecsa Mira3 Field Emission SEM) with an accelerating voltage of 5kV. The average fiber diameters were determined by choosing 100 randomly selected fibers using Image J. In order to

investigate, the structure of the ceramic within the fibers, membranes were soaked in DMF for 24 hours in order ensure total removal of PAN. Samples were then dried and imaged using the Tescan SEM. The morphology of the cross section of the fibers was investigated by transmission electron microscopy (FEI Tecnai G2 T12 Spirit TEM STEM). Thermal stability was characterized using differential scanning calorimetry (DSC, TA Instrument Q200) under nitrogen from 40°C to 350°C at a 10°C/min. Wide angle X-ray diffraction (XRD) patterns were recorded from 10° to 70° for all prepared electrospun membranes using Theta-Theta X-ray Diffractometer (Scintag) with Cu radiation ( $\lambda = 1.5405\text{\AA}$ ; 40 mA and 40 kV). XRD was also used to estimate fiber crystallinity. Elemental composition of ceramic component was done using X-ray photoelectron spectroscopy (XPS, Surface Science Instruments SSX-100). The separator/electrolyte interaction was estimated by measuring the dynamic change in contact angle between the electrolyte and the separator using a high speed camera capturing images every 0.001 sec. Electrolyte uptake is calculated using the following relation:

$$Uptake (\%) = \frac{M_a - M_i}{M_i} \times 100 \quad (1)$$

where  $M_a$  and  $M_i$  are the masses of the wet and dry membrane respectively. The porosity ( $P$ ) of the fabricated membranes was calculated by using the measured data and the density of material with the equation below.<sup>28</sup>

$$P = 1 - \left( \frac{W}{\rho \cdot V} \right) \quad (2)$$

where  $W$  is the dried membrane weight,  $\rho$  the membrane density, and  $V$  the apparent volume of the membrane. The membrane thickness was measured by a digital thickness gauge.

Electrochemical test are carried out in a 2302 coin cell. Cell impedance was measured by sandwiching the separator membrane between two lithium disks inside a cell. The cells were tested on a PARSTAT 4000 (Princeton Applied Research), with the impedance measurements at an amplitude of 5 mV over a frequency range of 20000 kHz to 1 Hz.

Full cells consisted of a  $\text{LiCoO}_2$  cathode (MTI Corporation), a graphite anode (MTI Corporation), and  $\text{LiPF}_6\text{-EC/DMC/DEC}$  electrolyte; cycling was carried out at a voltage range between 2.5 – 4.2 V at 0.2C and 0.5 C charge and discharge rates. Discharge rate capabilities was tested by charging cells to 4.2 V at 0.1 C rate for the first and last cycle and 0.2 C rate for all other cycles. Cells were discharged at 0.1 C, 0.2 C, 0.5 C, 1 C, 2 C, 5 C and 0.1 C respectively.

### 5.3 Results and Discussion

It is important to keep the amount of precursor in each sample the same to make sure we are having a fair comparison between the membranes. Each membrane was weighed before and after being placed in the 120°C oven. There is minimal weight change in the membranes (Table 5-1), showing there no thermal degradation of the ceramic or the polymer at that temperature. The minimal weight lost observed is due the evaporation of water from the membrane.

Sample Membrane	Initial weight (mg)	Final Weight (mg)	Weight Change (%)
0wt% TEOS:PSZ	13.20	13.07	1
20wt% TEOS:PSZ	18.04	17.62	2
40wt% TEOS:PSZ	10.87	10.73	1

**Table 5-1** Weight change in polymer/ceramic hybrid fibers after annealing

During the electrospinning process, all three precursors undergo a moisture crosslinking converting the three OPSZ precursors to polymer-derived ceramics.<sup>29</sup> OPSZ precursors can undergo room temperature curing in two ways: 1) hydrolysis reaction via the TEOS pendant

chains, 2) reaction along to Si-N backbone similar to the sol-gel reaction seen with perhydropolysilazane (PHPS)<sup>30</sup>. After a DMF rinse of the membranes to remove PAN, XPS analysis was done to determine the chemical composition of the resulting ceramic inside each fiber mat. The chemical composition of the three OPSZ precursors and resulting polymer-derived ceramics are shown in Table 5-2. As the precursors cure, there is a reduction in the percentage of nitrogen and an increase in the percentage of oxygen due to its reactions with moisture in the atmosphere. Figure 5-1 shows external and internal morphology of the various nonwoven fiber PAN/PDC mats. SEM images (Figure 5-1 a,d,g) show well-formed fibers, free of beads and droplets. Fiber characteristics including fiber diameter and porosity are presented in Table 5-3. There is a decrease in fiber diameter with TEOS ratio along the precursor backbone. This suggests that the gelling of the TEOS chains during the spinning process helps reduce fiber entanglement leading to smaller fibers. This is similar to previous works which show the increase in SiO<sub>2</sub> results in a decrease in fiber diameter due to repulsive force minimizing polymer entanglement.<sup>11,22</sup>

Sample	Si (%)	O (%)	C (%)	N (%)
40 wt% TEOS:PSZ Before	32	14	33	12
<b>40 wt% TEOS:PSZ After</b>	<b>15</b>	<b>25</b>	<b>50</b>	<b>9</b>
20 wt% TEOS:PSZ Before	38	7	29	17
<b>20 wt% TEOS:PSZ After</b>	<b>10</b>	<b>19</b>	<b>57</b>	<b>13</b>
0 wt% TEOS:PSZ Before	44	0	25	22
<b>0 wt% TEOS:PSZ After</b>	<b>21</b>	<b>29</b>	<b>43</b>	<b>6</b>

**Table 5-2** Elemental composition of OPSZ precursors and resultant ceramic inside the fiber after electrospinning

TEM images reveal the ceramic is evenly dispersed within the fibers along the fiber axis for all samples. TEM images also show the ceramic forms a continuous sheath layer (approximately 5nm thick) around all fibers followed by a space void of ceramic towards the edge of the fiber. Towards the fiber center, there is also ceramic present dispersed within the polymer matrix. Domain sizes of the ceramic within the fiber decrease with increasing TEOS percentage; 0wt% TEOS:PSZ fibers have domain size of  $40\pm 3$ nm, 20 wt% and 40 wt% TEOS:PSZ fiber have domain sizes of  $25\pm 2$  nm and  $38\pm 3$  nm respectively. Removal of the PAN polymer with a DMF rinse reveals the structure of the ceramic within the polymer network (Figure 5-2). Figure 5-2 a. and b. show the ceramic within the 40 wt% TEOS:PSZ and 20 wt% TEOS:PSZ fibers form a connected network independent of the polymer matrix. Further magnification of the ceramic fiber surface (Figure 5-2 d-e) reveals the ceramic fibers appear to be porous. The porosity of the fiber surface indicates the PAN polymer and the ceramic intertwine along the fiber axis forming a co-continuous network. In contrast to the other two fibers, the 0 wt% TEOS:PSZ ceramic does not form a continuous network within the fiber. Instead the 0 wt % TEOS:PSZ ceramic forms small discrete domains. The inability of 0 wt% TEOS:PSZ to form a connected ceramic network could be due to the lack of TEOS branches on the original precursor backbone. The TEOS branches dramatically increase the amount of available reactive sites along the precursor backbone to react with other OPSZ chains. The increased reaction sites enabled the connected ceramic network seen in the 40 wt% TEOS:PSZ and 20 wt% TEOS:PSZ samples. In addition, the 0 wt% precursors has the fastest curing rate among the precursors, the fast curing rate of the 0 wt% precursors allows it to gel and solidify before it can create a continuous structure.

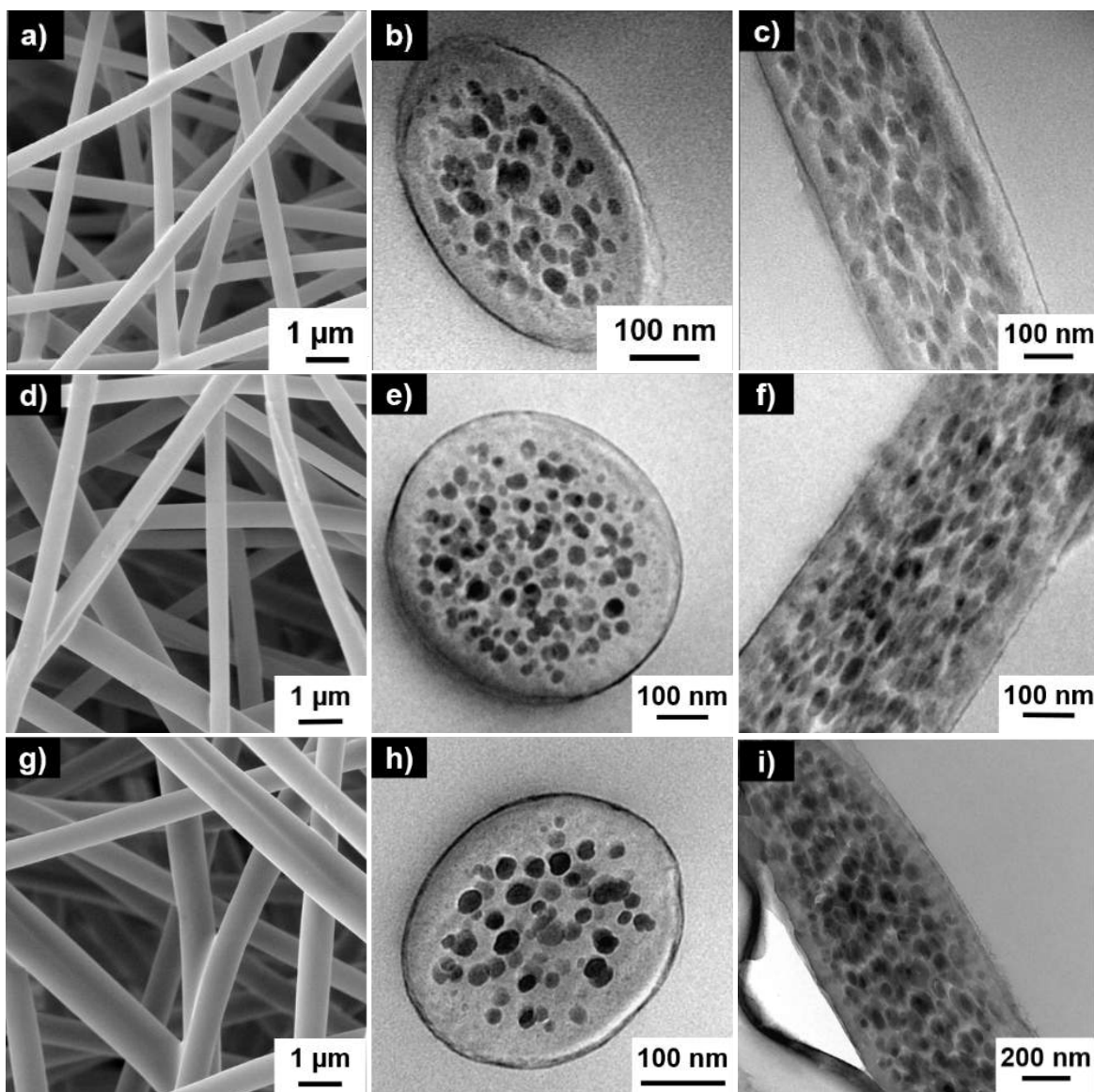


**Figure 5-1** SEM images and TEM images cross sectional and longitudinal cross section of various separator membranes. (a-c) 40wt% (d-f) 20wt% (g-i) 0wt%

Sample	Fiber Diameter (nm)	Porosity (%)	Pore Size Distribution (nm)	Electrolyte Uptake (%)
<b>0 wt% TEOS:PSZ</b>	660±81	82±4	619±76	801±75
<b>20 wt% TEOS:PSZ</b>	600±130	82±3	490±107	1066±24
<b>40 wt% TEOS:PSZ</b>	490±69	82±5	463±72	1109±32

**Table 5-3** Fiber diameter, porosity, pore size distribution and electrolyte uptake of various separator membranes

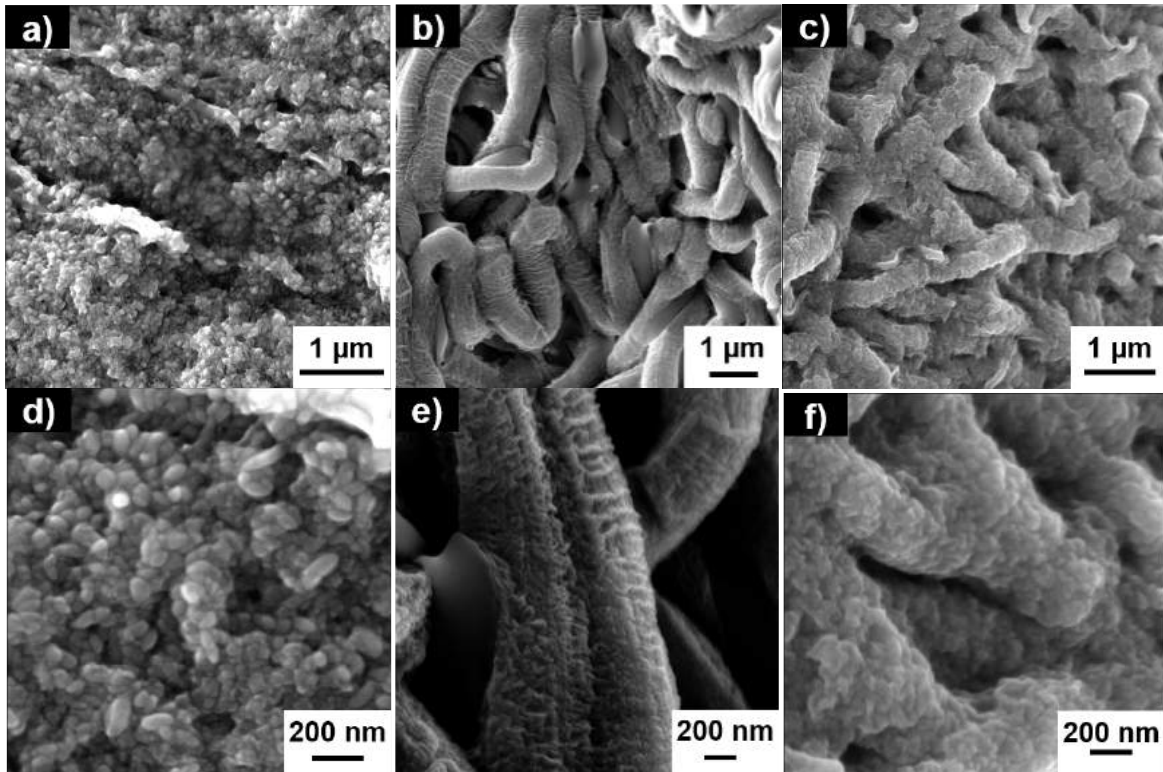


**Figure 5-2** SEM images of various membranes after removal of PAN using DMF rinse (a,d) 0wt%, (b,e) 20 wt%, (c,f) 40wt%

DSC measurements (Figure 5-3) were done to investigate how the presence of the ceramics affected the thermal properties of the polymer network. The cyclization temperature ( $T_c$ ) of the PAN polymer without the presence of ceramic is 290.1°C. The cyclization temperature of the PAN within the 0 wt% TEOS:PSZ fiber is 295°C indicating inclusion of 40 wt% TEOS:PSZ has a positive impact on the thermal stability of the fibers. Ceramic particles within the fiber acting as nanoparticle fillers within the fiber acting as an inhibiting agent, preventing the free radicals from getting to the other PAN polymer chains thus increasing the cyclization temperature.<sup>32,33</sup> On the other hand, there is a 13°C reduction in the  $T_c$  temperature for the 20 wt% TEOS:PSZ fiber, reducing  $T_c$  to 277°C. Cyclization first occurs within the amorphous region of the PAN fiber due to the loose orientation of the polymer chains before moving to the crystalline regions.<sup>34,35</sup> A decrease in the cyclization temperature in comparison to

the neat PAN fiber is a strong indication a larger disorganization of the polymer allowing for free radicals to better degrade the polymer chains. In addition, previous researchers have shown that the decrease in cyclization temperature and reduction in heat of enthalpy can also be caused by an outside initiator to nitrile cyclization. The reduction in the onset temperature is most likely caused by thermal degradation of the 20 wt% membrane, lending free radicals to the system to help propagate the thermal degradation of the polymer.

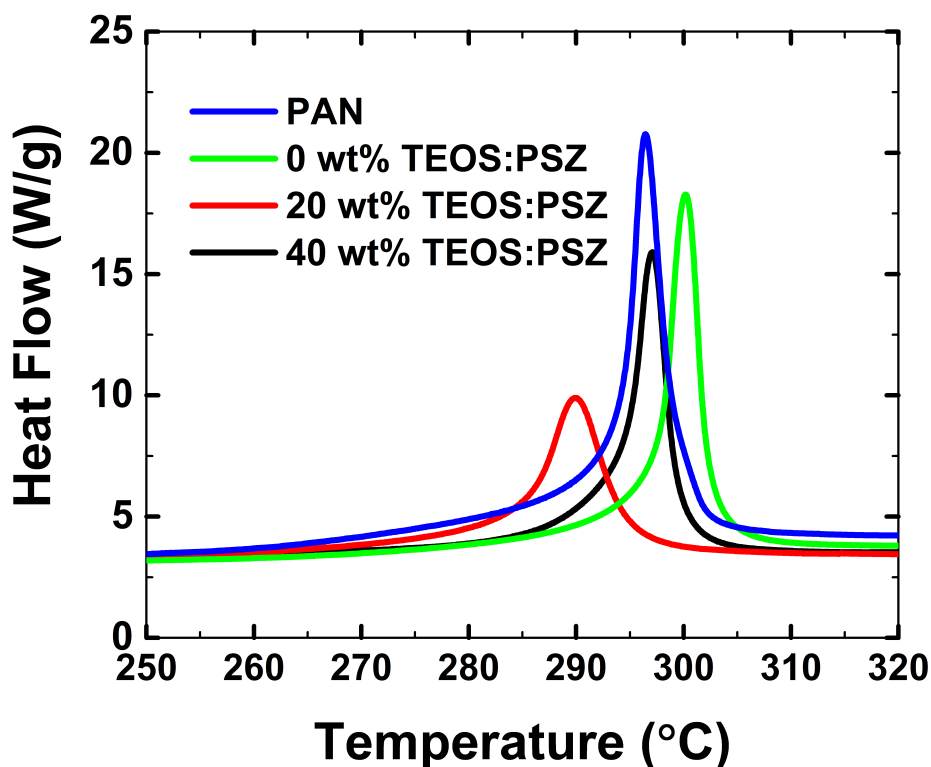
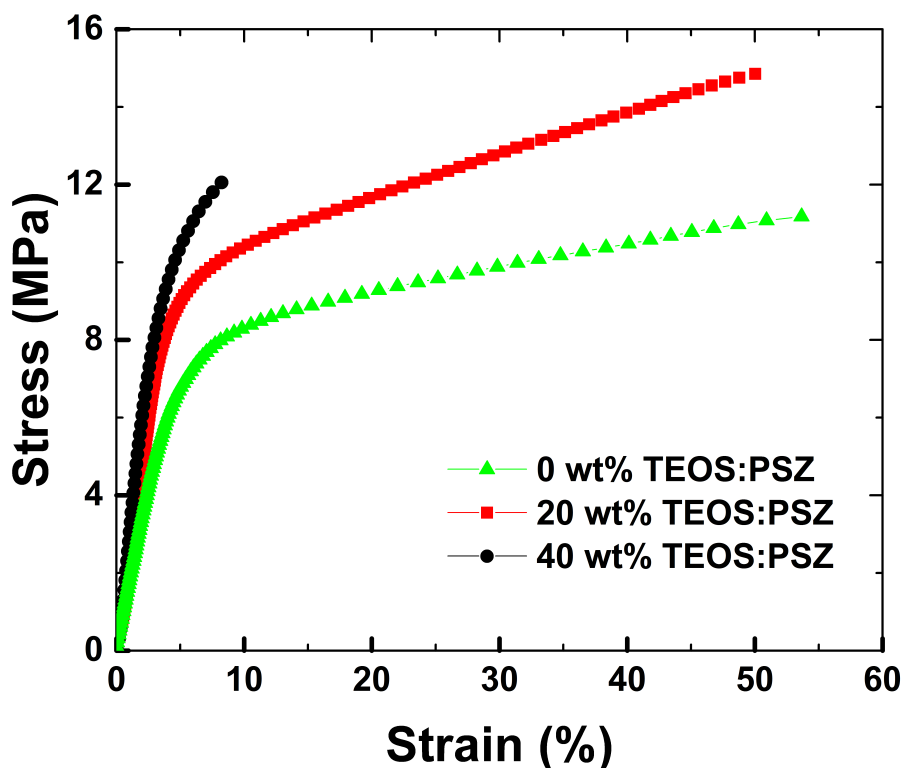


Figure 5-3 DSC thermograms of various separator membranes

In addition to good thermal property retention, separators must also be sufficient mechanical properties to withstand any punctures or tension the membranes might experience. Figure 5-4 shows the typical stress/strain curve of the three membranes. 20 wt% has the best highest strength at 14.8 MPa. This is followed by the 40wt% membrane which has a ultimate strength of 12.2 MPa. This membrane begins to exhibit brittle behavior due to the high ceramic

loading. It breaks at the yield point before entering the ductile region. The poorest performing membrane is 0 wt% TEOS:PSZ membrane strength at 11.2 MPa. These results suggest the interconnected ceramic network within the 40 wt% TEOS:PSZ and 20 wt% TEOS:PSZ offers added mechanical stability to the membranes.



**Figure 5-4** Typical stress-strain curves of various separator membranes

Figure 5-5 shows the XRD of various PAN/PDC membranes. Electrospun PAN membranes typically have peaks at  $17^\circ$  and  $28^\circ$ , indicating hexagonal packing of PAN chains.<sup>36,37</sup> 40 wt% TEOS:PSZ and 20 wt% TEOS:PSZ show a broadening of the peak of  $17^\circ$  which indicates a disruption in the crystalline structure and hence an increase in the amorphous regions. On the other hand, there is an increase in the crystalline regions and crystal size for the 0wt% TEOS:PSZ fibers compared to neat PAN polymer. This indicates that the ceramic domains in 0 WT% TEOS:PSZ fibers act as nucleating agents allowing for slight increase in crystallinity.

However, the interconnected ceramic network disrupts the crystallinity during the spinning process, leading to a reduction in crystallinity for the other fibers.

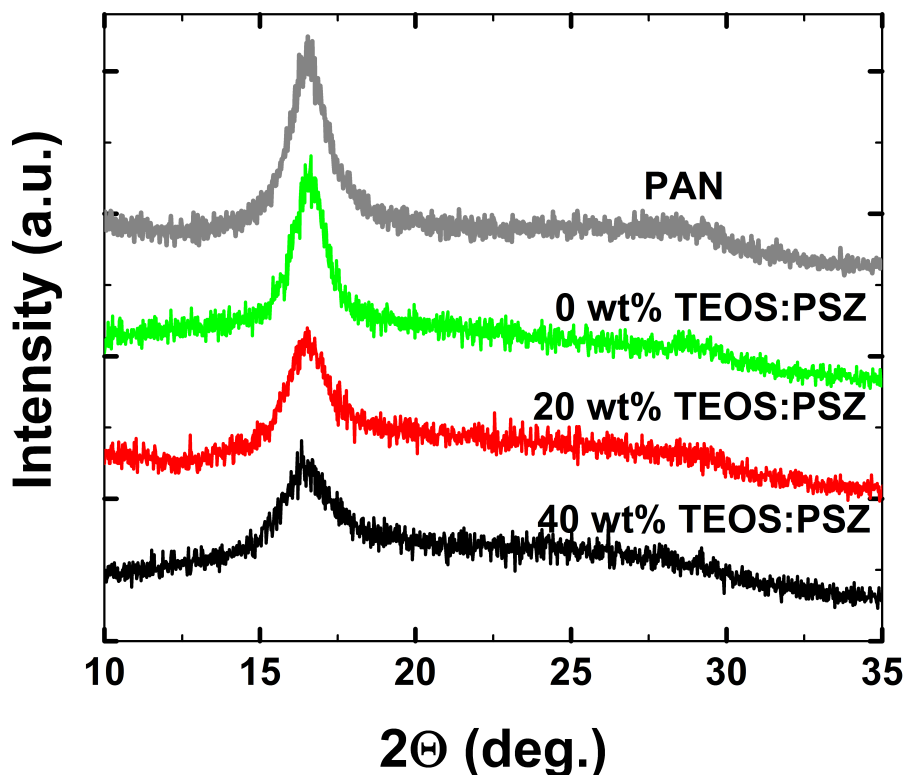


**Figure 5-5** XRD patterns of electrospun PAN/PDC composite membranes with various ceramic contents

Membranes are soaked in 1M LiPF<sub>6</sub>/DC/DMC/DEC to investigate the ability to uptake and retain electrolyte. The ability of the membrane separator to uptake electrolyte is vital in reducing the internal ionic resistance of the cell. Results in Table 5-3 show 40 wt% TEOS:PSZ sample has the highest electrolyte uptake with an uptake of 1189±32% followed by 20 wt% with an uptake of 1066±24%. This difference in uptake is due to the difference in amorphous regions in the two membranes. The 40 wt% TEOS:PSZ sample has a 21% crystallinity compared to 24% of the 20 wt% TEOS:PSZ sample. However there is a large decrease in uptake for the 0 wt% TEOS:PSZ membranes with an uptake value of 801±75%, this is due to the increased crystalline regions of 0 wt% TEOS:PSZ fibers compared to the other two membranes.

## Electrochemical Performance

The ionic conductivity of a li-ion separator represent with the transport of ions during the charge-discharge process of the batteries. The ionic conductivity of the three separators is presented in Figure 5-6. Ionic conductivity tests show 40 wt% TEOS:PSZ membranes have the highest calculated ionic conductivity at  $1.04\pm 0.05$  mS/cm followed by 20 wt% TEOS:PSZ with a ionic conductivity of  $0.59\pm 0.04$  mS/cm and 0 wt% TEOS:PSZ at  $0.44\pm 0.07$  mS/cm. Increase in ionic conductivity is usually attributed to increase in amorphous regions of the polymer due to inorganic inclusion, and ceramics acting as the Lewis acid–base center that promote salt disassociation which could free more cations.<sup>38</sup> In Figure 5-6, there is an indirect correlation between ionic conductivity and PAN polymer matrix crystallinity and crystal size confirming that the ceramic inclusion disrupts the polymer matrix to varying degrees thus increasing the ionic conductivity. The decrease in the degree of crystallization allows for the formation of more tunnels allowing for greater Li<sup>+</sup> migration. Electrolyte uptake results (Table 5-3) also show 0wt% has the lowest uptake compared to the other membranes due to have the larger pores sizes and fiber diameter. The reduced pore sizes of the other membranes allowed for a better entrapment of the electrolyte leading to improved ionic conductivity. In addition to the effect of the polymer, the ceramic sheath layer appears to have an impact on the ionic conductivity on the fibers.

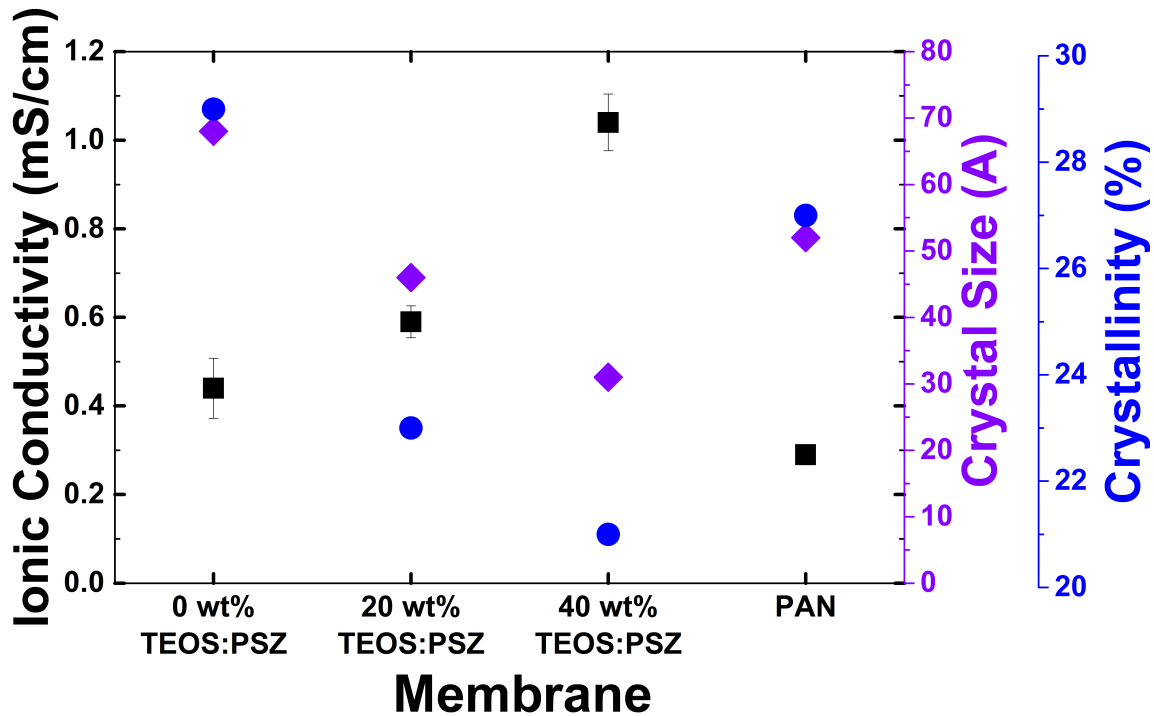


**Figure 5-6** Ionic conductivity of various membranes in relation to polymer crystal size and crystallinity

Figure 5-7 shows the cycling performance comparison of the three PAN/PDC separators at 0.2C and 0.5 C charging rates in  $\text{LiCoO}_2/\text{graphite}$  full cells in comparison to Celgard and PAN membranes. At the 0.2C charging rate, all PAN/ceramic separators start off at a similar initial capacity, approximately 134 mAh/g. Both the PAN and Celgard membranes start off at a lower capacity at 130 mAh/g. The higher initial capacity is due to the high ionic conductivity of the PAN/PDC membranes. After 100 cycles, the membrane with the highest ionic conductivity, 40 TEOS:PSZ has the highest capacity retention, 93% followed by 20 wt% TEOS:PSZ have a 91% capacity retention; 0 wt% TEOS:PSZ capacity has a 88% capacity retention after 100 cycles. A pure PAN membrane has a capacity retention of 86%. All electrospun membranes outperform the microporous membrane, Celgard, which showed an 82% retention for a 0.2C charge rate. The cells operated at a 0.5C charge rate show a similar trend to the cells operated at 0.2C rate, with 40 wt% TEOS:PSZ and 20 wt% TEOS:PSZ showing the best capacity retention. Starting

with an initial capacity of 121 mAh/g, the 40 wt% TEOS:PSZ is able to retain 90% of its initial discharge capacity, ending with final capacity of 109 mAh/g. The 20 wt% TEOS:PSZ separator was able to retain 87% retention, ending at 105 mAh/g after 100 cycles. Analogous to 0.2C case, 0 wt% TEOS:PSZ separator shows the fastest decay ending with 84% retention. The superior performance of the 20 wt% and 40 wt% membranes is due to their excellent electrolyte uptake and ionic conductivity in relation to the 0 wt% membrane and Celgard. The presence of Si-O-Si on the surface of the fiber can also enable greater salt disassociation of  $\text{LiPF}_6$ , producing a higher concentration of  $\text{Li}^+$  ions in the cell for the polymer/ceramic hybrid materials compared to the pristine PAN polymer and Celgard.

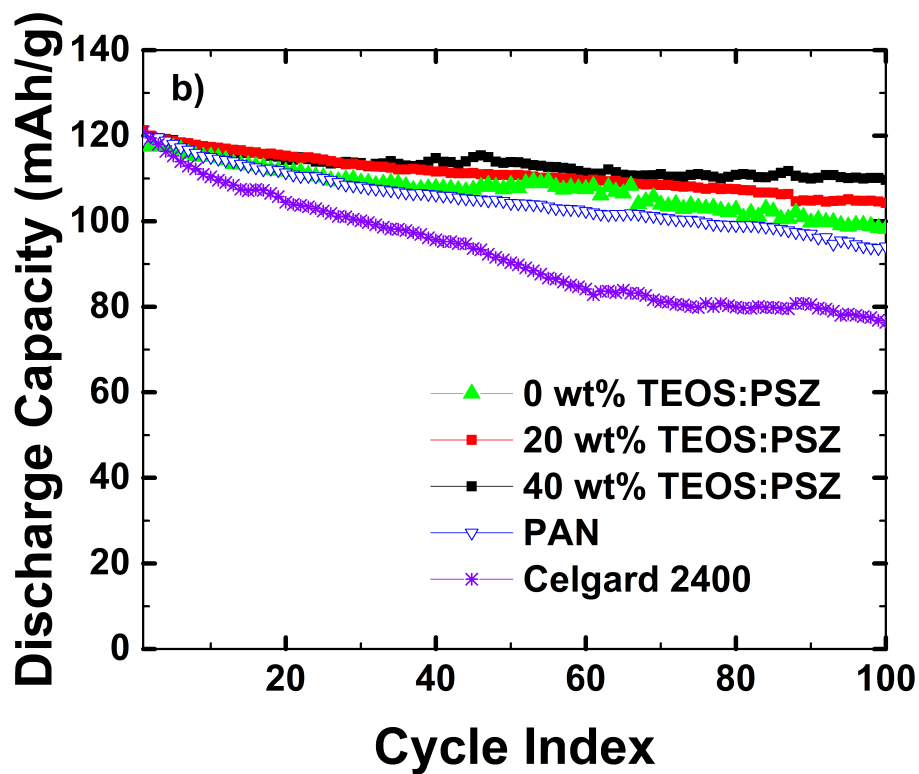
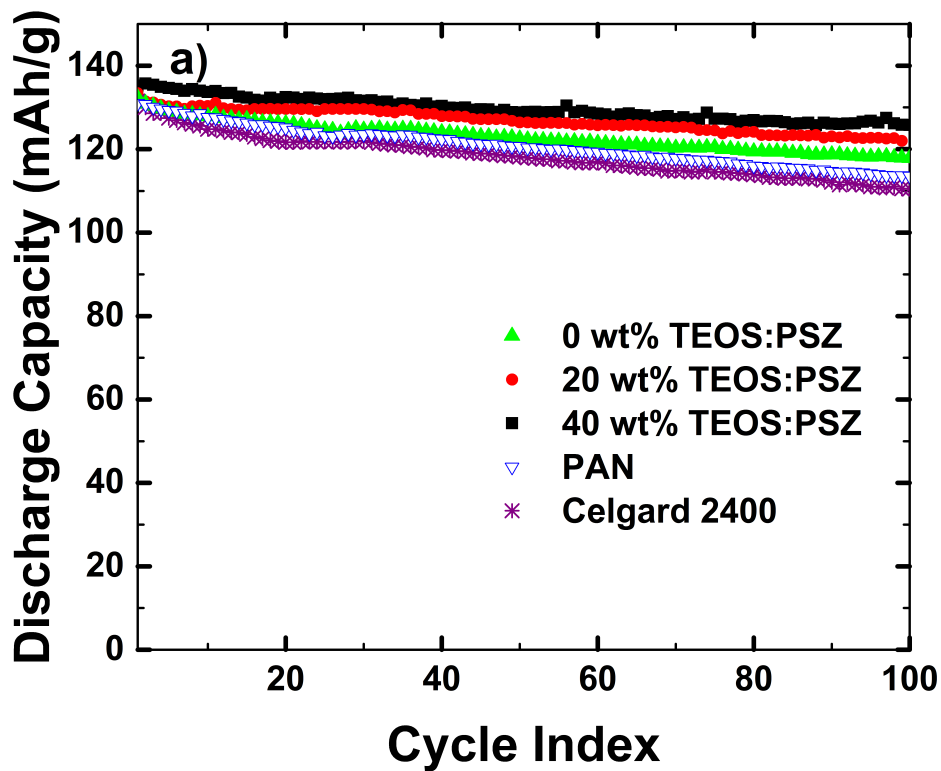


**Figure 5-7** The cycle performances of LiCoO<sub>2</sub>/graphite full cells with various separator membranes at a) 0.2C b) 0.5C

Rate capability testing for coin cells with the three separators can be seen in Figure 5-8. For the mild charge rates of 0.1C, all three separators show similar results. However as the cells are tested using more strenuous charging conditions, there is a more noticeable difference between the cells. At all charge rate after, the 40 wt% membrane shows the best capacity retention due to its superior ionic conductivity. At the most strenuous discharge capacity, 5C, the differences between the membranes becomes more apparent. Compared to the average C/10 discharge capacity, 132 mAh/g, there is a 55%, 44% and 33% retention at 5C for the 40 wt% TEOS:PSZ, 20 wt% TEOS:PSZ, and 0 wt% TEOS:PSZ membranes respectively. The Celgard membrane maintains 28% retention, underperforming compared to the other membranes. As the cells are returned to a C/10 discharging rate, all PAN/PDC membranes were able to recover a significant amount of their initial capacity. The PAN and the Celgard membranes also show poor recoverability when returned to a C/10 discharge rate. Celgard has a capacity recovery of 70%, while PAN shows a capacity recovery of 82%. However all PAN/PDC membranes show capacity recovery of greater than 95% due to the inclusion of ceramics into the polymer network.

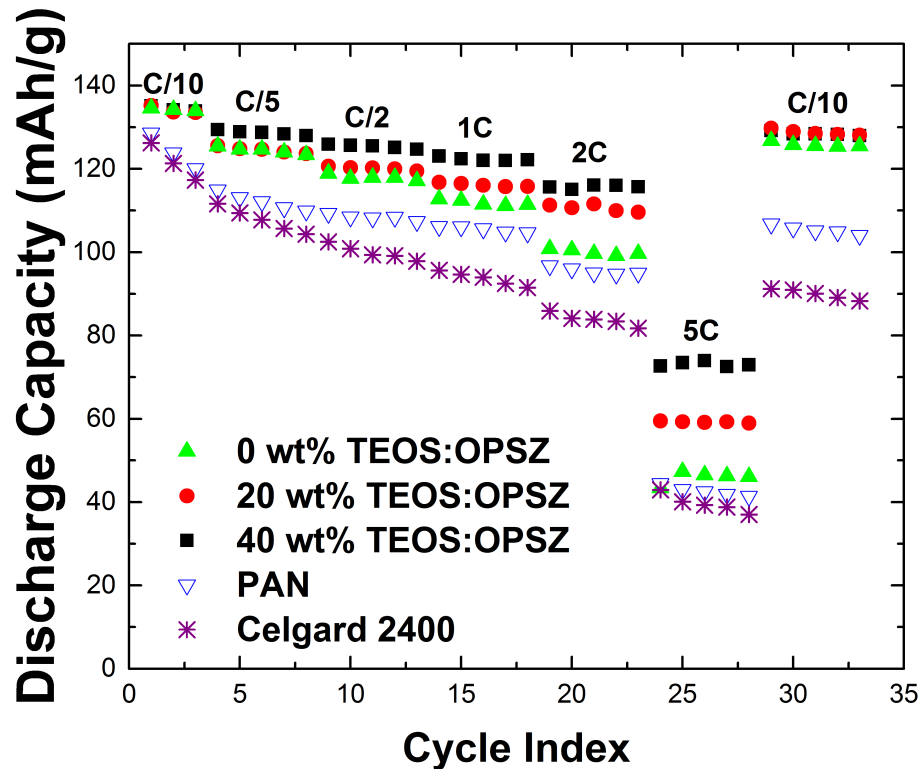


**Figure 5-8** Results of rate capability tests for the LiCoO<sub>2</sub>/graphite full cells with various separator membranes

#### 5.4 Conclusions

In this work, we created three different types of electrospun polycrylonitrile/polymer derived ceramic nanofibers using three different types of organopolysiloxazane precursors. The use of precursors allows for the creation of a polymer-ceramic bi-component in a single step process. The three precursors have a similar chemical backbone but differ on the ratio of the Si(OCH<sub>2</sub>CH<sub>3</sub>)<sub>3</sub> pendant chain attached to the polysilazane backbone. The presence of the Si(OCH<sub>2</sub>CH<sub>3</sub>)<sub>3</sub> chain enabled the ceramic to form an independently connected network within the polymer matrix. For the precursor without Si(OCH<sub>2</sub>CH<sub>3</sub>)<sub>3</sub> pendant chain, such a co-continuous polymer ceramic network was not formed, leading to discrete ceramic domains in the polymer matrix. The connected polymer network results in fiber membranes with superior mechanical and electrochemical performance compared to the membrane that had discrete ceramic domains in the polymer network.

## References

- 1 J.-M. Tarascon and M. Armand, *Nature*, 2001, **414**, 359.
- 2 F. L. Guangmin Zhou, *Energy Amp Environ. Sci.*, 2014, **7**, 1307.
- 3 B. Scrosati and J. Garche, *J. Power Sources*, 2010, **195**, 2419–2430.
- 4 P. Arora and Z. (John) Zhang, *Chem. Rev.*, 2004, **104**, 4419–4462.
- 5 X. Huang, *J. Solid State Electrochem.*, 2010, **15**, 649–662.
- 6 S. S. Zhang, *J. Power Sources*, 2007, **164**, 351–364.
- 7 K. Gao, X. Hu, C. Dai and T. Yi, *Mater. Sci. Eng. B*, 2006, **131**, 100–105.
- 8 Y.W. Ju, J.H. Park, H.R. Jung and W.-J. Lee, *Electrochimica Acta*, 2007, **52**, 4841–4847.
- 9 Y. Ding, W. Di, Y. Jiang, F. Xu, Z. Long, F. Ren and P. Zhang, *Ionics*, 2009, **15**, 731–734.
- 10 J. Hao, G. Lei, Z. Li, L. Wu, Q. Xiao and L. Wang, *J. Membr. Sci.*, 2013, **428**, 11–16.
- 11 H.-R. Jung, D.-H. Ju, W.-J. Lee and X. Zhang, *Electrochimica Acta*, 2009, **54**, 3630–3637.
- 12 T.-H. Cho, M. Tanaka, H. Onishi, Y. Kondo, T. Nakamura, H. Yamazaki, S. Tanase and T. Sakai, *J. Power Sources*, 2008, **181**, 155–160.
- 13 Y. Liang, S. Cheng, J. Zhao, C. Zhang, S. Sun, N. Zhou, Y. Qiu and X. Zhang, *J. Power Sources*, 2013, **240**, 204–211.
- 14 W.K. Shin, Y.S. Lee and D.-W. Kim, *J. Nanosci. Nanotechnol.*, 2013, **13**, 3705–3710.
- 15 H. Wang, H. Li, L. Yu, Y. Jiang and K. Wang, *J. Appl. Polym. Sci.*, 2013, **130**, 2886–2890.
- 16 H-S. Jeong, S. C. Hong and S.Y. Lee, *J. Membr. Sci.*, 2010, **364**, 177–182.
- 17 H. Liu, J. Xu, B. Guo and X. He, *Ceram. Int.*, 2014, **40**, 14105–14110.
- 18 T. Lee, W.-K. Kim, Y. Lee, M.-H. Ryou and Y. M. Lee, *Macromol. Res.*, 2014, **22**, 1190–1195.
- 19 H. Liu, J. Xu, B. Guo and X. He, *J. Appl. Polym. Sci.*, 2014, **131**, n/a–n/a.
- 20 J.-H. Park, J.-H. Cho, W. Park, D. Ryoo, S.-J. Yoon, J. H. Kim, Y. U. Jeong and S.-Y. Lee, *J. Power Sources*, 2010, **195**, 8306–8310.
- 21 M. Yanilmaz, C. Chen and X. Zhang, *J. Polym. Sci. Part B Polym. Phys.*, 2013, **51**, 1719–1726.
- 22 M. Yanilmaz, M. Dirican and X. Zhang, *Electrochimica Acta*, 2014, **133**, 501–508.
- 23 M. Yanilmaz, Y. Lu, Y. Li and X. Zhang, *J. Power Sources*, 2015, **273**, 1114–1119.

- 24 Y. Zhai, K. Xiao, J. Yu and B. Ding, *Electrochimica Acta*, 2015, **154**, 219–226.
- 25 J.A. Choi, S. H. Kim and D.-W. Kim, *J. Power Sources*, 2010, **195**, 6192–6196.
- 26 A. Manuel Stephan and K. S. Nahm, *Polymer*, 2006, **47**, 5952–5964.
- 27 M.Y. An, H.T. Kim and D.-R. Chang, *J. Solid State Electrochem.*, 2014, **18**, 1807–1814.
- 28 X. Huang, *J. Power Sources*, 2011, **196**, 8125–8128.
- 29 H. T. Chiu, T. Sukachonmakul, M. T. Kuo, Y. H. Wang and K. Wattanakul, *Appl. Surf. Sci.*, 2014, **292**, 928–936.
- 30 R. Saito, Y. Fujii and T. Kumagai, *J. Appl. Polym. Sci.*, 2013, **127**, 2074–2081.
- 31 S. Smith, .
- 32 L. Ji and X. Zhang, *Mater. Lett.*, 2008, **62**, 2161–2164.
- 33 L. Ji, K.-H. Jung, A. J. Medford and X. Zhang, *J. Mater. Chem.*, 2009, **19**, 4992–4997.
- 34 A. Gupta and I. R. Harrison, *Carbon*, 1996, **34**, 1427–1445.
- 35 Y. Hou, T. Sun, H. Wang and D. Wu, *J. Appl. Polym. Sci.*, 2009, **114**, 3668–3672.
- 36 S. W. Choi, J. R. Kim, S. M. Jo and W. S. Lee, *J. Electrochem. Soc.*, 2005, **152**, A989–A995.
- 37 Z. Song, X. Hou, L. Zhang and S. Wu, *Materials*, 2011, **4**, 621–632.
- 38 N. Salem and Y. Abu-Lebdeh, in *Nanotechnology for Lithium-Ion Batteries*, eds. Y. Abu-Lebdeh and I. Davidson, Springer US, 2012, pp. 221–244.

## **Chapter 6 Effect of Ceramic Morphology on the Properties of Bi-Component Polyacrylonitrile/Polymer-Derived Ceramic Nanofibers for the use as Separator Membranes in Lithium-ion Batteries**

### **Abstract**

Various liquid siloxane precursors were incorporated into polyacrylonitrile (OAN) to make polymer/ceramic hybrid nanofibers using the electrospinning process. In this work we aim to show incorporating a ceramic layer on the surface of fiber has a significant impact on the membrane-electrolyte interaction. All membranes created consisted of 3D interconnected porous membrane with randomly oriented, well-formed fibers free of beads. Organopolysilazane (OPSZ) and methylsilsesquioxane (MSQ) precursors resulted in composite fibers with ceramic not only distributed inside the fiber but the ceramic also forms a sheath layer on the surface of the fiber. PAN/Methylsiloxane (MSX) membranes contained inhomogeneous distributed ceramic within the polymer with fragmented ceramic particles on the fiber surface. PAN/Polysilsesquioxane (PSSQ) membranes contain only ceramic within the polymer matrix. The difference in polymer distribution had a significant impact on the mechanical stability and electrochemical performance of the membranes. The presence of ceramic on the surface resulted in an increase in the ionic conductivity due to more favorable membrane-electrolyte interaction. Lithium cobalt oxide/graphite full cells made with the various separators showed the membranes with a full sheath layer have higher cell capacities and superior capacity retention at both a 0.2C and 0.5C charge rate after 100 cycles. Post mortem analysis reveals that the ceramic on the fiber surface can scavenge hydrogen fluoride present in the system, leading to improved capacity retention.

## 6.1 Introduction

As the use of portable devices and electronic vehicles continue to rise, so does the demand for more powerful and efficient secondary batteries to power them. The most widely used secondary battery over the last two decades has been lithium ion batteries due to their high energy density and excellent cycle life.[1] Within the lithium battery, separators serve as a physical barrier between the cathode and anode in order to prevent short-circuiting while still maintain ionic transport. Polyolefin separators currently dominate the separator market because of their excellent mechanical strength and chemical stability.[2,3] However the use of nonpolar polyolefins, typically polyethylene (PE) or polypropylene (PP) lead to poor affinity for organic electrolytes and low thermal stability.[4,5] In addition the semicrystalline nature of polyolefin, limits the porosity of the membranes to 40-55 percent. These properties lead to notable resistance within the cell, severely affecting the cell cycle life and stability.[6]

Nonwovens have gained interest in the last decade as a means of creating higher porosity membranes from more hydrophilic materials. Non-woven membranes can be created from a variety of methods such as papermaking method [7], solution extrusion method [8,9] and electrospinning [10,11]. Electrospinning has gained considerable attention for the ease for making non-woven membrane with a 3-D interconnected pore structure with high porosity and large surface area. Electrospinning can be used to make membranes from a variety of materials including polyimide (PI) [12,13], polyacrylonitrile (PAN) [14,15], poly(vinylidene fluoride) (PVDF) [4,16], etc. The use of less hydrophobic materials allowed for better membrane-electrolyte interaction leading to increase electrolyte uptake and retention. The use of an electrospun membrane by Hao et al. [17] saw a 500% electrolyte uptake, more than 3 times the electrolyte uptake usually reported for polyolefin membranes. The increase in porosity and

electrolyte uptake lead to increases in ionic conductivity and superior electrochemical performance.

The use of electrospun polymer composite containing inorganics have gained attention for their use in various sectors for their properties due to ability to the beneficial properties of the organic and inorganic components. [18] In the past decade, there has been a large increase in their use in separators for lithium ion batteries. Researchers have incorporated metal oxides such as, SiO<sub>2</sub> [19], Al<sub>2</sub>O<sub>3</sub> [20], and TiO<sub>2</sub> [21] as a way of improving the thermal and electrochemical performance of lithium ion batteries. Separator incorporating these metal oxides exhibited superior thermal, mechanical and electrochemical properties. The use of ceramics improved the ionic conductivity, lower interfacial resistances and superior C-rate performance compared to neat electrospun membrane and microporous polyolefin membrane.

In this work, we will incorporate four different types of ceramic precursors into PAN polymer to investigate the effect of ceramic morphology on the electrochemical performance on lithium ion batteries. All membranes utilized the electrospinning technique to create bi-component polymer/ceramic nanofibers. Depending on the precursor used there is difference in the morphology of the ceramic component. For this work we chose to use four different precursors that would result in Si-O-Si based ceramics upon curing. Organopolysilazane (OPSZ) is a clear, colorless, low viscosity liquid resin consisting of polymethyl(hydro)silazane linear polymeric subunit with a TEOS pendant chain. OPSZ can undergo a hydrolysis/condensation process by reacting with moisture in the atmosphere. The resin will cure both along the Si-H and Si-N bonds as well as along the TEOS pendant pain to create Si-O-Si bonds.[22] Methylsilsesquioxane (MSQ) is a spin-on glass resin with the chemical formula [RSiO<sub>3/2</sub>]<sub>n</sub>, it's a siloxane network with one non-reactive methyl group per Si atom.[23] The silanol groups can

react with each other to form a highly crosslinked structure through inter or intramolecular condensation reacts. Methylsiloxane (MSX) is a spin-on glass that can also crosslink through the silanol groups present on the resin backbone. Polysilsesquioxane (PSSQ) is a solid with molecules having a three dimensional cage structure. PSSQ solids are easily soluble in most organic solvents and easily disperse in most polymer matrices. We aim to show that the presence of ceramic precursor on the surface has a great impact on the ionic conductivity and hence the cycle performance on lithium ion full cells.

## 6.2 Experimental

### 6.2.1 Membrane Preparation

The PAN/ceramic non-woven separator was prepared using the electrospinning method. The electrospinning solution was prepared by combining Polyacrylonitrile (PAN,  $M_w = 200,000$ , Polysciences) with N,N-Dimethylformamide (DMF) to form a 8wt% solution. The solution was stirred for 8 hours on a 60°C hot plate to thoroughly dissolve the polymer. The liquid ceramic precursors: organopolysilazanes (EMD Performance Materials), methylsilsesquioxane (Nepes Corporation), methylsiloxane (Nepes Corporation), polysilsesquioxane (Dongjin SemiChem Ltd.), were added to obtain 10 wt% ceramic in relation to PAN. The mixtures were stirred on a hot plate for 10 minutes to ensure the components are properly mixed. Spinning conditions for each solution is listed in Table 6-1.

Precursor	Feed rate (mL/hr)	Voltage (KV)	Distance (cm)
OPSZ	0.9	17.5	15
MSQ	1.8	15	16
MSX	2.4	16	16
PSSQ	0.9	17.5	20

**Table 6-1** Electrospinning conditions for various separator membranes

### 6.2.2 Membrane Characterization

The presence of ceramic elements in the final fiber was determined using Fourier transform infrared spectroscopy (FTIR) under ambient conditions within the range of 700 – 4000  $\text{cm}^{-1}$  with a resolution of 4  $\text{cm}^{-1}$  for 512 scans. Fiber morphology and diameter were examined using scanning electron microscopy (Tecsca Mira3 Field Emission SEM) with an accelerating voltage of 5KV. The average fiber diameters were determined by choosing 50 randomly selected fibers using Image J. The internal morphology of the fibers was investigated by transmission electron microscopy (FEI Tecnai G2 T12 Spirit TEM STEM). Mechanical stability was tested by Dynamic Mechanical Analysis (TA Instruments DMA Q800 Dynamic Mechanical Thermal Analysis (DMTA). The separator/electrolyte interaction was estimated by measuring the dynamic change in contact angle between the electrolyte and the separator using a high speed camera capturing images every 0.001 sec. Electrolyte uptake is calculated using the following relation:

$$Uptake (\%) = \frac{M_a - M_i}{M_i} \times 100 \quad (1)$$

where  $M_a$  and  $M_i$  are the masses of the wet and dry membrane respectively. The porosity ( $P$ ) of the fabricated membranes was calculated by using the measured data and the density of material with the equation below.

$$P = 1 - \left( \frac{W}{\rho \cdot V} \right) \quad (2)$$

where  $W$  is the dried membrane weight,  $\rho$  the membrane density, and  $V$  the apparent volume of the membrane. The membrane thickness was measured by a digital thickness gauge.

### 2.3 Membrane Electrochemical Evaluation

Electrochemical test are carried out in a 2302 coin cell. Cell impedance was measured by sandwiching the separator membrane between two lithium disks inside a cell. The cells were tested on a PARSTAT 4000 (Princeton Applied Research), with the impedance measurements at an amplitude of 5 mV over a frequency range of 20000 kHz to 1 Hz.

Full cell consisted of a  $\text{LiCoO}_2$  cathode (LG Chem), a graphite anode (MTI Corporation), and  $\text{LiPF}_6\text{-EC/DMC/DEC}$ ; cycling was carried out at a voltage range between 2.5 – 4.2 V at 0.2C and 0.5 C charge and discharge rates.

## 6.3 Results and Discussion

FTIR analysis (Figure 6-1) of the various membranes shows the ceramics are well incorporated into the polymer membrane. All membranes show the presence of Si-O-Si asymmetrical stretching between  $1037\text{ cm}^{-1}$  to  $1134\text{ cm}^{-1}$ , depending on the angle of the Si-O bond within the ceramic structure. The peak at  $1134\text{ cm}^{-1}$  for the PSSQ based ceramic is associated with the stretch band of Si-O bond in a caged structure at approximately  $150^\circ$ . The peak Si-O for MSQ and MSX are present at  $1070$ , characteristic of Si-O asymmetric stretching network. The Si-O stretch in OPSZ is seen at  $1037\text{ cm}^{-1}$  which indicates the angle between Si-O is less than that of Si-O bonds in the previously mentioned ceramics.

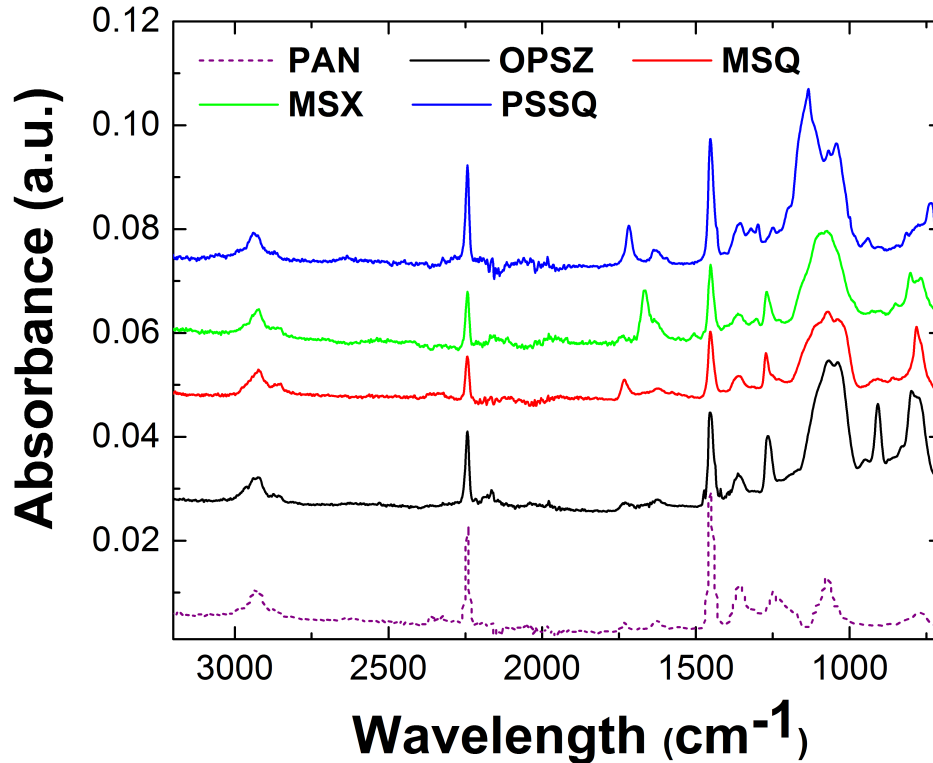


**Figure 6-1** FTIR of various PAN/ceramic membranes

SEM images of the fiber membrane (Figure 6-2) reveal 3D interconnected porous membrane with randomly oriented, uniform, well-formed fibers free of beads. Fiber characteristics including diameter and porosity are listed in Table 2. The MSQ and MSX precursors are both only 12 percent ceramic, therefore a lot of precursor liquid has to be added to the 8 wt% PAN solution. The addition of large amount of liquid decreases the viscosity of the solution reducing the diameter of the final fibers. The OPSZ and PSSQ liquids are both 100 percent precursors; therefore these solutions are less diluted resulting in slightly thicker fibers. Though the OPSZ fibers have the largest fiber diameter, it has the smallest pore size distribution and the highest porosity. The remaining membranes have a similar average porosity.

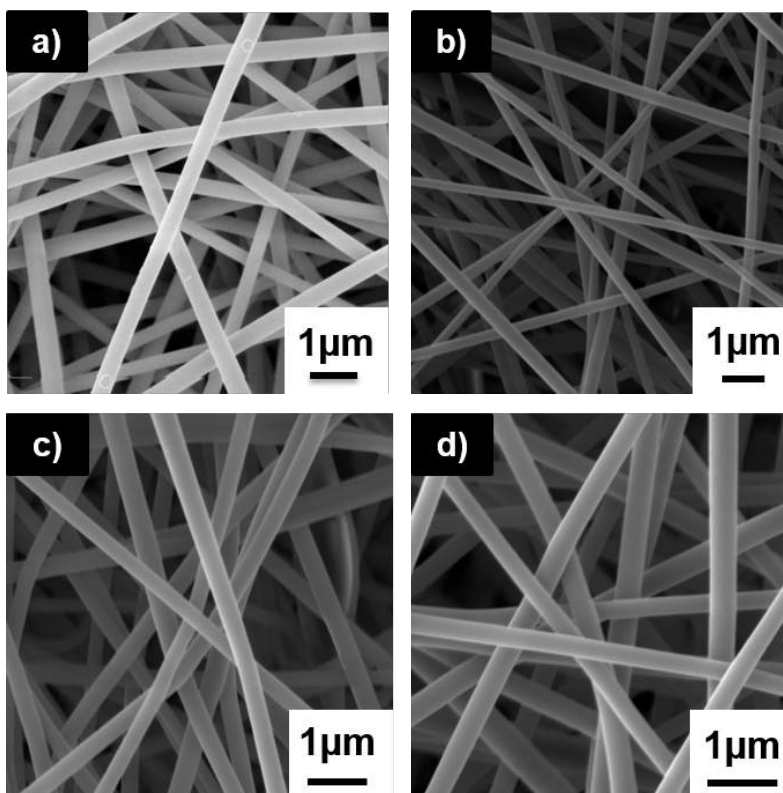


**Figure 6-2** SEM images of various PAN/Ceramic membranes. a) OPSZ b) MSQ c) MSX d) PSSQ

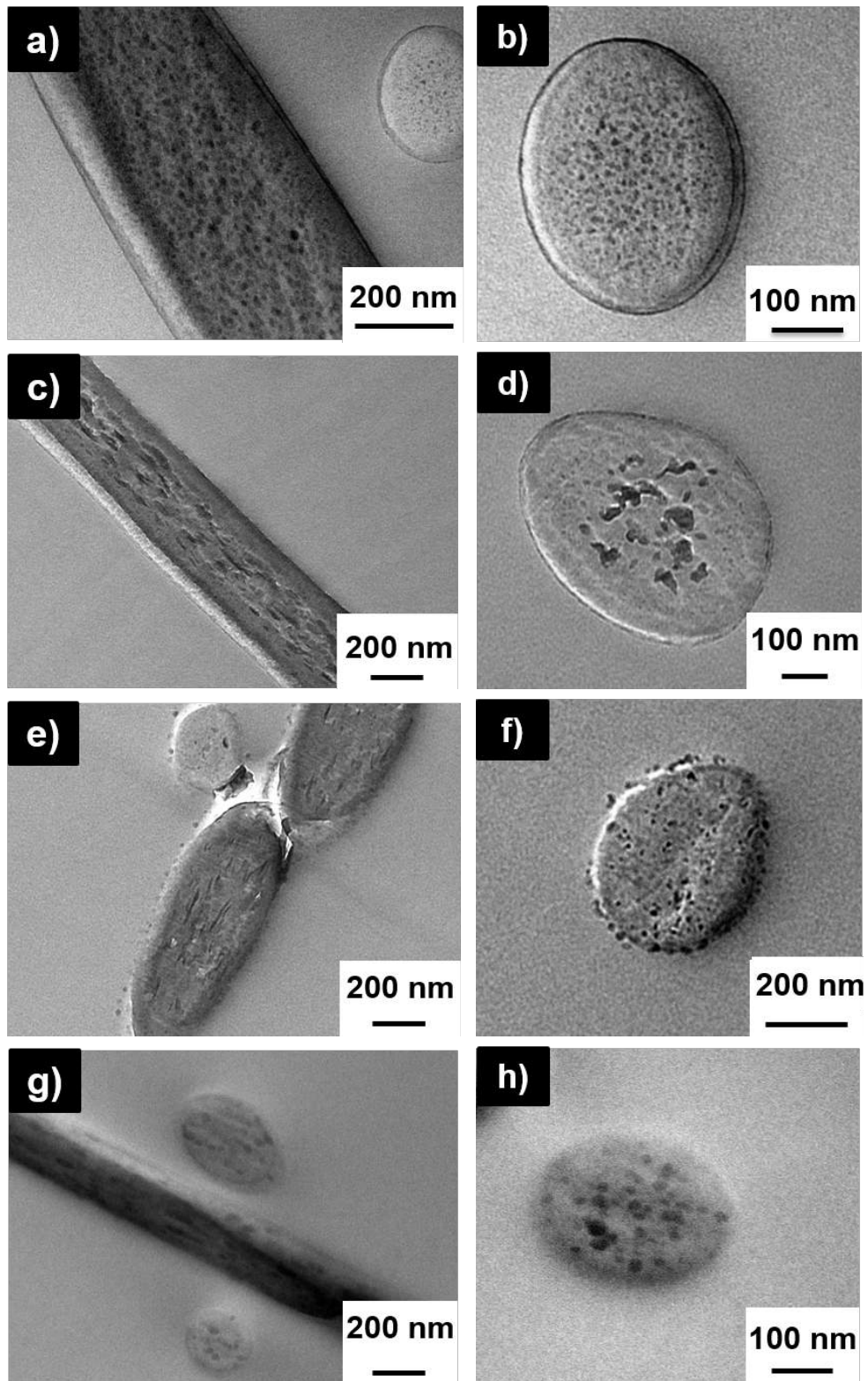
Membrane	Average Pore Size (nm)	Fiber Size (nm)	Porosity	Fiber Crystallinity (%)
OPSZ	205±94	367±75	79±3	29
MSQ	350±71	292±46	76±4	36
MSX	262±88	298±98	75±3	31
PSSQ	246±76	316±36	75±4	39

**Table 6-2** Characteristics of PAN/PDC composite separators of various PDC inclusions

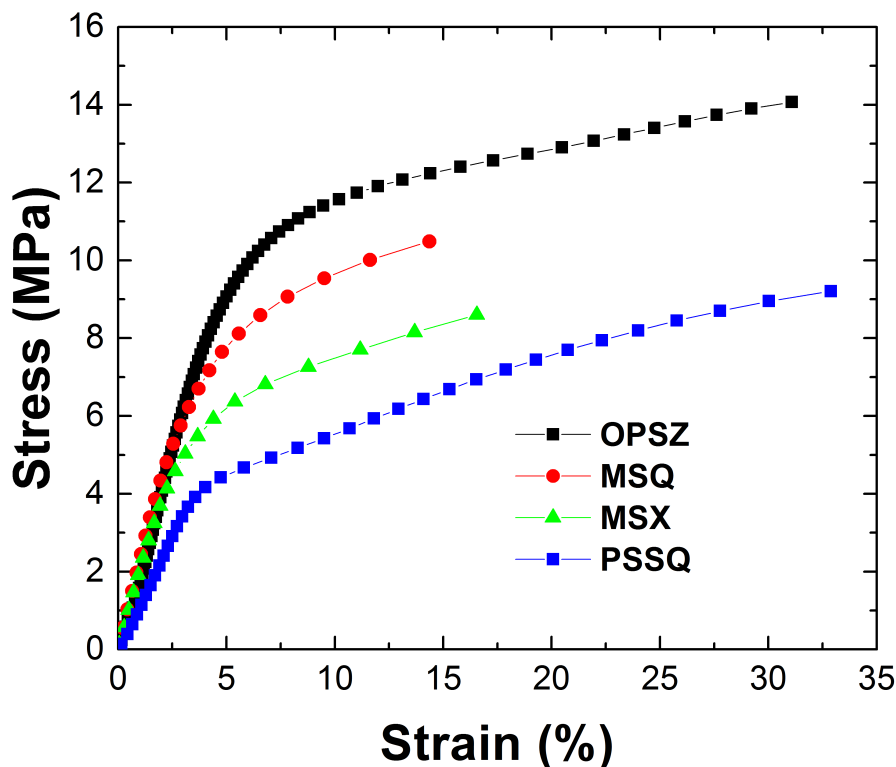
TEM of the radial and longitudinal cross-sections were done to investigate the domain distribution within the fibers. TEM images of the cross section reveal each precursor resulted in a different distribution of the ceramic within the fiber. OPSZ precursor (Figure 6-3a-b) forms small ceramic domains with average diameter of 10nm evenly dispersed along the fiber axis. Radial cross sections reveal the ceramic also forms a thin sheath layer ( $\sim 4.3 \pm 0.3$ nm) around each

fiber similar to results seen in previous works. The MSQ precursor (Figure 6-3c-d) leads to irregularly shaped elongated domains along the fiber axis. Unlike the OPSZ fiber, which produced uniform domains, there are a wide variety of domain shape and sizes formed by the MSQ precursors. Radial cross section shows the domains for the MSQ fiber tend to form toward the center of the fiber. Similar to OPSZ, MSQ also has a thin sheath layer ( $4.2\pm 0.6\text{nm}$ ) around the individual fibers. Both radial and longitudinal cross sections reveal the MSX based ceramic forms a disjointed ceramic layer on the fibers surface. Along the fiber axis, the fibers have long, thin domains that are sporadically placed leading to an inhomogeneous fiber internal morphology. PSSQ fibers have no ceramic on the surface of the fibers, instead all the ceramic components are concentrated inside the fiber. As you can see in Figure 6-3g, the distribution of the fibers is even and various cross section morphologies will have different layouts.

Mechanical stability is an important characteristic of all separator membranes to withstand tension from winding. Of the four membranes tested, OPSZ has the highest mechanical stability which a strength of 14MPa. The following membranes had strengths of 10.5 MPa, 8.6 MPa, and 9.8MPa for MSQ, MSX, and PSSQ respectively. The superior mechanical stability of OPSZ fibers is due to uniform distribution of the particles within the fiber. The dispersion of small OPSZ nanofillers improves the mechanical properties by adding interfacial strength between the polymer network and the OPSZ. However, the large size of the MSQ and their concentration to only the center of the fiber adds sources of stress within the fiber leading to its reduced strength and ductility compared to OPSZ. MSX and PSSQ membranes inhomogeneous particle distribution within the polymer also impact their ability to act as a suitable nanofiller.

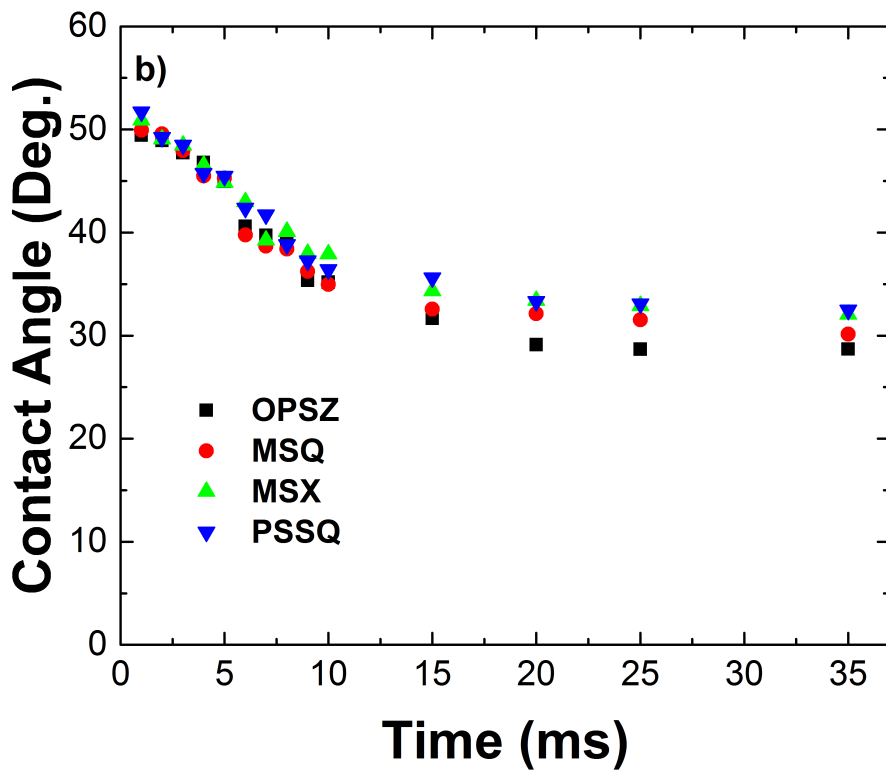
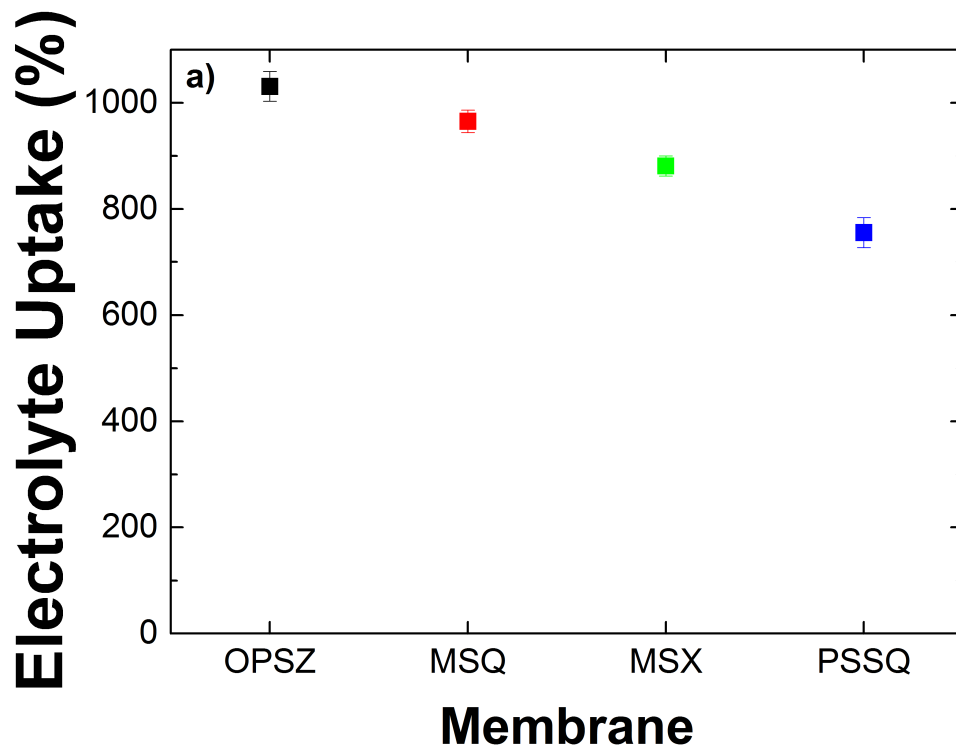


**Figure 6-3** TEM images revealing the internal morphology of the PAN/ceramic fibers. a-b) PAN/OPSZ c-d) PAN/MSQ e-f) PAN/MSX g-h) PAN/PSSQ



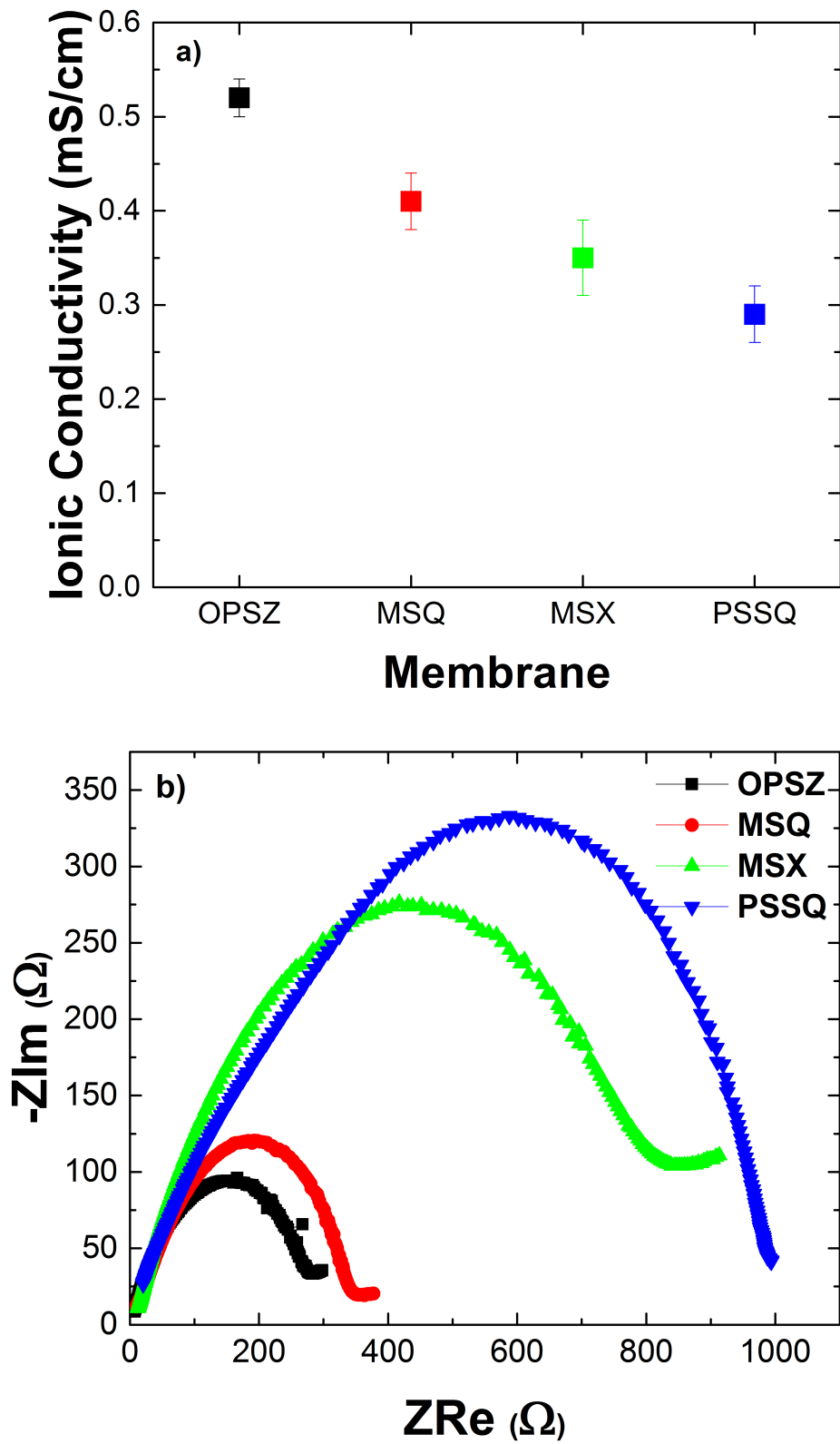
**Figure 6-4** Stress-Strain curves of the four membranes

The electrolyte uptake of separators is important because it can affect the internal resistance within the cell as well as the ionic conductivity. The electrolyte uptake is dependent on a variety of factors including average fiber diameter, pore size and membrane porosity. The OPSZ membrane has the highest electrolyte uptake at  $1031 \pm 28\%$ ; the MSQ membrane also has a large uptake of  $982 \pm 25\%$ . This large uptake percentage is due to the swelling of the amorphous regions of the PAN polymer as well as more favorable electrolyte membrane surface interaction and increased porosity. The more favorable interaction is exemplified in dynamic contact angle measurements present in Figure 6-5b. The electrolyte is able to penetrate faster into the membrane due to the presence of the sheath layer. The disjointed ceramic covering on the PAN/MSX fibers affects its membrane surface-electrolyte interaction and electrolyte uptake. PSSQ has the smallest uptake due to the lack of a sheath layer and having the highest percent crystallinity of the four membranes.



**Figure 6-5** a) Electrolyte uptake of various separator membranes b) Contact angle between separator membranes and electrolyte

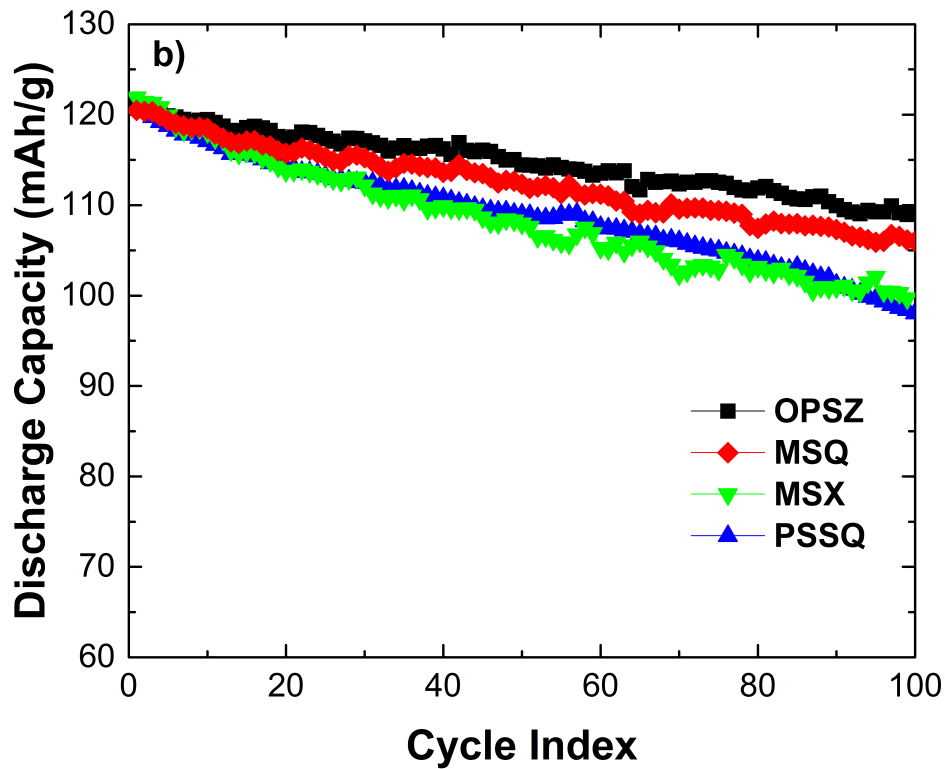
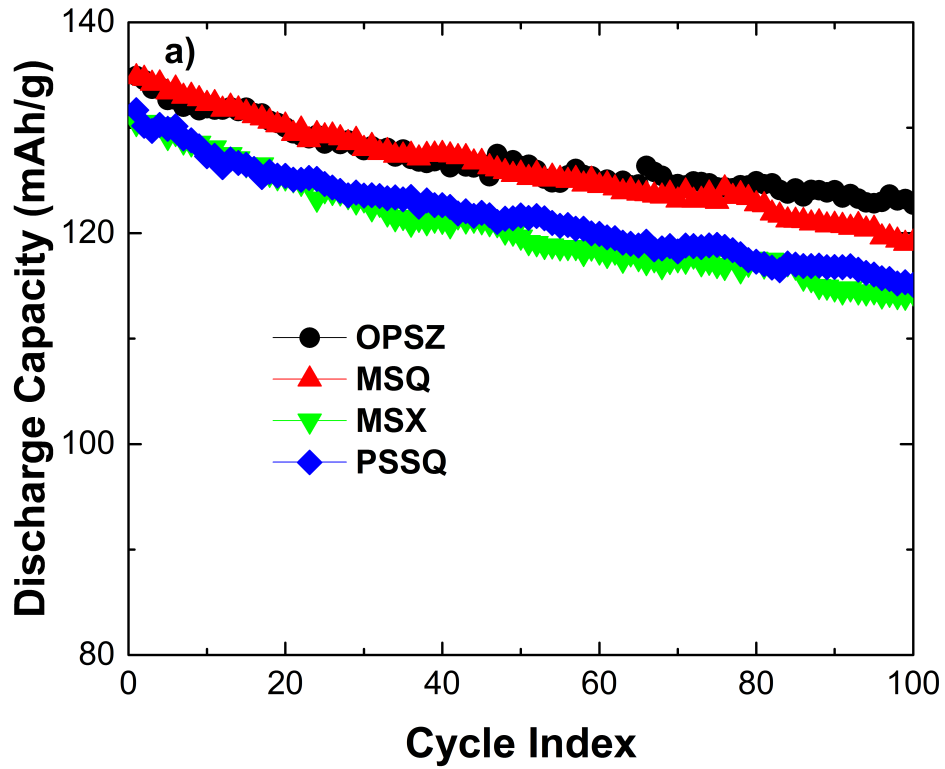
Ionic conductivity is dependent on various factors such as pore structure, porosity, thickness of the membrane, electrolyte uptake and resistivity to the electrolyte.[24,25] The room-temperature ionic conductivity of the various membranes are presented in Figure 6. Results show OPSZ membranes have the highest ionic conductivity at  $0.52\pm 0.02$  mS/cm, followed by MSQ at  $0.42\pm 0.03$  mS/cm. MSX and PSSQ have calculated ionic conductivity values of  $0.34\pm 0.04$  mS/cm and 0.29 mS/cm respectively. The increase in ionic conductivity of the MSQ and OPSZ membranes can be attributed to the Si-O-Si linkages on the surface of the fiber having Lewis acid/base reactions with the ionic species in the electrolyte.[26] Moreover, referring to Table 6-2, the OPSZ membrane has the highest porosity among the membranes, along with the smallest and most uniform pore sizes. The remaining separators all have similar porosity of approximately 75 percent. The high porosity of OPSZ membranes as well as its high electrolyte uptake leads to its superior ionic conductivity. In addition, Nyquist plots of lithium symmetrical cells show OPSZ and MSQ fibers have the lowest interfacial resistance represented by the diameter of the semi-circle of the plot. This reduction in resistance is due to the presence of the sheath layer on the fibers providing better membrane-electrode affinity which facilitates the migration of lithium ion at the interface between the electrolyte and electrode which leads to a decrease in cell resistance. The membranes without a full sheath layer, MSX and PSSQ, show interfacial resistance double and triple that of the other membranes.



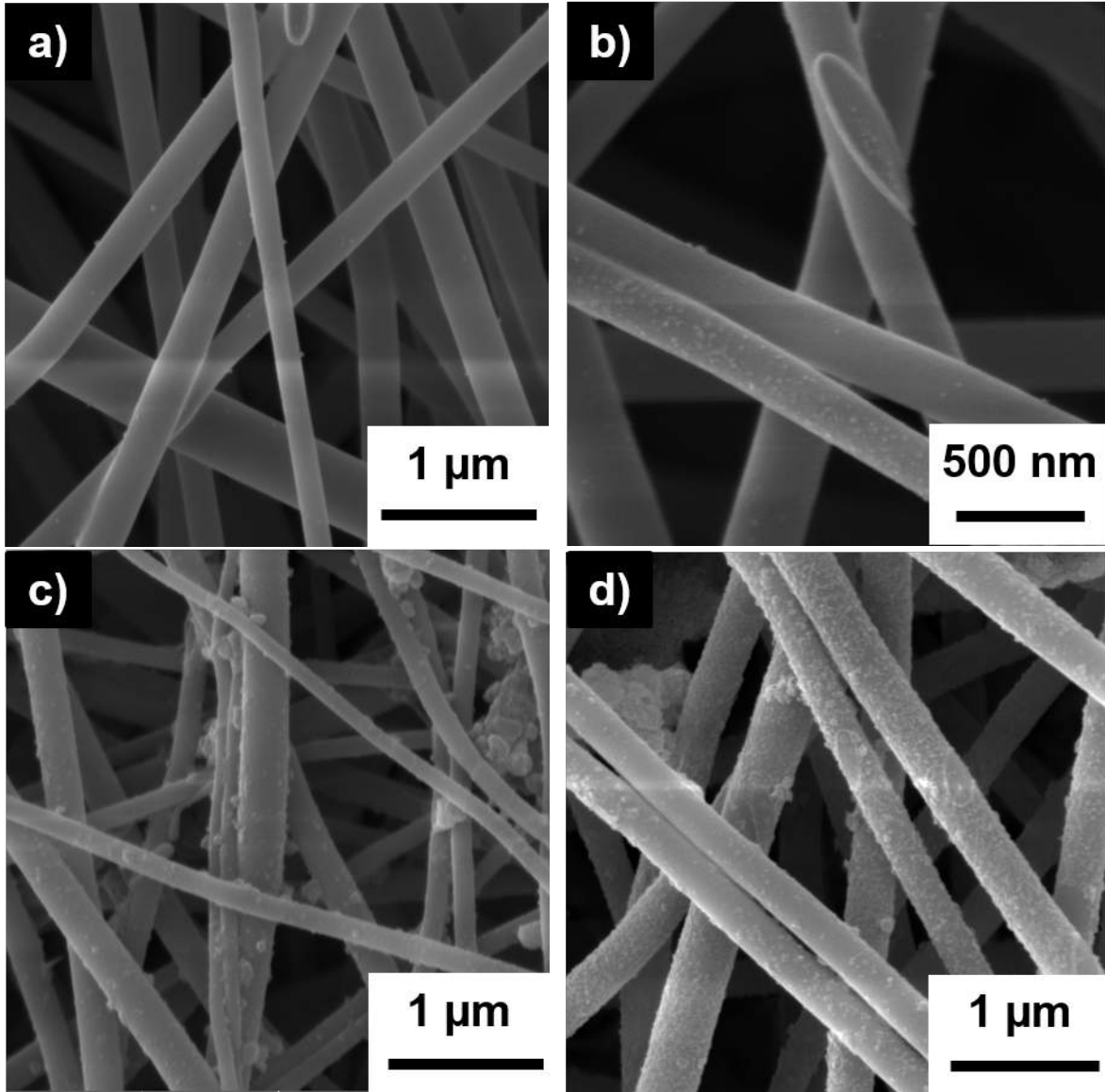
**Figure 6-6** a) Ionic Conductivity of PAN/ceramic based separator membranes a) Nyquist plots for the cells with containing four PAN/ceramic based membranes

Figure 6-7a shows the C/5 cycling performance of various membranes. OPSZ and MSQ have a higher initial capacity of 135 mAh/g compared to 132 mAh/g of the MSX and PSSQ membranes. At the end of 100 cycles, the OPSZ membrane maintains at 92 percent capacity retention, MSQ has 90% retention, and MSX, and PSSQ have an 87% retention each. The improved cycling performance can be attributed to higher conductivity and lower interfacial resistance of the electrolyte-soaked membranes. Increasing the charge rate to C/2 shows all the cells start at a similar capacity, 121 mAh/g (Figure 6-7b). However after 100 cycles, OPSZ separators once again show the best capacity retention, 90 percent similar to retention seen for C/5. MSQ membranes also show excellent capacity retention after 100 cycles maintain 89 percent retention. MSX and PSSQ membranes capacity retention diminishes to 82% and 81% respectively at a C/2. These results show membranes with a sturdy interconnected ceramic sheath layer help to maintain excellent capacity retention at a variety of charge rates. The presence of the Si-O-Si bonds in the sheath layer of the OPSZ and MSQ molecules is able to react with trap water and other impurities in the electrolyte.[27] This leads to thinner and more compact SEI on the cathode which can prevent the intercalation of lithium ions, reducing the capacity retention of the battery cells.

In addition, SEM images taken of membranes after cycling (Figure 6-8) show the membranes without ceramic on the surface show a buildup of fluorine containing particles on the fiber surface. While the OPSZ and MSQ membranes show very little particle buildup on the surface. The buildup of contaminants on the surface drastically reduces the membranes ability to react with the electrolyte salt. This leads to a gradual reduction in salt dissociation, which helps to explain the lower capacity retention observed during the cell cycling.



**Figure 6-7** Cycling performance of LiCoO<sub>2</sub>/graphite full cells at a) 0.2C and b) 0.5C



**Figure 6-8** SEM images of membranes after cycling. a) OPSZ b) MSQ c) MSX d) PSSQ

## 6.4 Conclusion

Various PAN/siloxane hybrid separator membranes were prepared by the electrospinning process. The use of various ceramic precursors resulted in hybrid membranes with different configurations of the ceramic within the polymer. All membranes contain ceramic nanoparticles within the polymer network. However, the OPSZ and MSQ membranes consisted of a sheath

layer of ceramic which resulted in more favorable membrane-electrolyte interactions. This leads to OPSZ and MSQ membranes having the highest electrolyte uptake, ionic conductivity and hence excellent cycling ability. The MSX membrane has a disjointed ceramic sheath and the PSSQ membrane contains no ceramic on the surface of the fiber. The lack of an intact ceramic sheath layer results in a lower ionic conductivity due to the membranes inability to undergo Lewis-base interactions with the electrolyte salt. The lower ionic conductivity resulted in lower cycling performance in comparison with the previously mentioned membranes. Post-cycling SEM images also reveal that the ceramic on the sheath layer can aid in preventing the buildup of fluorine based particles on the surface on the fiber, leading to improved capacity retention.

## References

- [1] P. Arora, Z. (John) Zhang, Battery Separators, *Chem. Rev.* 104 (2004) 4419–4462. doi:10.1021/cr020738u.
- [2] I. Uchida, H. Ishikawa, M. Mohamedi, M. Umeda, AC-impedance measurements during thermal runaway process in several lithium/polymer batteries, *J. Power Sources.* 119–121 (2003) 821–825. doi:10.1016/S0378-7753(03)00248-9.
- [3] G. Venugopal, J. Moore, J. Howard, S. Pandalwar, Characterization of microporous separators for lithium-ion batteries, *J. Power Sources.* 77 (1999) 34–41. doi:10.1016/S0378-7753(98)00168-2.
- [4] K. Gao, X. Hu, C. Dai, T. Yi, Crystal structures of electrospun PVDF membranes and its separator application for rechargeable lithium metal cells, *Mater. Sci. Eng. B.* 131 (2006) 100–105. doi:10.1016/j.mseb.2006.03.035.
- [5] M.-S. Wu, P.-C.J. Chiang, J.-C. Lin, Y.-S. Jan, Correlation between electrochemical characteristics and thermal stability of advanced lithium-ion batteries in abuse tests—short-circuit tests, *Electrochimica Acta.* 49 (2004) 1803–1812. doi:10.1016/j.electacta.2003.12.012.

- [6] K.M. Abraham, M. Alamgir, D.K. Hoffman, Polymer Electrolytes Reinforced by Celgard® Membranes, *J. Electrochem. Soc.* 142 (1995) 683–687. doi:10.1149/1.2048517.
- [7] J. Zhang, Q. Kong, Z. Liu, S. Pang, L. Yue, J. Yao, et al., A highly safe and inflame retarding aramid lithium ion battery separator by a papermaking process, *Solid State Ion.* 245–246 (2013) 49–55. doi:10.1016/j.ssi.2013.05.016.
- [8] W. Yi, Z. Huaiyu, H. Jian, L. Yun, Z. Shushu, Wet-laid non-woven fabric for separator of lithium-ion battery, *J. Power Sources.* 189 (2009) 616–619. doi:10.1016/j.jpowsour.2008.09.078.
- [9] W. Yi, D. Xiaoli, Y. Yunzhen, L. Yun, Study on wet-laid nonwoven separator of lithium-ion battery, *Text. Res. J.* 82 (2012) 1659.
- [10] S.W. Choi, J.R. Kim, S.M. Jo, W.S. Lee, Electrochemical and spectroscopic properties of electrospun PAN-based fibrous polymer electrolytes, *J. Electrochem. Soc.* 152 (2005) A989–A995. doi:10.1149/1.1887166.
- [11] S. w. Choi, S. m. Jo, W. s. Lee, Y.-R. Kim, An Electrospun Poly(vinylidene fluoride) Nanofibrous Membrane and Its Battery Applications, *Adv. Mater.* 15 (2003) 2027–2032. doi:10.1002/adma.200304617.
- [12] D. Wu, C. Shi, S. Huang, X. Qiu, H. Wang, Z. Zhan, et al., Electrospun Nanofibers for Sandwiched Polyimide/Poly (vinylidene fluoride)/Polyimide Separators with the Thermal Shutdown Function, *Electrochimica Acta.* 176 (2015) 727–734. doi:10.1016/j.electacta.2015.07.072.
- [13] Q. Wang, W.-L. Song, L. Wang, Y. Song, Q. Shi, L.-Z. Fan, Electrospun polyimide-based fiber membranes as polymer electrolytes for lithium-ion batteries, *Electrochimica Acta.* 132 (2014) 538–544. doi:10.1016/j.electacta.2014.04.053.
- [14] T.H. Cho, T. Sakai, S. Tanase, K. Kimura, Electrochemical Performances of Polyacrylonitrile Nanofiber-Based Nonwoven Separator for Lithium-Ion Battery, *Electrochem. Solid-State Lett.* 10 (2007) A159. doi:10.1149/1.2730727.
- [15] P. Carol, P. Ramakrishnan, B. John, G. Cheruvally, Preparation and characterization of electrospun poly(acrylonitrile) fibrous membrane based gel polymer electrolytes for lithium-ion batteries, *J. Power Sources.* 196 (2011) 10156–10162. doi:10.1016/j.jpowsour.2011.08.037.

- [16] Y. Liang, S. Cheng, J. Zhao, C. Zhang, S. Sun, N. Zhou, et al., Heat treatment of electrospun Polyvinylidene fluoride fibrous membrane separators for rechargeable lithium-ion batteries, *J. Power Sources*. 240 (2013) 204–211. doi:10.1016/j.jpowsour.2013.04.019.
- [17] J. Hao, G. Lei, Z. Li, L. Wu, Q. Xiao, L. Wang, A novel polyethylene terephthalate nonwoven separator based on electrospinning technique for lithium ion battery, *J. Membr. Sci.* 428 (2013) 11–16. doi:10.1016/j.memsci.2012.09.058.
- [18] H. Dong, D. Wang, G. Sun, J.P. Hinestroza, Assembly of Metal Nanoparticles on Electrospun Nylon 6 Nanofibers by Control of Interfacial Hydrogen-Bonding Interactions, *Chem. Mater.* 20 (2008) 6627–6632. doi:10.1021/cm801077p.
- [19] M. Yanilmaz, M. Dirican, X. Zhang, Evaluation of electrospun SiO<sub>2</sub>/nylon 6,6 nanofiber membranes as a thermally-stable separator for lithium-ion batteries, *Electrochimica Acta*. 133 (2014) 501–508. doi:10.1016/j.electacta.2014.04.109.
- [20] Q. Liu, M. Xia, J. Chen, Y. Tao, Y. Wang, K. Liu, et al., High performance hybrid Al<sub>2</sub>O<sub>3</sub>/poly(vinyl alcohol-co-ethylene) nanofibrous membrane for lithium-ion battery separator, *Electrochimica Acta*. 176 (2015) 949–955. doi:10.1016/j.electacta.2015.07.104.
- [21] W. Chen, Y. Liu, Y. Ma, W. Yang, Improved performance of lithium ion battery separator enabled by co-electrospinning polyimide/poly(vinylidene fluoride-co-hexafluoropropylene) and the incorporation of TiO<sub>2</sub>-(2-hydroxyethyl methacrylate), *J. Power Sources*. 273 (2015) 1127–1135. doi:10.1016/j.jpowsour.2014.10.026.
- [22] F. Bauer, U. Decker, A. Dierdorf, H. Ernst, R. Heller, H. Liebe, et al., Preparation of moisture curable polysilazane coatings: Part I. Elucidation of low temperature curing kinetics by FT-IR spectroscopy, *Prog. Org. Coat.* 53 (2005) 183–190. doi:10.1016/j.porgcoat.2005.02.006.
- [23] H.W. Ro, E.S. Park, C.L. Soles, D.Y. Yoon, Structure–Property Relationships for Methylsilsesquioxanes, *Chem. Mater.* 22 (2010) 1330–1339. doi:10.1021/cm901771y.
- [24] M. Yanilmaz, Y. Lu, M. Dirican, K. Fu, X. Zhang, Nanoparticle-on-nanofiber hybrid membrane separators for lithium-ion batteries via combining electrospraying and electrospinning techniques, *J. Membr. Sci.* 456 (2014) 57–65. doi:10.1016/j.memsci.2014.01.022.

- [25] Z. Wang, F. Guo, C. Chen, L. Shi, S. Yuan, L. Sun, et al., Self-Assembly of PEI/SiO<sub>2</sub> on Polyethylene Separators for Li-Ion Batteries with Enhanced Rate Capability, *ACS Appl. Mater. Interfaces*. 7 (2015) 3314–3322. doi:10.1021/am508149n.
- [26] M. Yanilmaz, C. Chen, X. Zhang, Fabrication and characterization of SiO<sub>2</sub>/PVDF composite nanofiber-coated PP nonwoven separators for lithium-ion batteries, *J. Polym. Sci. Part B Polym. Phys.* 51 (2013) 1719–1726. doi:10.1002/polb.23387.
- [27] K.-H. Lee, Y.-G. Lee, J.-K. Park, D.-Y. Seung, Effect of silica on the electrochemical characteristics of the plasticized polymer electrolytes based on the P(AN-co-MMA) copolymer, *Solid State Ion.* 133 (2000) 257–263. doi:10.1016/S0167-2738(00)00708-6.

## Chapter 7 Conclusion

This work focused on the fabrication and characterization of electrospun polymer/ceramic nanofibers for the use as separators in lithium ion batteries. Separators serve as a physical barrier between the anode and the cathode while still allowing ion transport between the two components. Separators have evolved from microporous polyolefin membranes to electrospun non-woven membranes in an aim to improve membrane porosity and effective diffusivity. To further improve membrane performance, inorganic ceramic nanoparticles have been incorporated into the polymer membranes. To overcome the issues of ceramic delamination and aggregation of the ceramic particles, this research proposed using preceramic liquid precursors that cure using the sol-gel process as an inorganic source instead of the nanosized ceramic particles previously used. To make the membranes, 8 wt% PAN is combined with various siloxane or silazane based liquid precursors to create the membranes using the electrospinning technique.

In chapter 4, organopolysilazane was used in varying amounts from 0 to 30 wt% to demonstrate the effect of ceramic content on cycling performance. The physical and electrochemical properties, such as porosity, mechanical strength, uptake capacity, lithium-ion conductivity, interfacial resistance and cycling performance were investigated. TEM images reveal the resultant ceramic is well distributed within the polymer; with ceramic dispersed in the polymer and also forming a sheath layer around the fibers. Removal of the PAN polymer matrix reveals the ceramic component forms an interconnected network at high loadings. The presence of ceramic on the surface of the fiber along with the increase in amorphous regions of the polymer led to increased higher electrolyte uptake, less interfacial resistance and superior ionic conductivity. Full Cell ( $\text{LiCoO}_2$ /separator/graphite) cells show there is an increase in initial

capacity and capacity retention with increasing ceramic content at both 0.2C and 0.5C charge rates after 100 cycles.

The organopolysilazane used in chapter 4 consist of a polysilazane (Si-N) backbone with a TEOS pendant chain. In Chapter 5, we investigated the effect of the changes to the TEOS:PSZ ratio on the performance of polymer/ceramic hybrid nanofiber membranes. Results show presence of TEOS chains enables the ceramic to form an independently connected ceramic network within the polymer differing it from the discrete ceramic materials that have been used in the past. The interconnected ceramic network also resulted in superior mechanical properties, with tensile strength up to three times greater than of the neat PAN membrane. Ionic conductivity tests reveal the membrane with the greatest TEOS:PSZ membranes has the highest ionic conductivity. Cycling tests show cells containing membranes with an interconnected ceramic networks show the best capacity retention due to the increased amorphous regions and electrolyte uptake. C-rate tests show the 40 wt% TEOS: PSZ is able to maintain up to 55% of its initial capacity at up to 5C.

In Chapter 6, different siloxane based precursors were used to compare to organopolysilazane. In this work, we incorporates four different types of ceramic precursors into PAN polymer to investigate the effect of ceramic morphology on the electrochemical performance on lithium ion batteries. All membranes utilized the electrospinning technique to create bi-component polymer/ceramic nanofibers. Depending on the precursor used there is difference in the morphology of the ceramic component. Two membranes has a continuous ceramic sheath layer on the surface of the fiber (OPSZ and MSQ), one membrane had a disjointed ceramic layer (MSX) , while the final membrane contained ceramic only in polymer matrix (PSSQ). Membranes with a ceramic layer on the surface of the fiber showed a higher electrolyte uptake due to improved electrolyte-membrane interactions. As a result, these membranes also had

superior ionic conductivity which resulted in excellent cycling capacity and retention. Additionally, our post-mortem analysis reveals that the ceramic on the sheath layer can aid in preventing the buildup of fluorine based particles on the surface on the fiber, leading to improved capacity retention.

In summary, various polymer/ceramic blend nanofibers were made using PAN and various ceramic precursors. Using precursors instead of previously used nano-sized particles, enabled high loading of ceramic without particle agglomerates. The use of precursors resulted in unique fiber/ceramic morphology not seen before for polymer/ceramic hybrids used for separators. Ceramic is present in the fiber as well as on the surface of the fiber. The ceramic inside the fiber interrupts the polymers ability to crystallize, leading to increased amorphous regions. In addition, ceramic on the surface improves membrane-electrolyte interaction. Moreover, fibers with ceramic on the surface provide better membrane-electrode affinity, which facilitates the migration of lithium ion at the interface between the electrolyte, and electrode leading to a decrease in cell resistance. Also, Si-O-Si on the surface of the fiber can also enable greater salt disassociation of  $\text{LiPF}_6$ , producing a higher concentration of  $\text{Li}^+$  ions in the cell. All these factors lead to membranes with excellent cycling performance and capacity retention.

## Chapter 8 Recommendation for Future Works

In order to expand upon the research of polymer/ceramic hybrid membranes, the recommendations for future research are include in the following:

- (1) Preparation and characterization of electrospun polymer/OPSZ membranes using various polymers.

For all three projects, PAN was the only polymer used. Changing the polymer used would give some insight into how different polymers interact with the organopolysilazanes and how the use of different polymers changes the electrochemical performance of the separator membranes. In Chapter 3 and 4, PAN/OPSZ 80:20 wt% seemed like the best separator. The PAN/OPSZ 80:20 wt% has the highest thermal stability and the mechanical stability of all the 9 membranes investigated. In terms of electrochemical performance, it has superior cycling retention after 100 cycles and also show impressive cycling during rate capability testing. For a future project, instead of using PAN, another polymer could be used and compared to the performance of PAN/OPSZ 80 wt% to investigate the role of the polymer on membrane properties. Lim et al.<sup>1</sup> suggested polystyrene could be a viable candidate as a secondary battery separator in their study of the ionic conductivity of polystyrene/ $\text{Al}_2\text{O}_3$ . In addition, Koo et al.<sup>2</sup> successfully electrospun polystyrene with a phenylsilsesquiazane (PhSSQZ) to create fibrous membranes showing polystyrene could potentially mix well with polysilazanes. Therefore a future project could involve mixing polystyrene and OPSZ Slow Cure in an 80:20 weight percent ratio and evaluate its thermal, mechanical and electrochemical performance. Polyvinylidene fluoride (PVDF) is also a potentially interesting polymer matrix. Researchers in the Joo group lab have been able to successfully make PVDF/PSZ membranes for coating purposes. Previous works have already

shown that PVDF to be an excellent separator membrane due to its polar regions of the polymer backbone ability to facilitate disassociation of the  $\text{LiPF}_6$  salt. Incorporation of a ceramic component could further add to the performance of PVDF membranes.

(2) Effect of annealing on the electrochemical performance of PAN/OPSZ electrospun membranes as separators in lithium ion batteries

In Chapter 3 and 4, we showed that crystallinity can have a large impact on the electrochemical performance of our separator membranes. XRD results have shown that the as-spun membranes have very similar crystallinity and crystal size regardless of the precursor used. Preliminary ionic conductivity measurements also show that the as-spun separators have a higher ionic conductivity than their annealed counter parts presumably due to the higher amorphous content. However when some of these separators were placed in full cell batteries, their performance was much different than expected. Though as-spun membranes have a similar initial capacity as the annealed membranes, they show very different capacity retentions. In the case of the 90:10 wt% PAN/slow cure membranes, the annealed membranes have a capacity retention of 89 and 88 percent retention after 100 cycles. However, the three as-spun membranes have capacity retention of 74, 80 and 88 percent. This difference in capacity retention shows the as-spun membranes and the annealed membranes are interacting differently with the electrolyte. SEM images done after 100 cycles at  $C/2$  charge rate reveal the cells with the poorest performance have a large amount of material buildup on the surface of the fibers (Figure 8-2). This is further indication that the as-spun fibers are reacting with the electrolyte. As the ceramic loading increases, we see an even larger issue with reproducibility of the battery performance. Work

could be done to investigate how the structure of the inorganic component changes during the annealing process and how this affects the electrochemical performance.

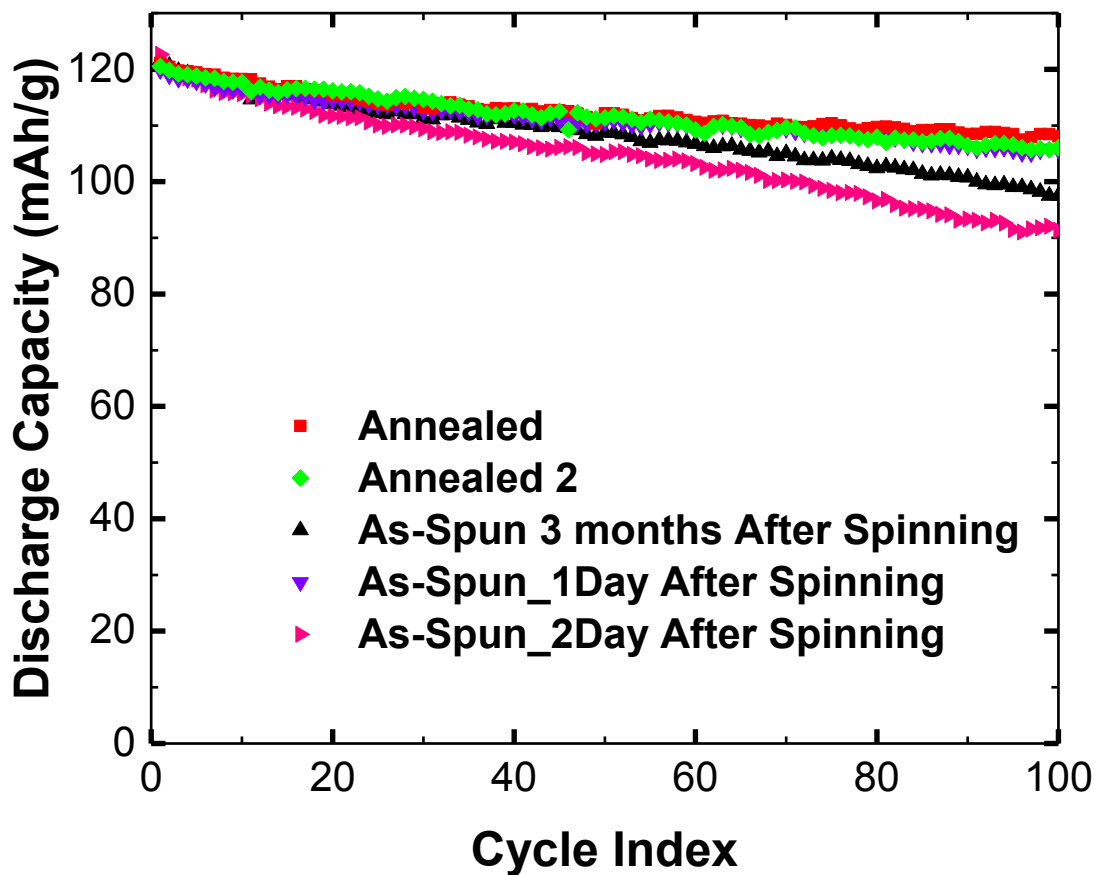


**Figure 8-1** Cycling Performance of various PAN/OPSZ 90:10wt%

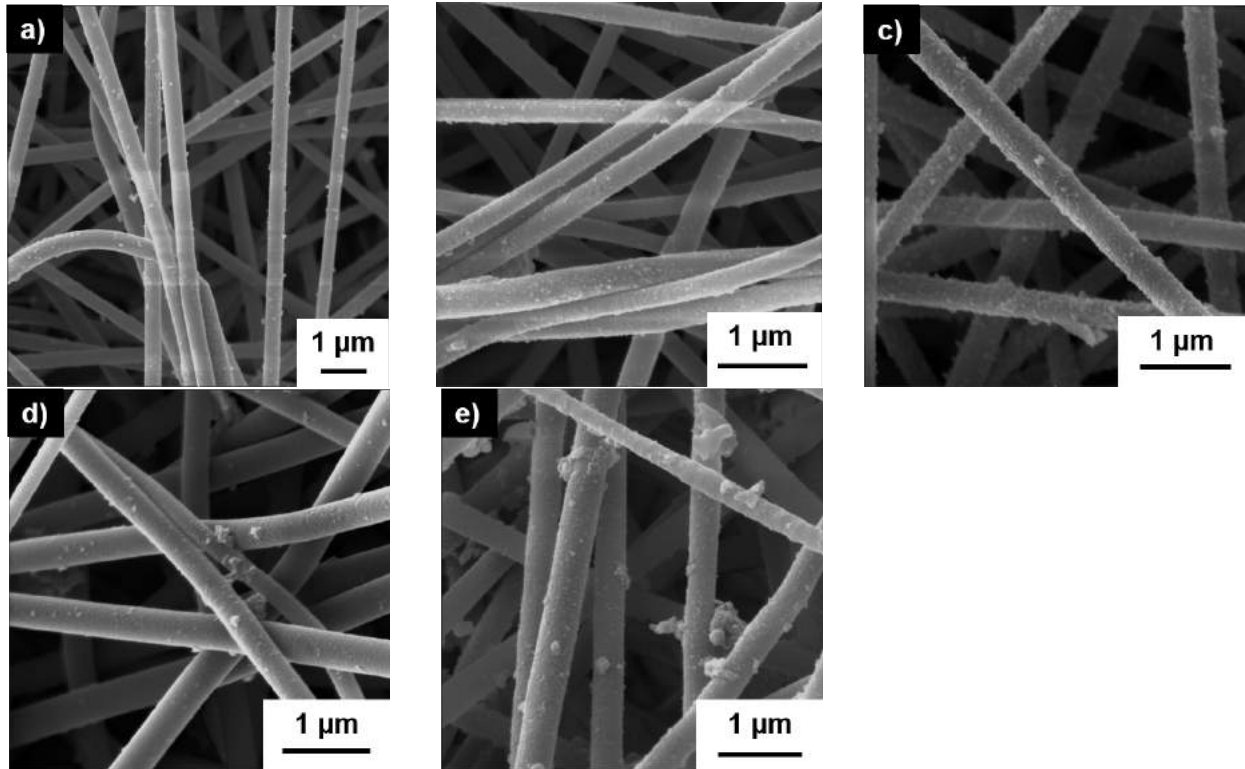


**Figure 8-2** SEM Images of membranes after being cycled at 0.5C for 100 cycles. a) Annealed b) Annealed 2 c) As-Spun 3 months after Spinning d) As-Spun 1 Day after Spinning e) As-Spun 2 days after Spinning

### (3) Comparison of the thermal, mechanical and electrochemical performance of

electrospun PAN nanofibers containing various metal oxide ceramic inclusions

For this work we choose to focus primarily on  $\text{SiO}_2$  based ceramics. However it would be of worth to compare our results to membranes using other ceramic inclusions. Researchers have shown other metal oxides such as  $\text{Al}_2\text{O}_3$ ,  $\text{TiO}_2$ , and  $\text{BaTiO}_3$  make excellent fillers for the use in lithium ion separators. Similar to using  $\text{SiO}_2$ , they can reduce the crystallinity of the fiber, which will leads to an increase in electrolyte uptake and ionic conductivity. In addition, the polar nature of the ceramics can cause disassociation of the  $\text{LiPF}_6$  salt. Therefore, it is recommended to make PAN membranes with various ceramic inclusions to see which ceramic shows the best electrochemical performance. Since nanoparticle fillers have a tendency to aggregate at high

loadings, all ceramic loadings should be kept at 10% in comparison to PAN. Electrospun PAN fibers containing OPSZ, Al<sub>2</sub>O<sub>3</sub>, SiO<sub>2</sub>, and TiO<sub>2</sub> would be made at 10 wt% loading to compare the mechanical, thermal and electrochemical performance of the membranes.

#### (4) Preparation and characterization of centrifugally-spun PAN/OPSZ nanofiber membranes as separator the use in lithium ion batteries

The use of electrospinning to create the PAN/OPSZ membranes resulted in a unique fiber morphology, with ceramic present inside the fiber and also on the surface. Centrifugal spinning has been presented as an alternative to electrospinning due to its high production rate and safety. Centrifugal spinning doesn't require the high-voltage electric field that is required during electrospinning to overcome the polymer surface tension in order to create the fibers. Instead centrifugal spinning involves using centrifugal force to overcome the surface tension of the solution and ejects a liquid solution from the nozzle. There is a possibility that the centrifugal spinning technique could create different fiber/ceramic morphology. PAN/OPSZ solutions would be prepared similar to the preparation steps for electrospinning though the viscosity of solution should be adjusted. TEM images would be taken to investigate the internal morphology of the fiber.

#### References

1. Lim, Y.J., An, Y.H. & Jo, N.J. Polystyrene-Al<sub>2</sub>O<sub>3</sub> composite solid polymer electrolyte for lithium secondary battery. *Nanoscale Res. Lett.* 7, 19 (2012).
2. Koo, S. H. *et al.* Robust multifunctional superhydrophobic organic–inorganic hybrid macroporous coatings and films. *Polymer* 55, 2661–2666 (2014).